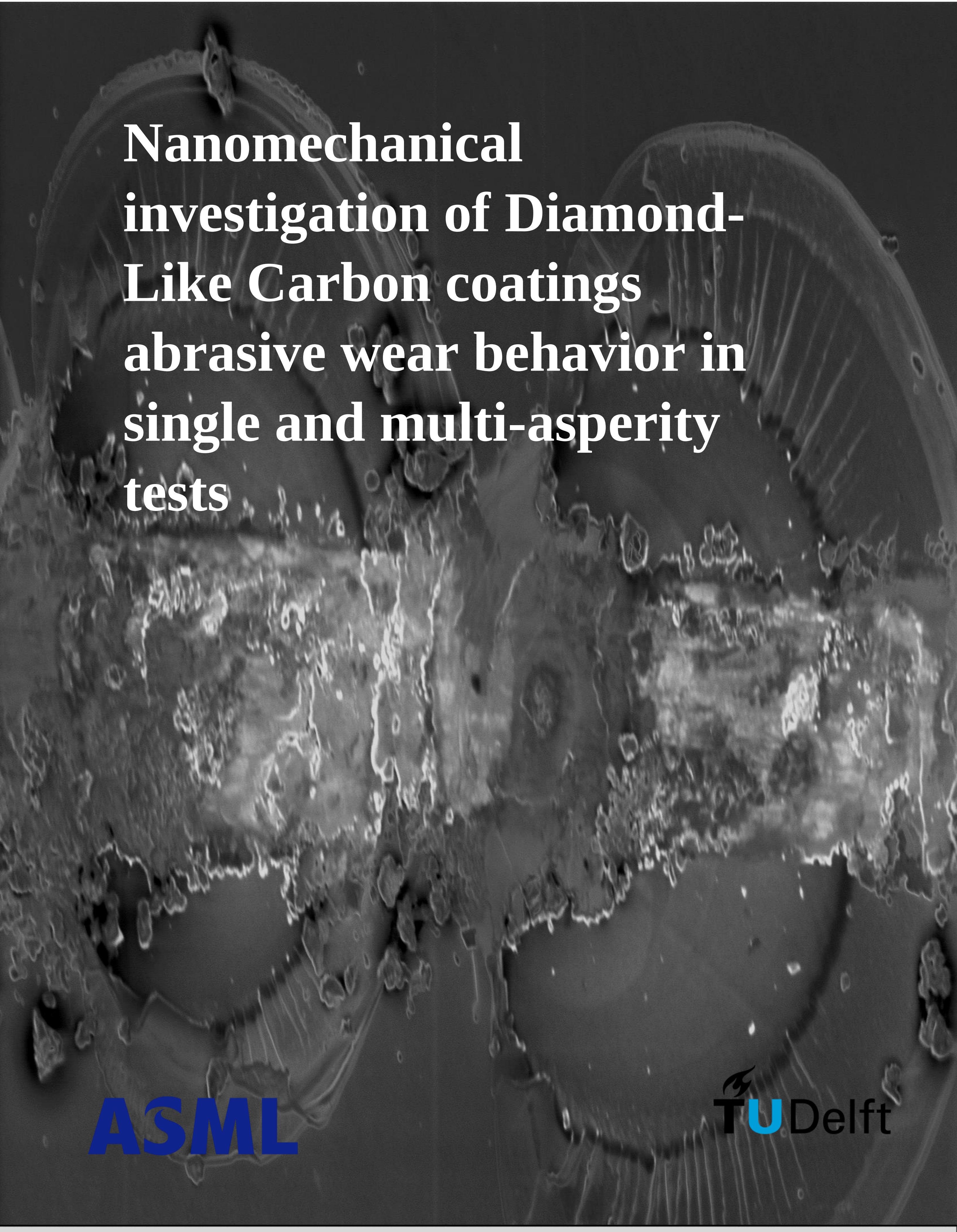

Nanomechanical investigation of Diamond-Like Carbon coatings abrasive wear behavior in single and multi-asperity tests

Nanomechanical investigation of Diamond-Like Carbon (DLC) coatings abrasive wear behavior in single and multi-asperity tests

Student number: 5612322

Thesis duration: May 1, 2023 – February 15, 2024

Thesis committee: dr. Yaiza Gonzalez-Garcia (TU Delft supervisor)

dr. Andres Hunt (TU Delft PME)

Kasper van den Broek (VDL ETG)

dr. ir. Dennis Ernens (ASML supervisor)

The image of the cover is a SEM image showing DLC failure (spallation) under single-asperity scratching test with diamond performed in the current thesis .

Acknowledgement

This thesis was carried out in ASML Research Department in the team of Tribology & Electrostatics. I would like to thank dr. Yaiza Gonzalez Garcia for her instructive and valuable feedback throughout the duration of the Thesis. At ASML I was supervised by dr. ir. Dennis Ernens who truly inspired me to broaden my knowledge on tribology, and with his critical comments helped me to develop as an engineer.

Special thanks to the people from ASML who helped me in the acquisition of AFM and SEM/EDS measurements. More precisely, I would like to thank Leslye Astrid Ugalde Lopez, Annie Bastos Higuera, dr. Cristobal Oliver Vergara, Rens van Houts, and also Martijn Brands for assisting me in the gluing of the samples. Moreover, I would like to thank the project members for their support and critical comments.

Finally, I would like to deeply thank my family and my friends for their continuous moral support.

Summary

Nanomechanical tests to investigate Diamond-Like Carbon (DLC) coating abrasive wear behavior were carried out under different load and strain rate conditions. Nanomechanical tests performed include nanoindentation, single and multi-asperity scratching tests. Nanoindentation tests were performed with a diamond Berkovich tip under 2mN and 50mN maximum normal load and under 4 different strain rates, namely 0.01,0.1,1,10 s^{-1}. Single-asperity scratching tests were performed by sliding a 5μm diamond spherical tip over a DLC coating deposited on SiC under 3 normal loads (10,35,100mN) and 3 different sliding speeds (0.5 μm/s,10 μm/s, 1mm/s) which result in 3 different strain rates.

Multi-asperity scratching tests with a diamond grit paper sliding against DLC/SiC wafers under 50N and 150N normal load at 10 μm/s and 10 mm/s were carried out. Grit paper asperities exhibit various radii, geometry and heights. Furthermore, the wear at the edge of the DLC/SiC wafers was studied by scratching the edge with the diamond grit paper. This was accomplished by placing the grit paper at a certain distance from the wafer's edge, so as its rear part of it was free hanging, while the rest of the grit paper was supported from the wafer. An analytical model was developed to explain the experimental observations. The model derives the equation of motion of a spherical asperity colliding and "climbing" an edge based on classical mechanics and proposes a criterion for minimized edge wear.

Results show that DLC abrasive wear behavior is predominantly plowing. Increasing load results in wear debris at the edge and inside the wear scar. Failure occurs between DLC and substrate (in this case SiC), which is in agreement with the literature. In addition, it is found that strain rate influences DLC wear behavior with increasing normal load. This implies that DLC/SiC interfacial adhesion strength presents strain rate dependency rather than DLC itself. This is supported by nanoindentation measurements, where no strain rate dependency was observed. Therefore, for a DLC coating operating under high loading (≥100mN per asperity) in an engineering application, single-asperity testing is not representative of the engineering application. This is caused by the limitations of single-asperity test setup reaching strain rates close to that of the engineering application.

Finally in the context of this thesis, it is reported that in multi-asperity scratching tests increasing the normal load affected the scratch density rather than scratch depth and width. A mild increase in scratch depth and no difference in scratch width was reported. This implies that there is a range of macroscopic normal loads that corresponds to similar single-asperity wear behavior. Scratching tests performed at the edge of DLC/SiC wafers showed that edge wear depends on the rate of change of asperity interference during collision with the edge. In other words, when the interference of a colliding asperity changes rapidly, the wear at the edge is more severe. More precisely, DLC spallation was observed when the rate of change of interference ($\dot{\omega}$) was maximum, while DLC shallow plowing was reported in the case where $\dot{\omega}$ was minimum. Moreover, an analytical model was developed which predicts that minimization of the impact force (and thus wear) is accomplished when $\dot{\omega}$ takes minimum value. A criterion for minimized edge wear has been established which involves asperity interference at the moment of collision, asperity radius, stiffness, applied normal load, and Coefficient of Friction (CoF). Based on this criterion minimized edge wear takes place when the grit paper asperities are relatively sharp (~1μm) and their initial interference does not exceed 30% of the coating thickness.

Table of Contents

1 Introduction

Friction and wear are phenomena that take place when two surfaces are in relative motion. Relative motion covers displacements from the atomic scale to the macro-scale. Everyday activities in which friction and wear take place include holding, sliding, gripping etc. The first consistent study of friction dates back to the 17th century where Leonardo da Vinci found that the magnitude of the lateral force opposing motion is proportional to the applied normal load during the relative sliding of two bodies. Although many advancements in tribology (the science of friction and wear) have been made, the impact of friction and wear until nowadays is still significant. According to Holmberg and Erdemir [1] 23% of the world's energy consumption is caused by friction and wear. Further, tribological contacts are major contributors to increased CO_2 emissions. Improving tribological behavior in industries like transportation, manufacturing and power generation can lead to cost savings of almost 1 billion euros [1] . Therefore, strategies to improve the tribological behavior of coatings is essential to reduce costs and environmental impact. Diamond-Like Carbon (DLC) coatings are promising, hard coatings which exhibit low friction and high wear resistance, making them suitable for applications in a variety of fields e.g. as coatings on cutting tools.

Further, there is a number of state of the art strategies to combat friction and wear. For example, bio-inspired surfaces have been reported to enhance the tribological behavior of Micro-and Nano electromechanical devices (MEMS/NEMS) [2] [3]. Examples are taken from both the plant and animal kingdom such as the superior hydrophobicity of lotus leaves [4] [5] and reduced friction of teeth-shaped snakeskin design [6] [7]. Although implementing bio-inspired surface textures for enhanced wear resistance seems appealing, difficulties in high load engineering applications still need to be tackled. In many cases (e.g. tool cutting components) work conditions are harsh (e.g. high loads and or corrosive environments), making bio-inspired solutions difficult to be adapted. In other words, the application conditions need to be taken into account as well as the property that the specific design should enhance.

Moreover, novel materials are widely used as solid lubricants. For example, MoS_2 nanoparticles can be used as additives in oil to further reduce wear or they can even be mixed with grease [8]. Molybdenum disulfide (MoS_2) has been extensively studied and it is known for its low friction and wear rate under vacuum and inert gaseous environments [9] However, MoS_2 presents high wear rate in ambient conditions due to the presence of water vapor thus inhibiting its wider applicability. Other materials that do not have this limitation and present ultra-low friction and low wear rate are carbon nanostructures like graphene and fullerene C-60 [10]. Finally, Diamond-Like Carbon (DLC) coatings are widely applicable with exceptional tribological properties, resembling those of diamond [11] [12]. Although they have been studied for more than 50 years, even today active research is carried out to further optimize their tribological behavior.

2 Background

2.1 Friction & Wear

Tribology is the science which investigates the contact between interfaces in relative motion [13]. During such contact a number of physicochemical changes take place which result in friction and wear of one or both materials in contact [14]. Friction is the lateral force opposed to the direction of motion when two surfaces slide relative to each other. Therefore, friction and wear are system properties and not individual material properties. The various mechanical properties and architecture of materials influencing the tribological behavior of a tribo-system are illustrated in Figure 2.1a. Figure 2.1b-c shows the changes that take place during relative sliding and the scales in which these changes occur. Therefore, predicting the complete tribological process is a challenging task because it involves simultaneously friction, wear and deformation in different scales [14].

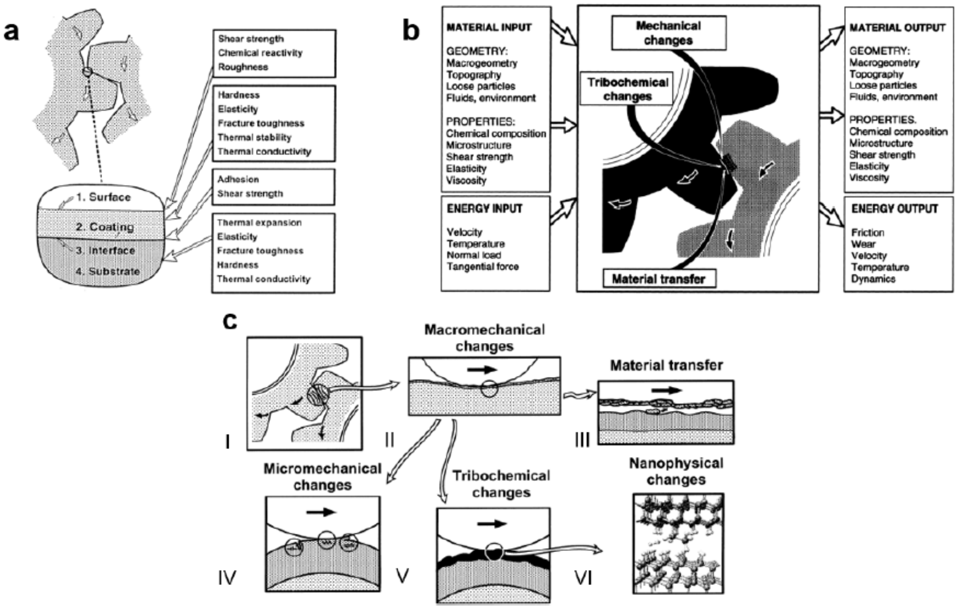

Figure 2.1: (a) Material properties influencing their tribological behavior, (b) Tribological contact between two surfaces includes mechanical and chemical changes as well as material transfer, (c) Tribological phenomena in different scales: I-II: Tribology at the macro-scale, III: Material transfer, IV-V: Microscale, VI: Nanoscale. From [14].

When two bodies are brought into contact, the true (or real) contact area is considerably less than the apparent contact area. This is because the two surfaces are in contact only at localized regions that stick out from the surfaces called asperities. This is illustrated in Figure 2.2. Depending on the normal load per asperity and the materials' yield strength, asperities can deform elastically, fully plastically or elastoplastically. Contact mechanics for different loading regimes are summarized in section 2.2.

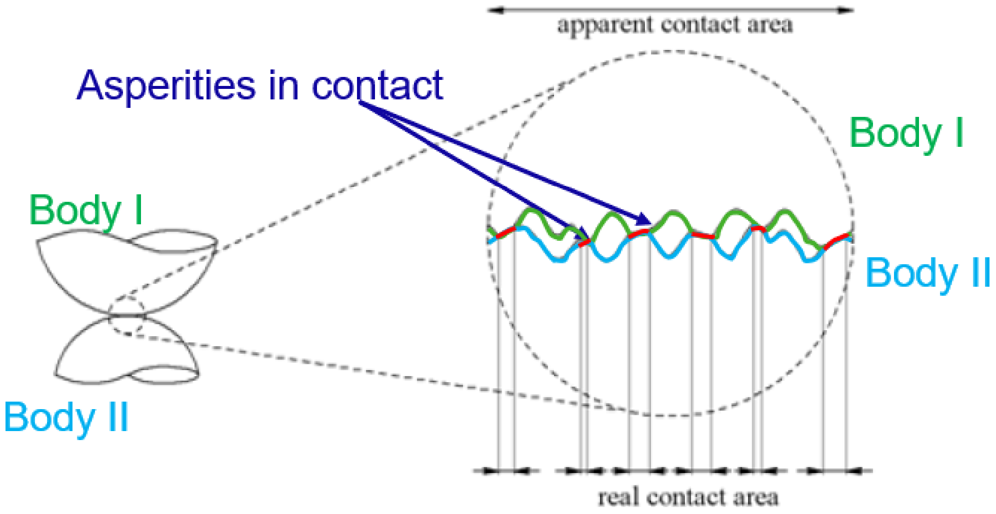

Figure 2.2: Two surfaces are in contact when their asperities touch. Green: Surface profile of Body I, Blue: Surface profile of Body II, Red: Segments from asperities in contact. From [13].

When two surfaces are brought into contact and slide relative to each other, their asperities start to wear. Wear is classified into four different types [15]:

- Abrasive wear.
- Adhesive wear.
- Tribochemical wear.
- Surface fatigue.

In this thesis, DLC abrasive wear is investigated. During abrasive wear, micro-cutting of a surface takes place either by the asperities of the counter surface and/or by particles entrapped in the contact. Severe wear can lead to increased friction, and degradation of coating protective capability.

In tribosystems where the scratched material is a coated system, friction and wear behavior is considerably affected by the coating-substrate adhesion (Figure 2.1a). DLC coatings under high loading suffer from adhesive failure rather than through thickness crack initiation and propagation [16]. Prior to interfacial failure the scratched material is plowed by the counter surface. Figure 2.3a shows a schematic representation of buckling and delamination of a thin coating and Figure 2.3b shows the coating being completely detached from the substrate causing coating spallation. Therefore, the tribological performance of a coating is influenced by the subsurface stresses and strains, which are analyzed in section 2.2.

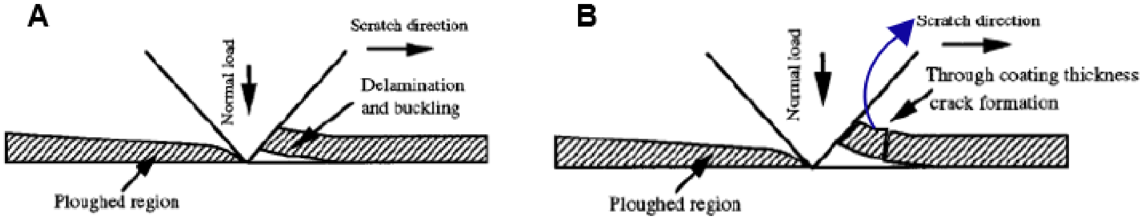

Figure 2.3: Schematic representation of: A: Coating buckling and delamination, B: coating spallation dictated by the curved arrow (complete detachment and removal of whole part of the coating). From [17].

2.2 Contact mechanics

Upon scratching a groove with certain depth, width and pile-ups occurs as shown in Figure 2.6. If scratched material is loaded within its elastic regime the wear track will be relatively shallow since no or limited plasticity takes place. Scratched material is elastically loaded if surface and subsurface stresses do not exceed material's yield stress. Following the Zhao, Maietta, Chang (ZMC) model [18] the contact interference ω is defined as the difference between asperity height (z) and mean separation between the two surfaces (d) and it is given by Equation 2.1 and is illustrated in Figure 2.4.

$$\omega = z - d$$

2.1

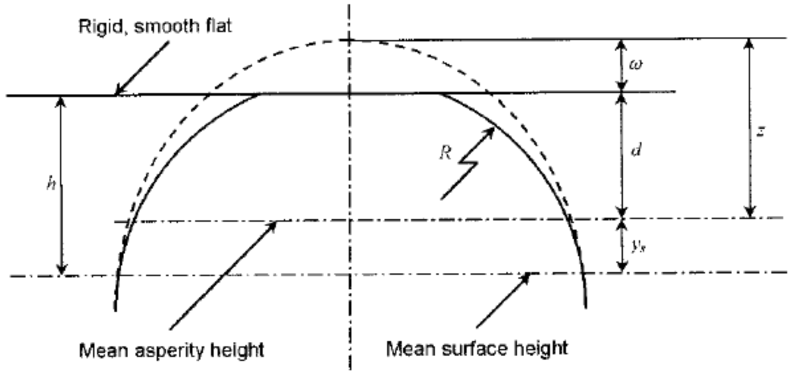

Figure 2.4: Contact between an asperity and a rigid body. From [18] .

Elastic contact

Following the nomenclature used in [18], the equations of the contact area A_e, contact load w_e, maximum contact pressure P_m and mean contact pressure P_a for a fully elastic contact are expressed as a function of interference ω according to equations 2-5 of [18]. In case of single asperity scratching tests, described in section 2.3.1, the normal load w_e is known. Then the contact interference can be obtained by Equation 2.2 and it is a function of the loading condition, asperity radius (R) and reduced modulus $E = \frac{1-v_1}{E_1} + \frac{1-v_2}{E_2}$.

$$w_e = \frac{4}{3}\, E\, R^{\frac{1}{2}}\, \omega^{\frac{3}{2}} \rightarrow \omega = \left(\frac{3}{4}\, \frac{w_e}{E R^{\frac{1}{2}}}\right)^{\frac{2}{3}}$$

2.2

Parameters E_1, E_2, v_1, v_2 are the elastic moduli and Poison ratio of the materials in contact. Subsurface stresses σ_r, σ_θ and σ_z for a pressure profile corresponding to Hertzian theory (elastic loading of a sphere versus a flat [19]) are the following:

$$p = p_0\left(1 - \frac{r^2}{a^2}\right)^n, \qquad n = \frac{1}{2}$$

2.3

$$\frac{\sigma_r}{p_0} = \frac{\sigma_\theta}{p_0} = -(1+v)\{1 - \left(\frac{z}{a}\right)\tan^{-1}(\frac{a}{z})\} + 1/2\, \left(1 + \frac{z^2}{a^2}\right)^{-1}$$

2.4

$$\frac{\sigma_z}{p_0} = -\left(1 + \frac{z^2}{a^2}\right)^{-1}$$

2.5

$$\tau_{rz} = \frac{1}{2}|\sigma_z - \sigma_r|$$

2.6

, where p_0 is the maximum contact pressure, r is the radial distance of a point from the point of contact, a is the contact radius and z is the depth of a point from the surface. The shear stress of Eq. 2.6 is responsible for coating delamination. Contact remains fully elastic until interference exceeds the ω_1 value which is given by Equation 2.7 and is a function of materials' properties (E, H) and asperity geometry (R). The parameter k is taken as 0.4

$$\omega_1 = \left(\frac{3\pi k H}{4E}\right)^2 R$$

2.7

When the interference of rigid tip scratching a flat surface (e.g. in a single-asperity scratching test) is less than ω_1, then the scratched material undergoes elastic deformation. After the tip has passed the surface, elastic recovery takes place, which results in the absence of a wear track.

Fully plastic contact

According to [18] contact is fully plastic if interference exceeds the $\omega_2$value

$$\omega_2 > \frac{4}{k^2}\left(\frac{3\pi k H}{4E}\right)^2 R$$

2.8

Interference ω for a fully plastic contact can be found by taking the difference between the initial and worn profile of the tip following the methodology illustrated in Jamari's work [20].

According to Eq. 2.4-2.6 maximum subsurface stresses take place at a depth of $z = 0.78a$. There, Von Mises or Tresca yield criteria can be applied to calculate the value of maximum contact pressure in which subsurface yield starts. According to [21] choosing different yield criterion does not greatly affect p_0. For an axis-symmetric contact of solids of revolution the load to initiate subsurface stress depends on asperity geometry (R), materials elastic properties (E) and yield stress (Y) as shown in Equation 2.9 .

$$P_Y = \frac{\pi^3 R^2}{6E^2} (p_0)_Y^3 = \frac{\pi^3 R^2}{6E^2} (1.6\, Y)^3$$

2.9

For fully plastic contact, the mean contact area becomes constant and equal to the scratched material hardness. The equations yielding the contact area and contact load are given by Equation 10-11 of [18].

Further, when the interference of rigid tip scratching a flat surface (single-asperity scratching test) is higher than ω_2, then the plastic strains are considerably higher than the elastic strains, and so elastic deformation can be neglected. In other words, the scratched material is plastically deformed. This means that after the passing of the rigid asperity, a groove of certain width, and depth has been formed on the surface of the scratched surface. Also, depending on the hardness of the scratched surface, the material that has been removed from the track will be in the form of debris and/or as pile-ups at the edges of the groove [13]. Important take out is that since the tip is plowing the scratched surface, the load is carried only from the front part of the tip, and therefore the contact area is lower than that at the fully elastic regime.

Elastoplastic loading

For interference values between ω_1 and ω_2 contact is elastoplastic. During scratching of a flat surface with a sharp tip, scratched surface undergoes both elastic and plastic deformation, therefore analytical equations for asperity normal load and contact area become more complex and are illustrated in section 3.3.2 of the work of Masen [13] . Equations hold for conical and spherical asperities.

When the interference of rigid tip scratching a flat surface is between ω_1, and ω_2 then the scratched material undergoes elastoplastic deformation. This means that when the tip plows the surface elastic recovery takes place at its rear end. This results in the change of both the values of the contact area(Figure 3.5 from [13]) and the shape of the contact area (Figure 3.6 from [13]).

Figure 2.5 illustrates the cross section of a groove formed when a tip plows a surface under elastoplastic loading. When the tip passes, the surface is deformed elastically and plastically, while at the rear of the tip elastic recovery takes place, which result in the formation of a *residual* scratch with a residual width (w_{res}) and a residual depth (h_{res}). The groove during scratching, which incorporates elastic and plastic deformation (black line in Figure 2.5), is called *effective* and its width and depth are called effective width(w_{eff}) and depth (h_{eff}). Techniques like Confocal OM and AFM measure the residual depth and width of a scratch. From geometric considerations, the effective width and depth of a scratch are connected with the geometry of tip that caused via Equation 2.10

$$R = \frac{1}{2}\left(h_{eff} + \frac{w_{eff}^2}{4h_{eff}}\right)$$

2.10

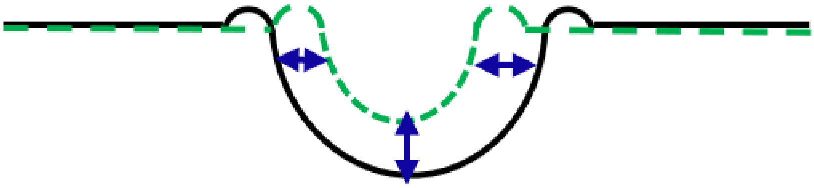

Figure 2.5: Schematic representation of a groove cross section showing the surface when the tip passes (black continuous line) and the elastic recovery taking place at the rear part of the tip (green dashed line). When scratching takes place, elastic and plastic strains are developed while when the tip passes, elastic recovery occurs which result in a narrower and shallower groove (green dashed line).

2.3 Mechanical tests and characterization techniques

2.3.1 Nanomechanical tests

The tribological properties (friction and wear) of DLC coatings can be studied by scratching and nanoindentation tests. Nanoscratch testing was first implied for the investigation of coating adhesion of ceramic coatings [22] [23] [24] [25] [26] [27]. Nowadays, more light has been shed on the use of the nanoscratch technique for single asperity tests in tribological experiments [27]. In single-asperity scratching tests, the three scan progressive method is used in order to acquire quantitative data on the elastic and plastic deformation of the scratched material during scratching.

During the first step of the three scan progressive method, a stylus of known material and geometry approaches the coating surface and scans the surface with the application of a negligible normal load, in order to obtain the surface profile before scratching without wearing the stylus or the coating surface (pre inspection). During the second step, the tip approaches the coating surface, it penetrates it until a certain depth is reached, and subsequently, it moves laterally with either constant or ramped (increasing) load at the desired sliding speed. During this step, a groove of certain width, depth and pile-up will be formed depending on the loading regime of the sliding contact as described in the previous section. Further, the wear track may exhibit one or more of the following characteristics: angular, parallel and transverse cracks, chipping, or spallation [28] [29] [30] [31] [32] [33]. Finally, in the third step, the stylus repeats the operation of first step in order to acquire the surface profile after scratching (prost inspection). A more detailed description of the three-scan progressive method can be found in [34], where an in-depth overview of scratching test is presented.

Taking the difference of z-displacement between the pre-inspection and the one recorded during scratching gives the sum of elastic and plastic deformation of the surface. The difference between the pre and post-scratching z-displacement yields only the plastic deformation, and if it is considerably higher that the beforementioned difference, then elastic strains can be neglected and contact is described as fully plastic.

An important take out is that with single-asperity scratching tests the properties of coating-substrate interface are probed since the subsurface stresses at the coating-substrate interface are comparable to the substrate-coating adhesion strength.

During nanoindentation, an indenter with known geometry (e.g. conical with certain attack angle) and mechanical properties (E,v) is loaded vertically into the material's surface until it reaches a maximum load (P_{max}) and displacement (h_{max}) and subsequently it is withdrawn. With nanoindentation the mechanical properties of the indented material such as elastic modulus (E) and hardness (H) are obtained. A commonly used methodology to extract those properties from nanoindentation is the method introduced by Oliver and Pharr [35]. First results were carried out with indenters having smooth surface [36] and later the theory was expanded for conical indenters [37]. Mathematically, Oliver & Pharr method is based on the use of Sneddon's analysis [38], who solved the Boussinesq problem [38] for simple contact geometries using Hankel transformations. This work is presented thoroughly in the work of Selvaduarai [39].

With nanoindentation, the deformation behavior of the indented material can is investigated. During nanoindentation, settings are adjusted so as the influence of substrate properties do not interfere with the measurement results. The rule of thumb is that penetration depth should not exceed 10% of the coating thickness so as effects caused by the underlying substrate are avoided.

2.3.2 Characterization techniques

After nanoscratch tests both indenter and scratched material in contact exhibit abrasive wear. During single-asperity scratching the stylus removes material in its path, forming a groove with certain width (w) and depth (d). If the scratched material exhibits plasticity, then at the edges of the grooves pile-ups of height h will be formed a shown in Figure 2.6. An indication of material removal is obtained from the wear parameter ξ as stated in Equation 2.11.

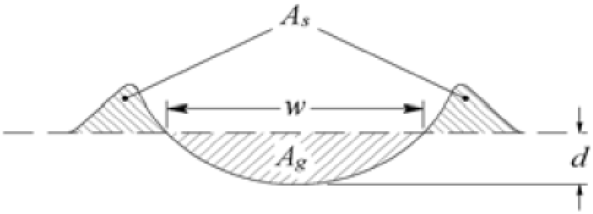

Figure 2.6: Schematic representation of the cross section of a wear scar. Scratching direction is perpendicular to the page. From [13].

$$\xi = \frac{A_g - A_s}{A_g}$$

Equation 2.11

, where A_g and A_s is the cross-sectional area of the groove and pile-ups respectively.

Depending on the tribosystem and loading conditions, scratch dimensions can vary. First, to study the topography of surfaces and scratches White Light Interferometry (WLI) and/or Confocal Optical Microscopy (COM) can be used. Using light-based techniques is beneficial because of their easy use and because they are non-destructive techniques. However, due to diffraction limit of light, features with lateral dimensions close to microscope's wavelength and vertical dimensions of less than approximately 10nm cannot be sufficiently resolved. Under such circumstances, the topography of scratches can be obtained in nanometer accuracy by Atomic Force Microscopy (AFM), where a sharp tip scans the surface under non-contact mode and is deflected by surface features. An overview of the AFM modes is presented in [40] [41], where contact and non-contact modes are briefly explained. The lateral dimension of features analyzed with AFM is influenced by the tip radius. For example, in the AFM measurements of the current thesis 5nm radius SSS NCHR AFM tips where used, which enabled a resolution of 10nm/pixel to be reached. AFM sensitivity at the vertical direction depends on the noise level (at the lower limit) and on the scanning speed and the steepness of the analyzed surface.

Further, Scanning Electron Microscopy (SEM) is suitable to detect cracks at the vicinity of the wear track as well as obtain a more detailed image of the groove. Coupling Confocal OM, AFM and SEM to scratch analysis provides an in depth overview of the wear behavior, topography and processes that took place during sliding (e.g. debris generation). Energy Dispersive Spectroscopy (EDS), can provide quantitative information on material transfer. Also, EDS can confirm adhesive failure in case of spallation by collecting different signals from the substrate and the coating.

Last, coating through thickness cracks and (initial) stages of coating delamination or buckling can be revealed by Focused Ion Beam (FIB) cross sections. If higher resolution is needed (to atomic-subatomic level), implementation of (High Resolution) Transmission Electron Microscopy (HR-TEM) can be used.

2.3.3 Summary

Table 2.1 summarizes the details of the techniques used in the current thesis to investigate the tribological behavior of DLC coatings. Schematic representation of tests, scales that each test is sensitive, the motivation for choosing a particular test and the result of using a particular technique are listed.

Table 2.1: Overview of tests and characterization methods for tribological investigation of coated systems. Table includes the schematic representation or working principle of the techniques, the scale in which techniques are sensitive, the capabilities of a particular test and representative results. Results presented are from single-asperity scratching tests between DLC coating on silicon carbide (SiC) substrate scratched with a conical 5μm radius diamond asperity. The indicated scales represent those used in the experimental setups of the thesis.

Method	Schematic representation	Scale	Capabilities	Result
Scratching	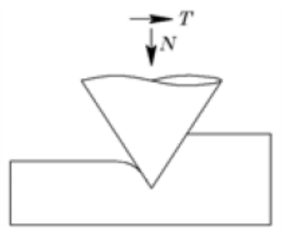 *From* [13].	nm-µm	Study coating-substrate adhesion & coating tribological behavior.	Creation of scratches on the surface of scratched material.
Nanoindentation	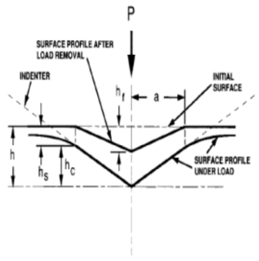 *From* [35].	nm-µm	Extract E and H, and study deformation mechanisms.	Indents on the surface of the indented material.

Confocal Optical Microscopy (COM)	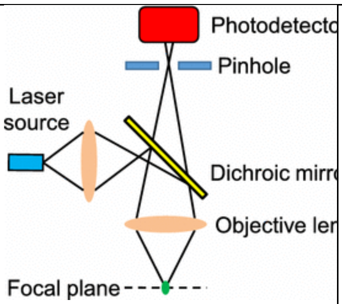 From [42].	Lateral direction: >0.5µm Normal direction >10nm	Obtain the topography of the scratched area.	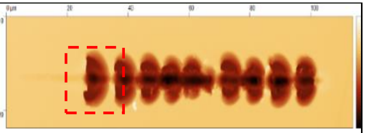
Atomic Force Microscopy (AFM)	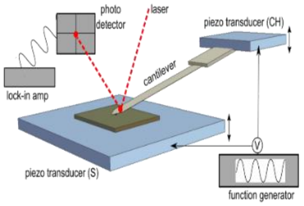 From [43].	Lateral: ~1nm (depending on the sharpness of the tip) Normal direction: 0.1nm< z<2µm (limitation in the ability of the cantilever to follow steep surfaces	Obtain the topography of the scratched area in higher resolution (picture on the right is 20nm/pixel).	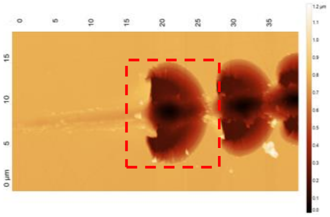
Scanning Electron Microscopy (SEM) Energy Dispersive Spectroscopy (EDS)	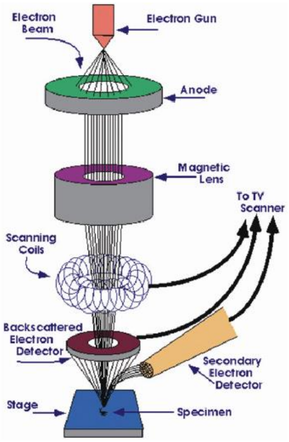 From [44].	>100nm. This limitation is associated with the specific SEM setup that was used for this Thesis.	Detect cracks and gain the morphology of the scratch. Confirm spallations and check for material removal.	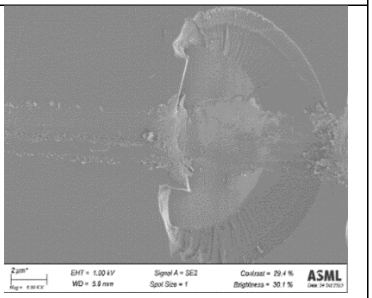 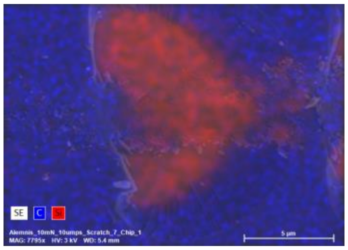 SEM and EDS images are not from the same area

2.4 Diamond-Like Carbon coatings

Diamond-Like Carbon (DLC) coatings are known for their superior mechanical properties resembling the ones of diamond such as low friction, high wear resistance and chemical inertness. DLC coatings are amorphous or hydrogenated amorphous carbon films, with a high fraction of sp3 bonded carbon atoms [16] [45] [46]. In the atomic scale, the structure of DLC films resembles this of a random network [46] [47]. The DLC pseudo phase diagram is illustrated in Figure 2.7, where the three corners of the triangle correspond to sp2,sp3 and H contents. Carbon sp2 and sp3 hybridization results in graphitic and diamond coordination of carbon, respectively. From Figure 2.7 it is seen that along the sp2-sp3 line with increasing C-C sp3 fraction different DLC films exist, starting with amorphous carbon (a-C) films and ending with (hydrogenated or not) tetrahedral amorphous DLC (ta-C:H). DLC coatings exhibiting tetrahedral coordination are denser, and more stressed due to the presence of higher concentration of sp3 clusters.

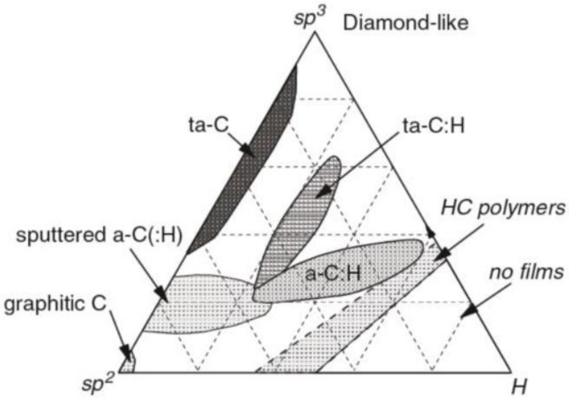

Figure 2.7: DLC pseudo ternary phase diagram. From [45].

The hardness (H) and Young's modulus (E) of DLC films are mainly dependent on the C-C sp3 content [14]. C-C sp2 clusters do not contribute significantly to the mechanical properties of DLC coatings. C-H bonds act, mechanically, as dangling bonds contributing negligibly to Young’s modulus and hardness [48]. Further, in the work of Robertson(1994) [49] it was found that hardness (H) is monotonically dependent on carbon sp3 fraction. Therefore, ta-C:(H) films present the highest E and H values [14]. However, hard DLC coatings show high residual stresses which can cause cracking and/or delamination of the film under the application of high loads [50] [51]. According to the work of Lan and Kato [52] delamination and coating cracking relate to the interfacial delamination causing expansion of already formed cracks. Alloying DLC with metals helps reduce internal stresses (e.g., Cr addition causing sp2 to sp3 transformations) [50]. Silicon addition also has been proven helpful [14].

The mechanical properties (E and H) of DLC coatings as well as their thickness and roughness depend on the deposition technique and the deposition parameters used [14] [46] [22] [53] [54] [55] [56]. For PECVD Young's modulus depends on the energy per incident C ion. Low energies result in lower rates of subplantation. Subplantation is subsurface implantation process where highly energetic carbon atoms penetrate the surface reaching the bulk of the coating, causing local densification and internal stresses due to the formation of sp3 bonds. Therefore, incident C ions having low kinetic energy are deposited as sp2 C-C on the surface. On the other hand, extremely high energy allows the atoms near subplanted atoms to relax promoting sp3 →sp2. The optimum ion energy is proposed to be 100eV [14].

2.5 Thesis Objective

The goal of this thesis is to investigate the abrasive wear behavior of Diamond-Like Carbon (DLC) coatings in single and multi-asperity contacts. For this purpose scratching and nanoindentation measurements were performed in a range of loads to capture the mechanical response of DLC in different loading conditions. In addition, the effect of strain rate on DLC wear was studied. Single asperity tests aim to highlight the interplay between strain rate and normal load to DLC abrasive wear behavior, and multi-asperity tests were taken to link the results of the single-asperity tests with an application. The research questions addressed in the current Thesis are:

1) What is DLC abrasive wear behavior when scratched by diamond particle(s)?
    a. Are DLC coatings wear behavior strain rate dependent?
    b. How does the substrate-DLC interface affects DLC tribological behavior?
    c. What material lift-up features are created during single and multi-asperity scratching?
    d. Does DLC interlayer thickness affect the coating's wear behavior?
2) What is the wear at the edge of a surface when an asperity collides with it at a certain depth?
    a. How does the interference of an asperity colliding with a surface edge change during the impact?
3) What design guidelines should be followed to optimize DLC wear behavior?

3 Materials and Methods

In this chapter the materials and methods used in the current thesis are presented. In addition, the test parameters used are also highlighted. DLC coatings on SiC substrate are studied. Nanomechanical tests performed are single and multi-asperity scratching and nanoindentation tests. The counter-part material in all tests (single and multi-asperity tests as well as nanoindentation) is diamond. An overview of the materials used in each test is provided in Table 3.1. Further, Confocal OM, AFM, and SEM/EDS measurements were performed to analyze scratches. Combining data from nanomechanical and characterization tests will enable a better understanding of DLC abrasive wear behavior.

Table 3.1: Mechanical tests and materials.

Technique	Deformed material	Counter-part material
Single-asperity scratching	DLC coating on SiC substrate	5 µm conical diamond tip
Multi-asperity scratching	x6 DLC deposited on SiC wafers x2 DLC deposited on Si wafers	Diamond asperities with a distribution of height and radius.
Nanoindentation	DLC on SiC	Berkovich diamond tip

3.1 Materials

3.1.1 DLC on SiC

For single-asperity scratching and nanoindentation tests 500 µm thick SiC wafers coated with double layer DLC coating were glued to an aluminum holder. The specimen is illustrated in Figure 3.1a. Interlayer to top layer thickness is 1.0. For multi-asperity scratching tests six 2-inch (50.4mm) SiC wafers coated with DLC were used (Figure 3.1b). The ratio of interlayer (t_i) to top layer thickness (t_t) is between 0.8 and 1.0. Angle-resolved ellipsometry measurements confirmed that the total coating thickness agrees with the manufacturing standard. Schematic representation of DLC/SiC samples is illustrated in Figure 3.2. In addition two wafers with DLC deposited on Si were used to calibrate the multi-asperity scratching test setup.

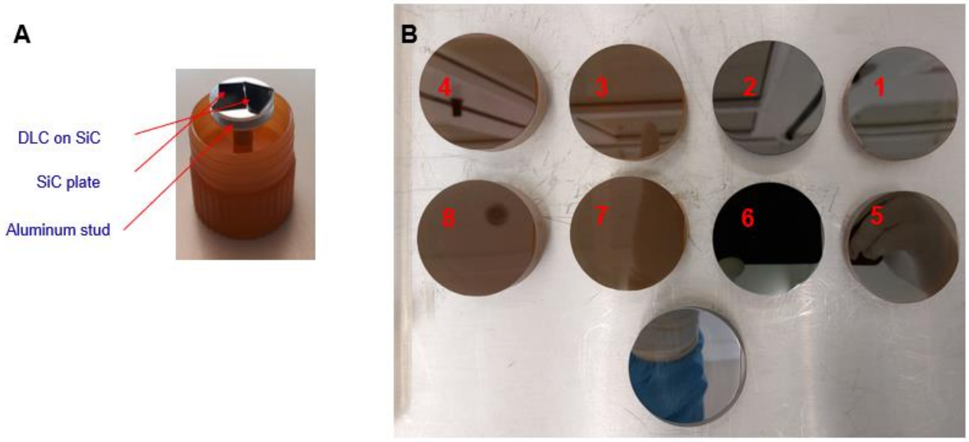

Figure 3.1: A:Specimen used for single-asperity scratching and nanoindentation testing. Right plate is SiC and left is SiC coated with DLC. Tests were performed only in the coated plate. B: DLC/SIC wafers (1-8)used for multi-asperity scratching tests. In the bottom a Si wafer glued on an optical flat is shown which was used to verify the gluing process.

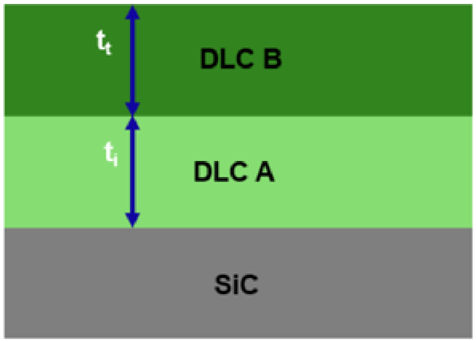

Ratio of DLC interlayer to top layer thickness

Single-asperity & nanoindentation tests	Multi-asperity tests
1.0	0.8-1.0

Figure 3.2: Schematic representation of DLC on SiC coating architecture for single and multi-asperity nanomechanical tests.

Samples used in multi-asperity scratching were glued onto transparent optical flats. Reasons for gluing DLC/SiC wafers onto aluminum stud (single-asperity tests) and optical flats (multi-asperity) is to first, be able to mount them onto the test equipment and second to provide stable backing to clamp them. The DLC coated side was distinguished by the uncoated (SiC) surface of the wafer with Raman spectroscopy. The uncoated side is glued to the optical flat. The steps to successfully glue DLC/SiC wafers (hereafter called wafers) on optical flats are the following:

- Visual inspection of wafers with bright and UV light to detect major spots of contamination and potential damage.
- Clean the surfaces of optical flats and wafers that are going to be glued, with a swab and isopropanol. Optical flats are illustrated in Figure 7a, with their side to be glued facing upwards.

- Put three paper blocks glued with a red tape as shown in Figure 3.3 to sustain wafer in the center of the flat.
- 4gr of Epotek 301-2 bipack glue is baked in a furnace at 200℃ for 1 hour.
- Switch on the EFD dispenser with overpressure of 1 bar over 0.75seconds and underpressure of 5.0kPa.
- A piston, syringe, wipes, EFD needle and the Epotek bipack glue are prepared.
- Glue is mixed for 1 minute over the edge of a table and inserted into the syringe. The syringe is connected to the EFD needle.
- Piston in connected with the EFD dispenser which upon air compression produces 0.1 mm^3 glue droplets. Based on calculations, 70 droplets are needed for taking a safety factor of 10 into account.
- Wafers are gently pushed on flats surface, with the DLC coated side up.
- Place steel weights of 370grams in the middle of the wafers to distribute the glue homogeneously and wait for 3 days (72 hours) for the glue to harden. (Figure 7b)
- Looking the optical flat from the bottom, glue droplets and the glued surface of the wafer are observed. The more homogeneous distribution the better the result. (Figure 7c)

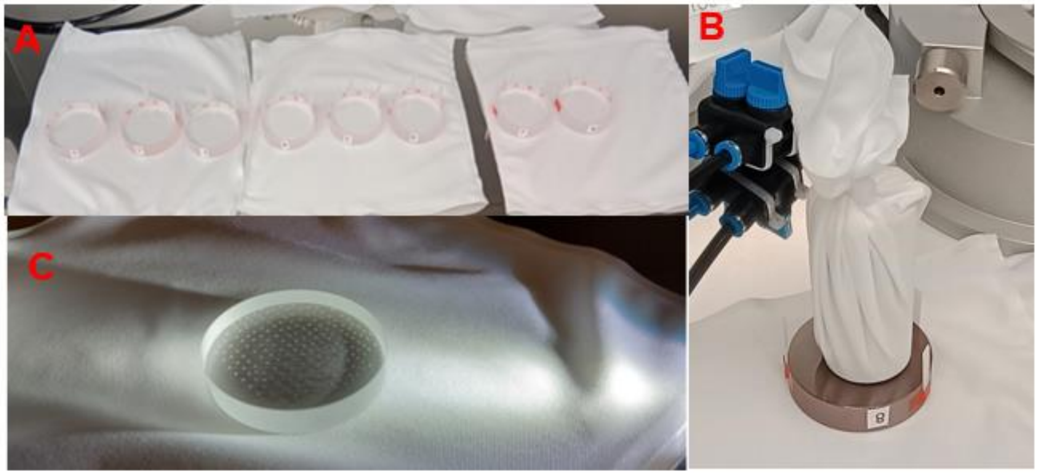

Figure 3.3: (A): Optical flats before gluing, (B): Steel weight pressing upon a DLC/SiC wafer onto an optical flat, (C) Glue droplets as seen from the bottom side of the optical flat.

3.1.2 Counterpart

3.1.2.1 Diamond tip

Single-asperity scratching tests were performed using 3 identical conical diamond tips with radius of 5μm, purchased from Synton-MDP LTD. Nanoindentation tests were performed with a Berkovich tip with angles $\alpha_1 = 120°$, $\beta_1 = 65.26°$, $\beta_2 = 65.38°$ and $\beta_3 = 65.36°$ against Si to calibrate the tip. In situ SEM micrographs of the conical and Berkovich tips are illustrated in Figure 3.4. SEM/EDS images of the worn tips used in scratching tests are shown in section A.1.3 of Appendix. Also, the order in which the tips were replaced can be found in section A.1.1 of the Appendix.

3.1.2.2 Diamond grit paper

During multi-asperity scratching tests, a diamond grit paper was used to scratch the DLC wafers. The diamond grit paper is adhered onto a steel holder in order to be mounted for scratching tests. Due to the particular adhesion method used, the grit-paper-steel holder systems shows considerable compliance. This compliance results in a decrease of the diamond asperities rigidity.

The overview of the grit paper (hereafter called diamond grit paper) and its schematic representation is illustrated in Figure 3.5. The steel holder of radius R has a hole in the middle of radius r. The contact between the grit paper and the wafer occurs inside the area enclosed by the two circles of Figure 3.5a. The grit paper consists of diamond asperities of various height and radius embedded in epoxy resin. Asperity radius is discussed in section 3.2.3.

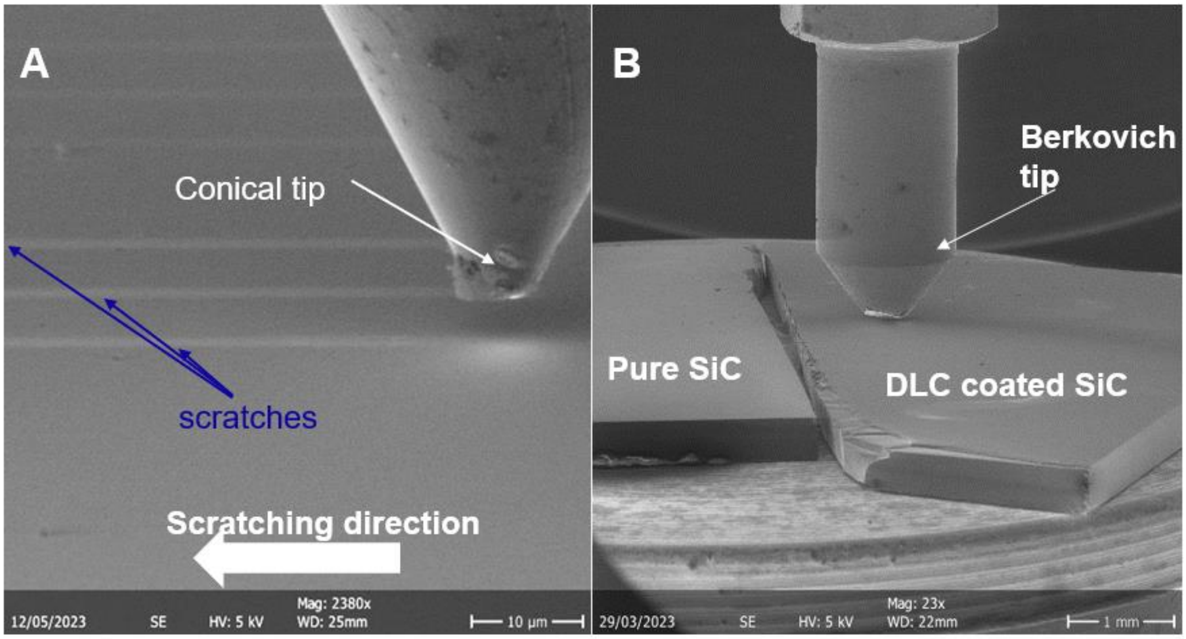

Figure 3.4: In situ SEM images showing the conical tip used in scratching tests (A) and Berkovich tip used in nanoindentation test.

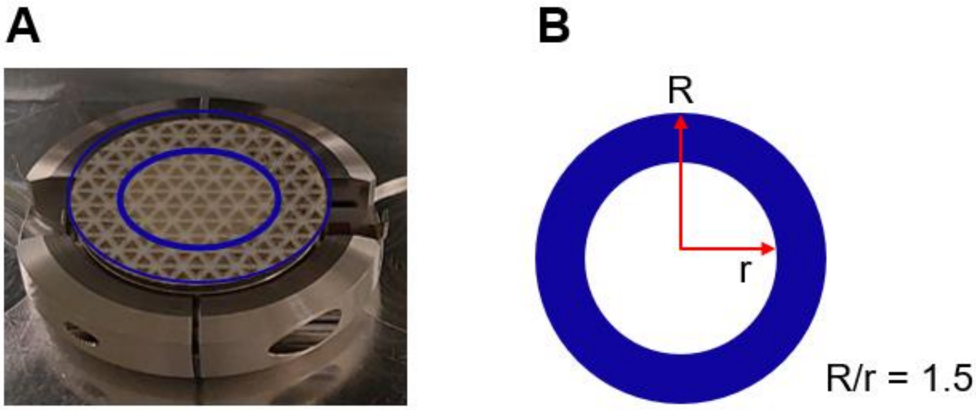

Figure 3.5: (A) Diamond grit paper used in multi-asperity scratching tests. The darkened area within the two blue cycles is the apparent contact area with the wafers, (B) 2D-Schematic representation of the ring-shaped apparent contact area.

3.2 Methods

An overview of the methods used in the current thesis is provided in Table 3.2.

Test	Equipment	Parameters	Environment	Motivation
Single-asperity scratching performed in Alemnis AG facilities	Alemnis Standard Assembly (ASA)-Standard Load Cell 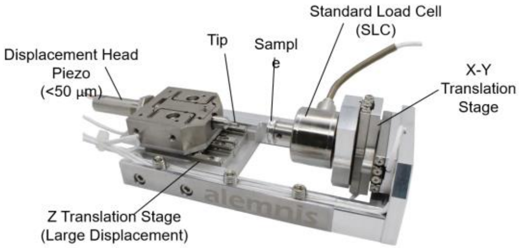 	Normal load: 10, 35, 100 mN . In each scratches with 3 different strain rates : 0.5,10,1000 µm/s	Outside of cleanroom. Ambient conditions.	Study strain rate influence on DLC abrasive wear behavior., observe lift-up features, study DLC failure, study DLC/SiC interface
Nanoindentation performed in Alemnis AG facilities	Alemnis Standard Assembly (ASA) – Mini Load Cell (MLC) 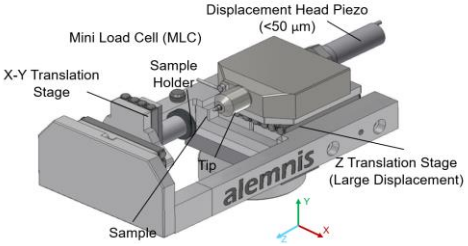 	Normal load: 2mN & 50mN , under 4 different Strain rates: 0.01, 0.1,1,10 µm/s	Outside of cleanroom. Ambient conditions.	Study strain rate dependent DLC deformation by evaluating E and H
Multi-asperity scratching	Bruker UMT equipped with 200N load cell and a vacuum clamping chuck 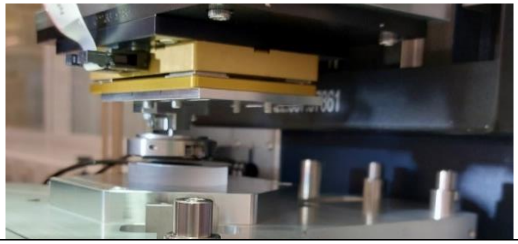	Normal loads: 50N, 150N Strain rates: 0.01, 10 mm/s	Inside grade 4 cleanroom. Ambient conditions.	Compare with single-asperity findings, correlate scratch-asperity,

Test	Equipment	Parameters	Environment	Motivation
Confocal OM	Sensofar SensoSCAN 6.6 	x5 lens for first inspection, x150 to analyze topography	Inside grade 4 cleanroom. Ambient conditions.	Obtain quantitative results on scratch width, depth and pile-up height, and observe DLC wear behavior
AFM	Parker NX20 	10nm/pixel , Non-contact mode,	Inside grade 4 cleanroom. Ambient conditions.	Obtain topography in high resolution
SEM/EDS	ZEISS Sigma 300 SEM & ZEISS QUANTAX EDS set-up 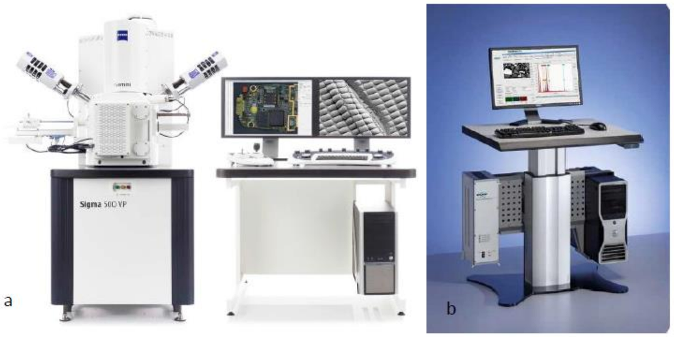	SEM: x7795 magn, EHT= 1kV, 3kV WD: 5.9mm, secondary electron sensor, EDS: EHT: 3 kV, WD: 5.5mm,	Outside of cleanroom. Ambient conditions.	Obtain topography at and near scratches, observe cracks, confirm interfacial failure

Table 3.2:Experimental methods used in the thesis, parameters used and motivation of each technique.

3.2.1 Nanoindentation

Nanoindentation measurements were performed at Alemnis AG facilities using the Alemnis Standard Assembly equipped with the Mini Load Cell (Table 2.1). System compliance was estimated by nanoindentations from a Berkovich tip on fused silica. Six indentations were performed with maximum load of 500mN.. Tip area calibration was done by nanoindentations of a Berkovich tip onto a SiC wafer under 20mN. Assumed elastic modulus and Poisson ratio is 410 GPa and 0.2, respectively. Distinction between DLC coated SiC and SiC plate of the specimen illustrated in Figure 3.1a was made by inspecting the load-displacement curves of nanoindentations under 2mN and 150mN. Measurements were carried out under true displacement control for two different maximum loads namely 2mN and 150mN. In each load four different strain rates were used (0.01, 0.1,1, 10 s^{-1}). For each conditions 9 indentations were carried out for repeatability. A total of 72 indentations were performed.

3.2.2 Scratching tests

3.2.2.1 *Single-asperity*

Single-asperity scratching tests were carried out by Alemnis AG in their facilities in Switzerland using an Alemnis Standard Assembly equipped with the Standard Load Cell [57]. A sensor measuring lateral force is mounted as shown in Figure 3.6 (noted as (LFS)). The experimental setup is illustrated in Figure 3.6. Scratching tests were performed under load control mode. Test series along with their parameters used are summarized in Table 3.3. Scratches at three normal loads and three different strain rates were used. For each condition 9 scratches were performed for consistency and repeatability. In total 81 scratches were performed. Test methodology is illustrated in Figure 3.7, which is the three-scan method. First, the stylus scans the surface before scratching (first block of Figure 3.7), second it scratches the surface with the desired parameters (second block), and finally the stylus scans the surface to obtain the profile after scratching (third block). Further, tilt correction was performed by subtracting the pre-scratching z-displacement data from post scratching data.

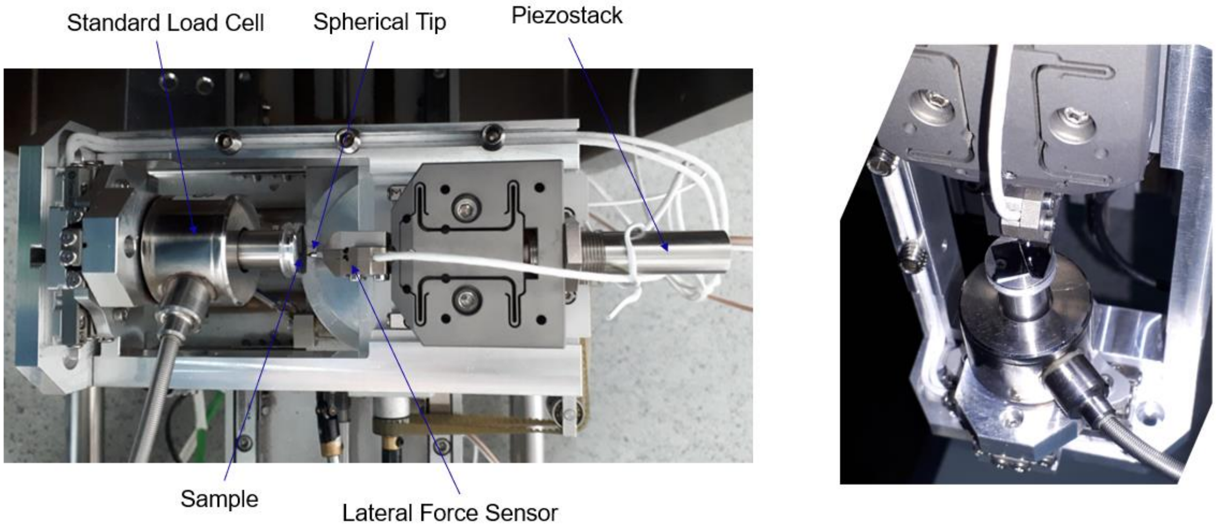

Figure 3.6: Left: Alemnis Scratching test setup, Right: DLC/SiC sample mounted onto sample holder.

Table 3.3: Single-asperity test parameters. Scratches in 3 different loads were performed. In each load 3 different sliding speeds which result in different strain rates were used. For each condition (load and strain rate) nine scratches were performed in order to check the repeatability of the results.

Test series	Normal load (mN)	Asperity radius (μm)	Sliding speed (μm/s)	Sliding distance (μm)	Number of scratches per parameter change
1	10	5	0.5, 10, 1000	50, 100, 2000	9,9,9
2	35		0.5, 10, 1000	50, 100, 2000	9,9,9
3	100		0.5, 10, 1000	50, 100, 2000	9,9,9

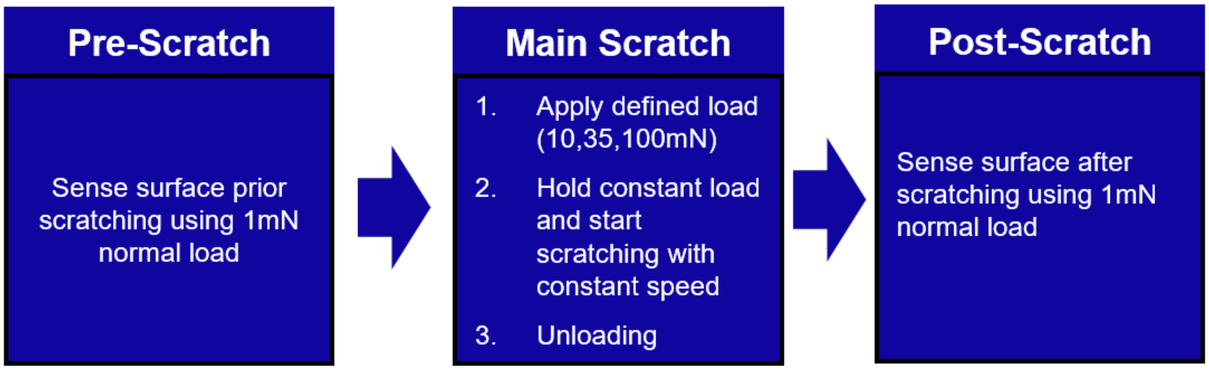

Figure 3.7: Schematic representation of single-asperity scratching test procedure.

Finally, the success criteria for a measurement to be regarded as trustworthy are the following:

1. Sliding speed should be constant and equal to the requested value.
2. Normal load during scratching should be constant and equal to the requested value.

3.2.2.2 Multi-asperity

Multi-asperity scratching tests were performed using the Bruker Universal Mechanical Tester (UMT) equipped with a 200N load cell and a vacuum chuck. Diamond grit paper adhered to a steel holder was mounted into a metal rod which is connected to the carrier which is connected to the load cell. Sensors that measure the normal and lateral force transmit the signals to a software whose interface is presented and controlled in a PC monitor. The 2-inch wafers are clamped into the wafer chuck using vacuum, in order for the wafers to remain stable during high load scratching. Wafer chuck is made of steel with a 2-inch circle in the middle to enable the positioning of the wafers. In the left upper corner the vacuum hose is connected with the wafer chuck. Schematic representation of the vacuum chuck can be found in A.3. The test set-up is illustrated in Figure 3.8.

In order to calibrate the setup two DLC on Si wafers (wafer number 3 and 4) and a spare diamond grit paper were used. The success criteria for a measurement to be regarded as trustworthy are the following:

1. From start to finish, the normal load needs to remain approximately constant (±3N) at the desired load. Fluctuations caused by system's compliance are expected. Factors adding to the compliance of the system include:
    a. Diamond grit paper design,
    b. Mounting way

    c. Bruker UMT components compliance.
2. Sliding speed needs to remain constant throughout scratching.

Different calibration settings were required for different loads, sliding speeds and grit paper's initial position as shown in Table 3.4.

Test parameters used in multi-asperity scratching tests are summarized in Table 3.5. Measurements were performed with 50N in order for scratch density to be relatively low. This enables scratches to be analyzed with Confocal OM. Also, when applying 50N taller asperities cause the most severe wear, causing deeper scratches compared to the shorter ones. When applying a normal load of 180N to the wafer versus a flat wafer, then the mean load per asperity is found to be approximately 10mN according to the following scaling calculation:

$$f = \frac{A}{A_{grit\ paper}} F$$

, where $A_{grit\ paper}$ is the area of the blue ring of Figure 3.5, f is the mean normal load per asperity, F is the normal load applied to the diamond grit paper and A the contact area of the application. Due to a persistent error, the maximum reachable normal load was 150N.

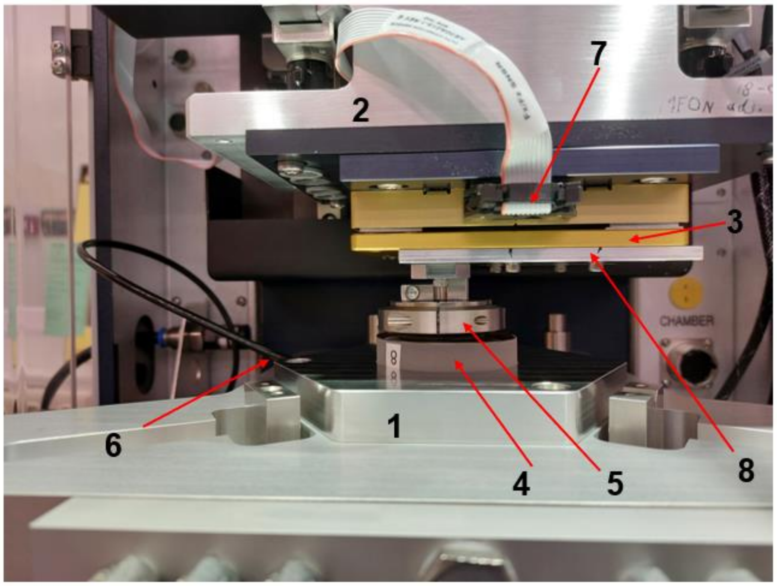

Figure 3.8: Bruker UMT custom setup for multi-asperity scratching between diamond grit paper and DLC/SiC wafer. 1: Wafer clamping chuck, 2: Moving carrier, 3: 200N load cell, 4:Optical flat with DLC/SiC wafer glued on top, 5: Diamond grit paper/steel holder, 6: Vacuum hose, 7: Connection cables, transmitting 8: Normal force (F_n) and lateral force (F_t) sensors.

The testing procedure followed is as follows:

- First, the testing procedure is written in a script in the Bruker UMT software.
- The diamond grit paper approaches the wafer with 2mm/s speed until a certain distance is reached. Then the diamond grit paper approaches the wafer with 0.25mm/s until is in contact.
- Contact is made when the normal sensor senses a force equal in magnitude with the weight of the grit paper and the steel holder.

- Then, the grit paper is pushed downwards with 0.025 mm/s or 0.005 mm/s until the desired scratching normal load is built-up. The tracking speed is 0.005 mm/s for F_n=150N tests and 0.025 mm/s for F_n=50N tests.
- Subsequently the carrier moves laterally under load control mode (constant normal load) for certain distance where the diamond grit paper scratches the DLC surface.
- Finally, when scratching is finished grit paper is retracted and moved to its initial position with a speed of 1mm/s.

Multi-asperity scratching tests were acquired with the grit paper starting at two different positions as shown in Figure 3.9. In case shown in Figure 3.9a-b, the diamond grit paper is positioned on top of the wafer and is fully supported. Then the grit paper starts scratching the DLC surface. In case illustrated in Figure 3.9c-d the diamond grit paper starts scratching with its rear part being free-hanging.

Because of mounting the grit paper to the metallic rod, when the grit paper was unloaded it had two degrees of freedom: one was in-plane rotation and second was out of plane rotation. Upon loading, these motions are expected to be partially suppressed.

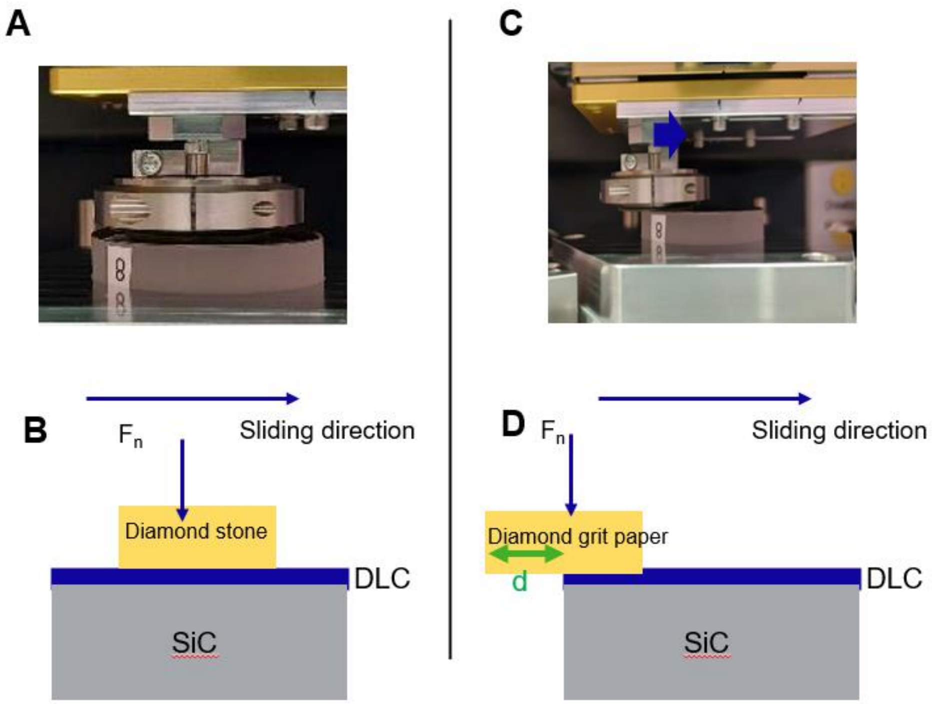

Figure 3.9: Multi-asperity scratching tests with diamond grit paper starting at two different positions. A: Grit paper start scratching while being fully in contact with the wafer, B: Schematic representation of case A, C: Grit paper start scratching having its rear edge in a distance d from wafer edge, D: Schematic representation of C.

In Table 3.5 measurements with the note "edge" were taken with the grit paper starting at the edge of the DLC wafer as shown in Figure 3.9c-d. Three different conditions of normal load and initial distance from DLC/SiC wafer edge were studied as described in Table 3.6. In case I, grit paper was loaded with 50N and started at an initial distance d equal to half of grit paper's diameter. In case II, and case III the grit paper was loaded under 150N.

Wafers that have been used more than once were rotated 90 degrees after each use in order for old and fresh scratches not to interact with each other in the beginning of the scratches.

Table 3.4: Calibration settings for the different multi-asperity scratching tests.

Diamond grit paper initial position	Normal load (N)	Strain rate (mm/s)	Tracking speed (mm/s)	Data acquisition frequency (s^{-1})
On top of DLC wafer	150	10	0.015	100
	50	0.01	0.035	100
On the side of DLC wafer	150	10	0.045	1000
	50	10	0.015	100

Table 3.5: Multi-asperity test parameters.

Wafer number	Normal load (N)	Interlayer to top layer thickness	Sliding speed (mm/s)	Sliding distance (mm)
1	50	0.8	10	15
2	50 50 (edge)	0.8	0.01 10	0.2 50
5	50 150 (edge)	0.8	0.01 10	0.2 55
6	50	0.8	10	15
7	150N	1.0	10	15
8	50 150 (edge)	1.0	10 10	15 55

Table 3.6: Normal load and distance from wafer edge in multi-asperity scratching tests.

Case number	Wafer number	Normal load (N)	Distance from the edge/ grit paper diameter
I	2	50	0.5
II	8	150	0.5
III	5	150	0.1

3.2.3 Confocal Optical Microscopy (COM) and Atomic force Microscopy (AFM)

First, scratches are analyzed by Sensofar NEOX Sensoscan6.6 microscope equipped with x5,x25,x50, and x150 magnification lenses. Confocal Optical Microscopy mode was used for measuring scratches on DLC/SiC wafers and Focus Variation method was used to analyze the pre-post state of the diamond grit paper asperities. Focus Variation is suitable for measuring highly rough surfaces. In order to obtain the scratch topography magnification was gradually increased from the lowest (x5) to the highest (x150).

Analysis was performed with Gwyddion and SensoView software. In order to obtain scratch width, depth and pile-up height images need to be flattened. Equivalently, any background should be removed. A representative example is illustrated in Figure 3.10 . This can be accomplished in a number of ways. Here the steps followed to remove background are illustrated. If the first step does not remove the background, the following step is tried. Assessment of the resultant image was performed by eye inspection.

- Images were flatten by plane subtraction. In most of the times this suffice.
- If plane subtraction does not work, background was removed by a plane through three points. Typically this step produced similar results with step 1, but sometimes depending on the location of the points chosen this method yielded better results.
- If this doesn't result in flattening the image, the Flatten Base function of Gwyddion was used only in the scratches where spallations were measured. In order for the process to be successful spallated volumes were masked, and then the Flat Base function was applied.
- Finally image was flattened by removing polynomial background. This step was helpful when taking images at wafer edges.

In order to extract the scratch width (w), scratch depth (d) and pile-up height (h) the following methodology was used:

- For each scratch, cross sections were taken by averaging profile properties over a certain length. In Figure 3.11 averages were taken over 5μm.
- The average width, depth and pile up height of these cross sections were taken.
- These averages were scratches' groove depth, width and pile-up height.

The radius of asperities of the diamond grit paper were investigated by Confocal OM. The part of grit paper that was studied is from 6 to 9 o' clock position. The followed methodology to extract diamond asperity radius using Gwyddion software is the following:

- Remove background as described earlier in this section.
- Isolate parts of the image with height above 99%. With this way, the taller asperities are isolated from shorter ones. Taller asperities would be the first to carry the applied normal load and plow the DLC surface.
- Make cross sections of the tip of diamond asperities.
- Fit the shape of the tip with best fitted circle using Gwyddion's Critical Dimension function. The radius of the best fitted circle is asperity's radius of curvature (RoC).

Atomic Force Microscopy was used to acquire the topography of scratches in higher resolution (HR). Measurements were acquired by Park NX20 instrument. High resolution images were taken under non-contact mode and with 10nm/pixel resolution. Tip movement when scanning was perpendicular to scratch direction. AFM images were analyzed by Gwyddion 2.61 software as follows (see also Figure 3.12):

- Plane removal. If this procedure worsens the image (assessed with eye-inspection) then is skipped.
- Aligning rows using " Matching" method perpendicular to scratch orientation. If the scratch is visible, no further steps are needed. With this way if the AFM image presents a step height, all areas will be brought in the same plane.
- Aling rows using "Matching" method parallel to scratch orientation.

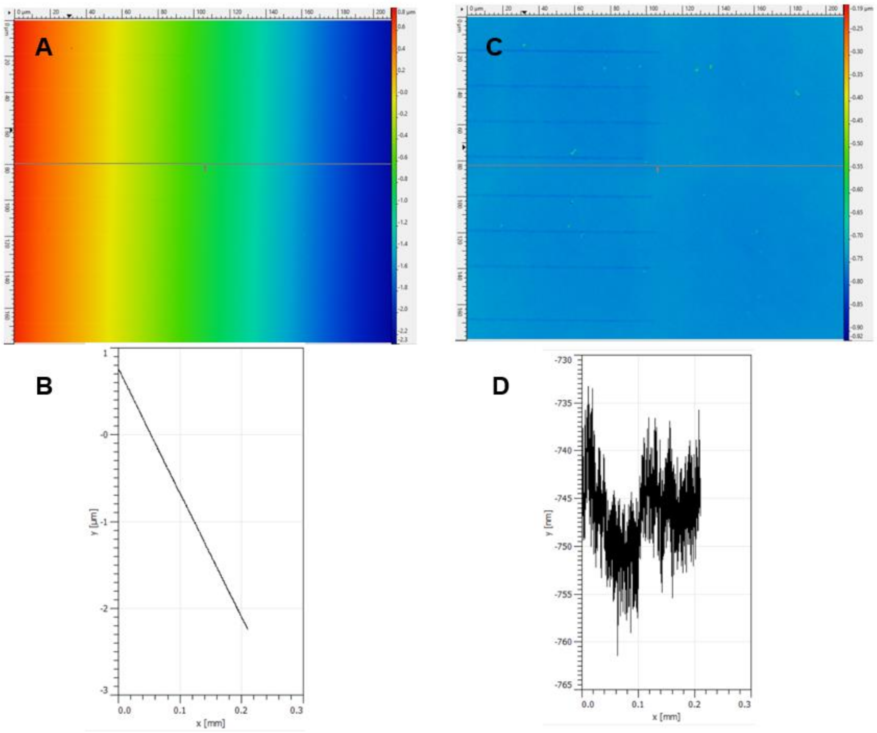

Figure 3.10: Background removal in COM image. (A) Raw image as measured by Sensofar NEOX,(B) Profile, (C) Image after background removal, where scratches are revealed, (D) Surface profile after background subtraction.

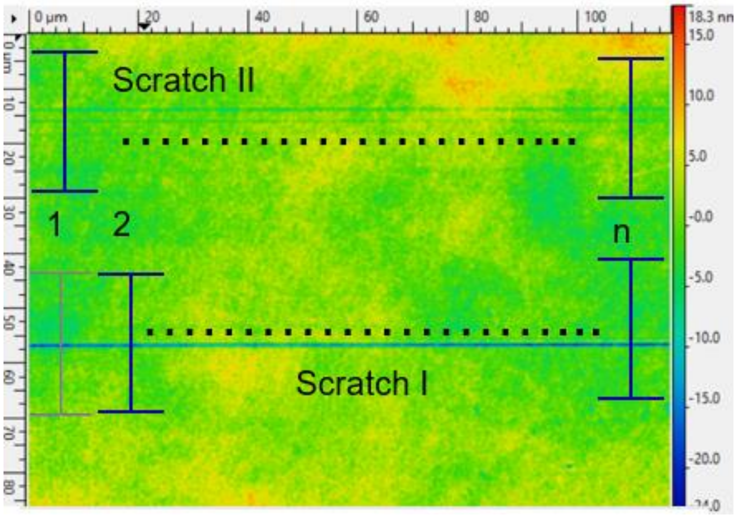

Figure 3.11: Method for obtaining scratch characteristics in a standard way. Average over a certain length (here 5μm) is taken throughout the length of the scratch. Average from 1st cross section up to nth cross section yield the scratch width, depth and pile-up height. The same process is repeated for other scratches.

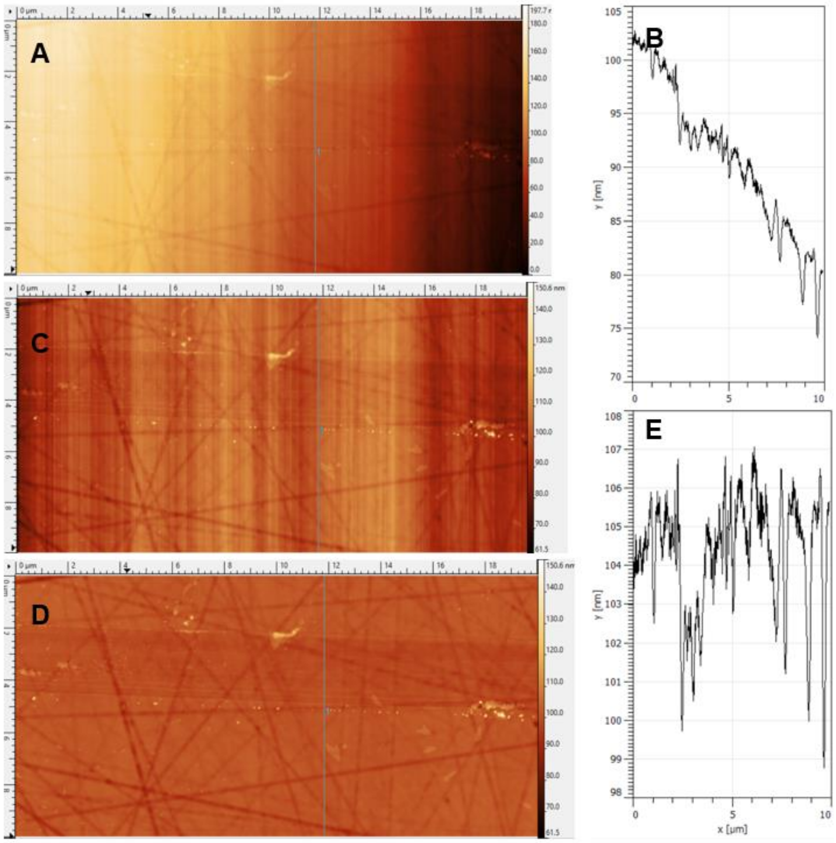

Figure 3.12: Background removal in AFM images. A: Raw data, B: Surface profile, C: Topography after plane removal, D: Surface after aligning rows vertically, E: Profile corresponding to C and D. Scratch although shallow is clearly visible.

3.2.4 Scanning Electron Microscopy (SEM)/ Energy Dispersive Spectroscopy (EDS)

SEM/EDS analysis was performed to study the morphology of scratches caused by single-asperity tests and confirm DLC spallation. ZEISS Sigma 300 SEM & Bruker QUANTAX EDS set-up were used. SEM micrographs were obtained with acceleration voltage of 1kV and working distance of 5.9mm. Sometimes 3kV voltage was used to speed up the image acquisition process. Aperture used is circular with 30µm diameter. For EDS measurements acceleration voltage was increased to 5kV and the aperture was increased to let more electrons interact with the EDS detector. Images were taken as long as the detector was measuring more than 1000 counts per second. Diamond tips (coated with single crystal diamond) were studied by applying 10kV beam energy.

4 Results and Discussion

4.1 Single asperity tests

4.1.1 Nanoindentation

Nanoindentations obtained by a Berkovich tip at four different strain rates (0.01,0.1,1,10 s^{-1}) and at two different maximum loads (2mN and 50mN) are discussed in this section. Load-displacement curves are illustrated in Figure 4.1 and the ratio of H/E for each condition is shown in Figure 4.2. Normalized displacement is defined as the z-displacement of the tip over the total coating thickness. Normalized contact depth is the contact depth that is reached with the Berkovich tip over the DLC coating thickness.

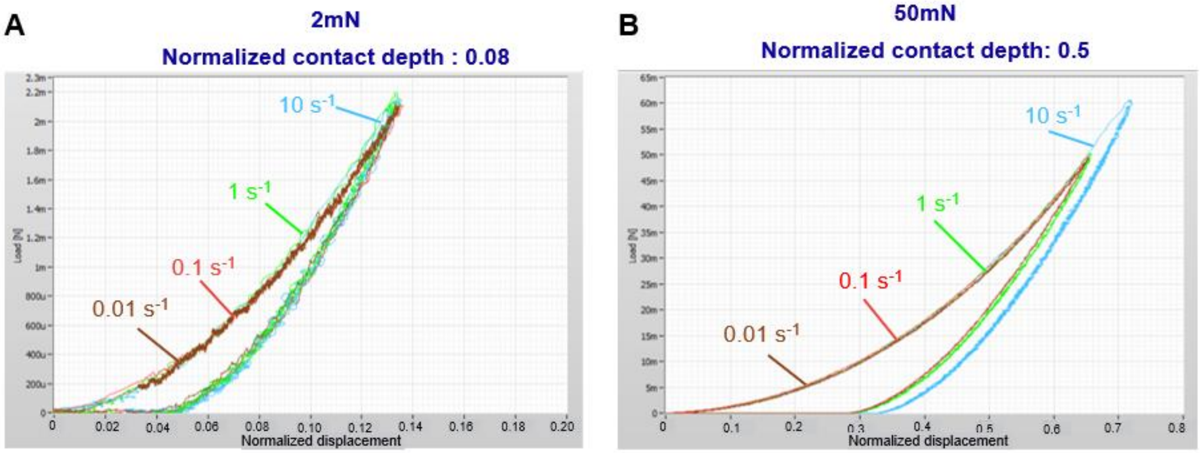

Figure 4.1: Nanoindentation results at different strain rates for (A) 2mN normal load and (B) 50mN. Load-displacement curves are identical with the exception of $10s^{-1}$ at 50mN, where a shoot of is observed attributed to equipment not being able to hold maximum load.

Nanoindentation results show that load-displacement curves under different strain rates are identical(Figure 4.1). The ratio of hardness to elastic modulus (also known as plasticity index [16]) shown in Figure 4.2 under 2mN maximum load, is strain rate independent, because the values of H/E for different strain rates lie within the error bars of the measurements. H/E values for 50mN is lower than that of 2mN, because as the load increases, subsurface stresses increase (shown in Table 4.5), and thus the mechanical properties of the substrate (SiC) are sensed. SiC has lower hardness than DLC, therefore H/E values for 50mN maximum load are lower than that of 2mN.

Plasticity index for 50mN maximum load exhibits a mild decreasing trend with increasing strain rate. However, the maximum and minimum H/E value is 0.067 and 0.061, respectively. Therefore, it is stated that for strain rates ranging from $0.01s^{-1}$ to $10s^{-1}$ H/E of DLC/SiC remains constant. Since nanoindentation results are derived from the deformation of the coating, it is deduced that the strain rate independency observed in the plasticity index indicates that DLC deformation is strain rate independent.

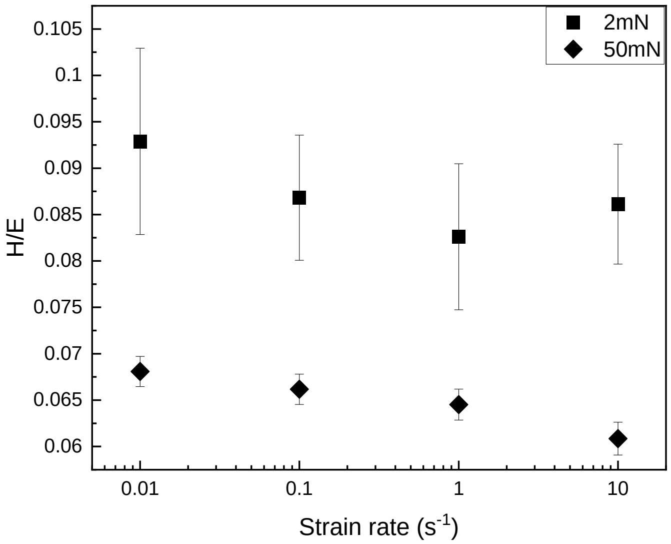

Figure 4.2: Hardness over Youngs modulus results (E/H) obtained from nanoindentation tests. H/E for 2mN(squares) and 50mN (cubes) remains stable in all strain rates. In 2mN case, H/E values for the different strain rates lie within the error bars of the measurement indicating DLC strain rate independence. Although a mild trend of H/E decrease in 50mN is observed the maximum and minimum value of H/E are 0.067 and 0.061 respectively. Therefore, it is stated that H/E of DLC is strain rate independent in both (2mN and 50mN) cases.

4.1.2 Scratching

Scratches created on DLC coated SiC wafer are illustrated in Figure 4.3 . Measurements performed at 10mN and 35mN under 1mm/s speed were discarded because they did not meet the success criteria as defined in section 3.2.2.2. As shown in Figure 4.4a-b the applied normal load was not held constant during scratching (e.g. force drop), therefore making the scratching conditions undetermined and thus unreliable. However, in the case of 100mN, 1mm/s a small force drop is observed which recovers after approximately 90μm of sliding, therefore making these measurements trustworthy. All other scratches met the success criteria (sliding speed and applied normal load equal to the expected values).

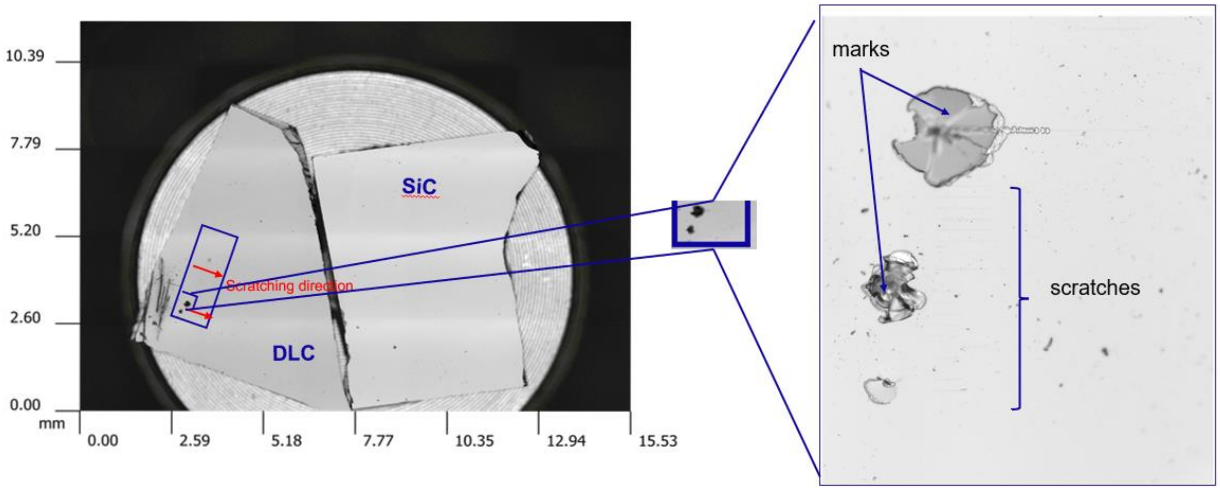

Figure 4.3: Scratches overview.

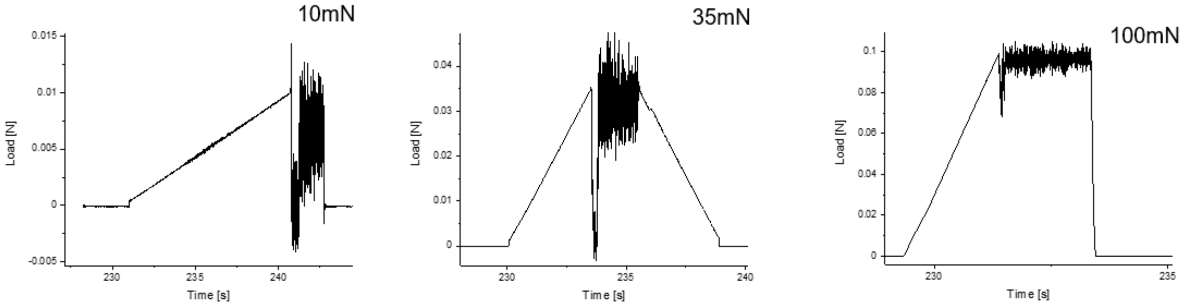

Figure 4.4: Representative Load-Time graphs under the 3 applied normal loads at the highest sliding speed (1mm/s). At 10mN and 35mN a drop in normal load is observed. Normal load does not recover up to the requested normal load.

Tip vertical displacement versus time during the three stages of scratching (pre, scratching, and post) mentioned in 3.2.2.1 revealed that DLC deformation is elastoplastic in the majority of tests as shown in Figure 4.5. This means that when the tip is plowing DLC, the front part of the tip is in contact (condition of a fully plastic contact), and behind the tip the DLC recovers elastically as described in section 2.2. Scratching is fully plastic if the green line (corresponding to z-displacement during scratching) of Figure 4.5 coincides with the blue line (z-displacement after scratching), meaning that the surface post scratching has the same depth as during scratching. In other words, elastic recovery is negligible compared to the plastic strains. This is observed at the condition of 10mN, 0.5 µm/s. Scratching is fully elastic if the tip before (red) and after (blue) scratching coincides. An example is seen at 100mN, 0.5 µm/s.

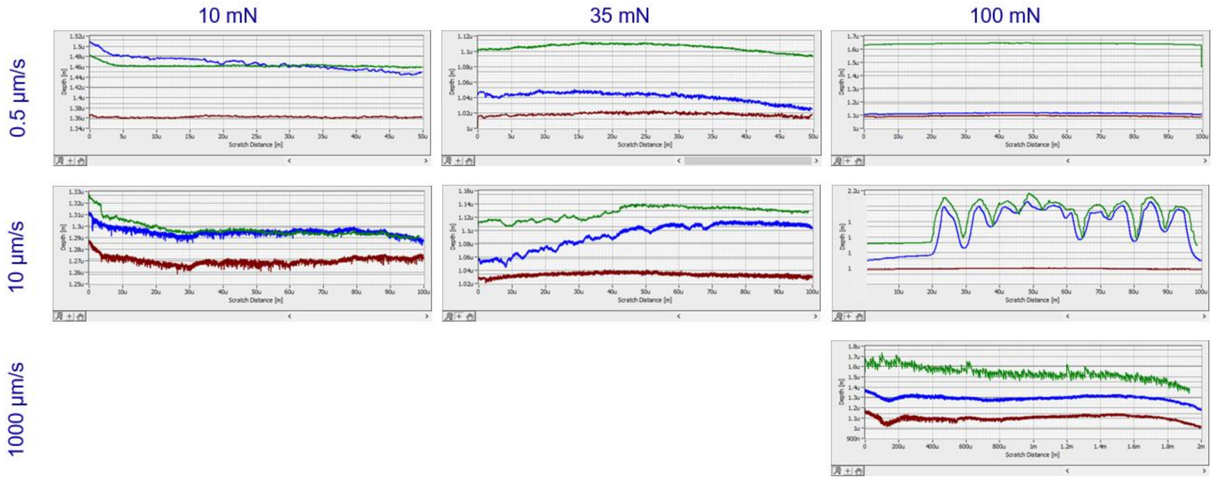

Figure 4.5: Displacement-Time data during scratching. Red signal shows the z-displacement of the tip before scratching, green signal shows tip's vertical displacement during scratching, and blue corresponds to tip's z-displacement after scratching.

A consequence of elastoplastic behavior is that scratch depth and width measured with surface analysis techniques (e.g. AFM) are the residual values. Elastic recovery makes the scratch shallower and narrower by material recovery in the vertical and lateral direction as described in section 2.2. This was also found by Kral et al. [58] ,where they presented a method to extract coating hardness from scratching test. In the current work, elastic recovery can be directly confirmed by observing Figure 4.5, where the difference between the scratching data (green lines) and the post scratching data (blue lines) is comparable to the observed plastic deformation (residual scratch characteristics). An indirect indication of the significant elastic recovery is by substituting the values of Table 4.2 in Eq. 2.10 of section 2.2 which yields a tip with radius of curvature even 3 orders of magnitude higher..

Before extracting results attention should be paid to the tip wear. Representative SEM images of the three used tips are illustrated in Figure 4.6. The cumulative scratching distance together with tip wear and the cumulative dissipated energy are listed in Table 4.1, and results are plotted in Figure 4.7, where it is shown that higher dissipation energy results in higher tip wear until tip wear reaches a plateau. Before the plateau is reached, the diamond asperity is running in, and when the plateau is reached scratching enters a steady state. A recommendation would be to fit the data of Figure 4.7 and predict the wear of a similar diamond asperity sliding against DLC under different load conditions.

EDS image of the adhered particles of Figure 4.6b reveal that these are silicon (Si) as shown in A.1.3.1. From SEM images it seen that the most worn tip (Figure 4.6a-b) exhibited wear of around 340nm and the less worn tip (Figure 4.6d) exhibited around 50nm of wear. The wear magnitude is calculated as the difference between the green circle and tip's surface. A more complete overview of SEM images investigating tip wear is presented in section A.1.3 of the Appendix. The order in which the tips were used are listed in A.1.1. In order to extract meaningful results from scratches, the tips should not be severely worn. The following methodology was followed to decide whether tip wear affects scratching behavior.

1. Scratches contaminated with debris along their lengths pinpoint a worn tip. This is easily observed by Confocal OM (see Section A.1.2).
2. When scratch morphology/topography change upon changing the tip, measurements before tip replacement are not representative of the real wear behavior indicating the effect of tip wear.

The measurements that did not meet the above conditions were the first 5 measurements obtained at 35mN and 100mN at 10$\mu m/s$. Therefore these measurements were discarded and they were not analyzed. The rest of the measurements were analyzed.

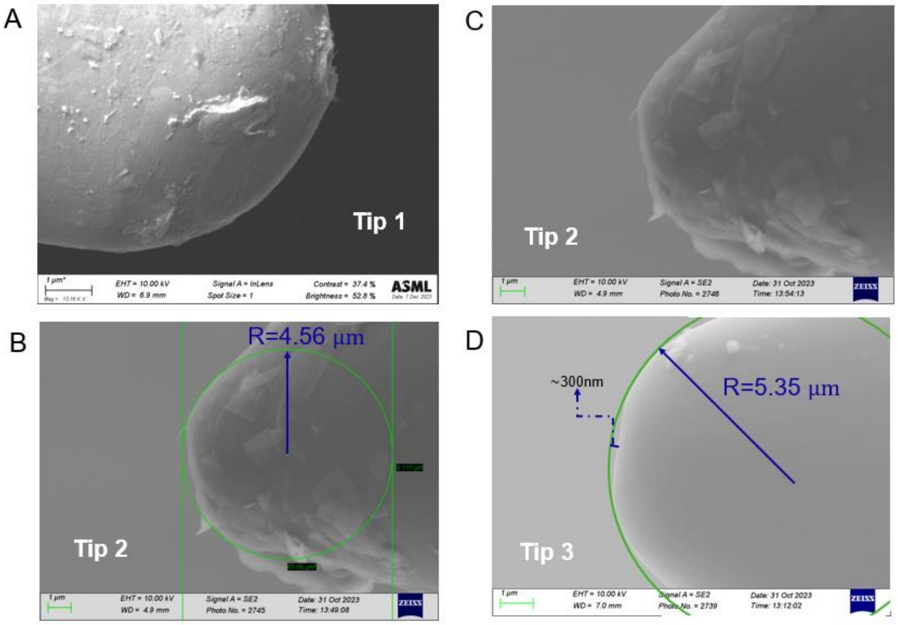

Figure 4.6: Diamond tip wear: (A) Tip showing least wear (tip number 1), (B) Tip number 2 showing the most wear and adhered particles, (C) Enlarged image of B, (D) Tip3. Green circles indicate the best fitted circle to the tip head. Initial tip radius was 5.67μm, 4.7 μm and 5.35 μm for tips 1 to 3. The sequence of tests can be found in section *A.1.1* of Appendix.

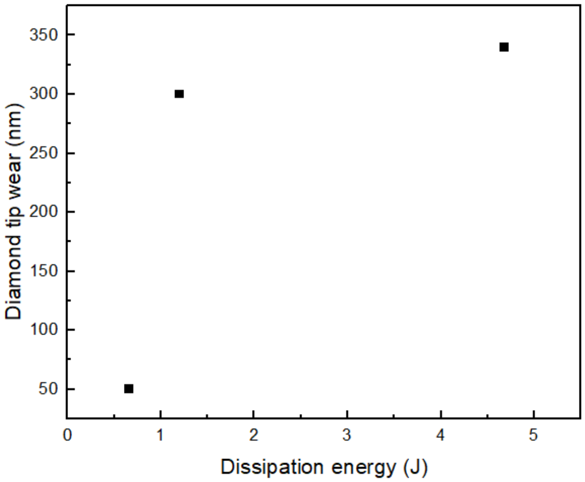

Figure 4.7: Dissipation energy-tip wear.

Table 4.1: Cumulative scratching distance and tip wear for the three tips used in single-asperity scratching tests.

Tip	Cumulative scratching distance (mm)	Cumulative dissipated energy (J)	Tip wear (nm)
1	20.3	0.66	50

2	19.7	4.68	340
3	18.4	1.20	300

Representative images of scratches as observed with HR-AFM are illustrated in Figure 4.8. A complete overview of HR-AFM images of the scratches can be found in section A.1.4 of the Appendix.

At normal load of 10mN in both strain rate conditions (0.5 and 10 μm/s) DLC shallow plowing is observed with wear debris at the edge of the scratch as shown in the first column of Figure 4.8. At 35mN (second column of Figure 4.8) higher debris are produced. At 100mN and 0.5μm/s shallow groove with small debris is observed, while for the case of 100mN and 10μm/s spallations occurred with through thickness cracks at spallated volumes. This difference in high load indicate that strain rate influences DLC abrasive wear performance at high loads. Behavior of scratch depth and width versus strain rate and load is illustrated in Figure 4.9 and Figure 4.10. Quantitative results are listed in Table 4.2. All scratches except the ones showing plowing and spallation showed constant width and depth throughout the scratching length. AFM data in Section A.1.4 support this statement. High error bars at 100mN 10μm/s are due to scratch characteristics not being constant throughout the scratch. Figure 4.11 shows the difference in scratch width and depth between 10μm/s and 0.5 μm/s measurements. At 10mN the difference in both scratch width and depth between the aforementioned sliding speeds is negligible. At 35mN, groove at 10μm/s becomes deeper indicated by the increase of green bar of Figure 4.11b. At 100mN, scratches at 10μm/s are narrower and deeper than those at 0.5μm/s, which is shown with the purple bars of Figure 4.11a-b. Therefore, Figure 4.11 shows that strain rate influences wear behavior as the load increase.

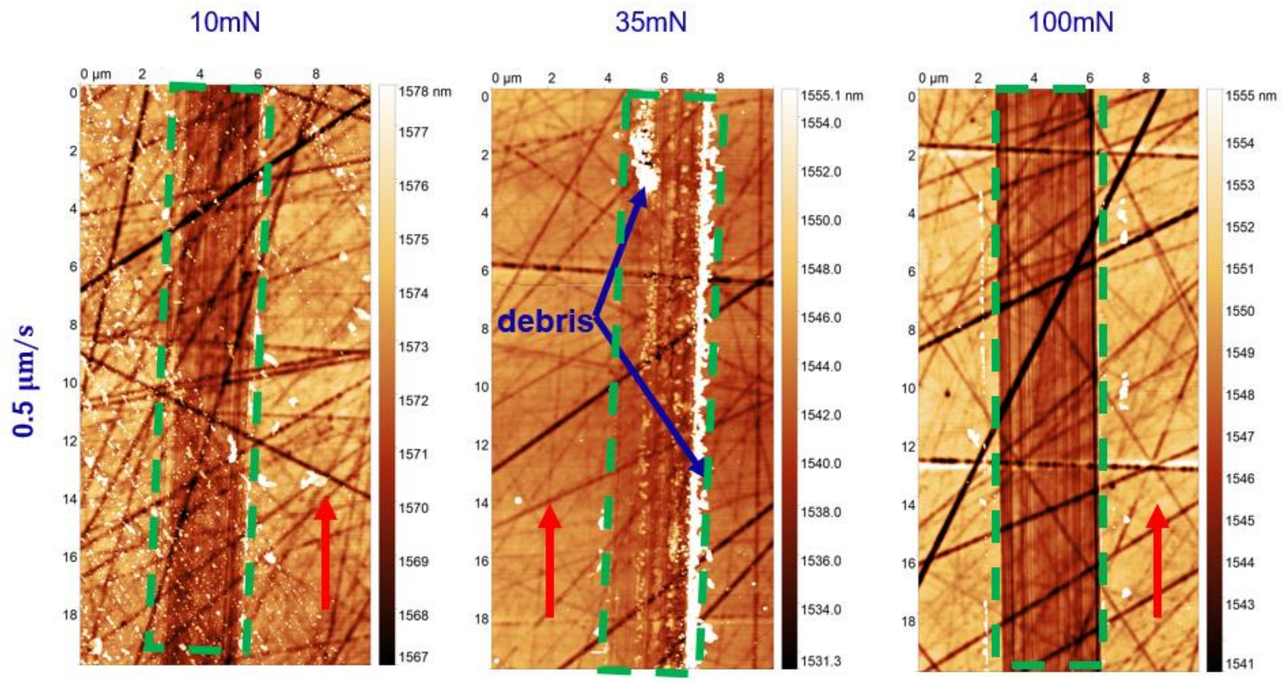

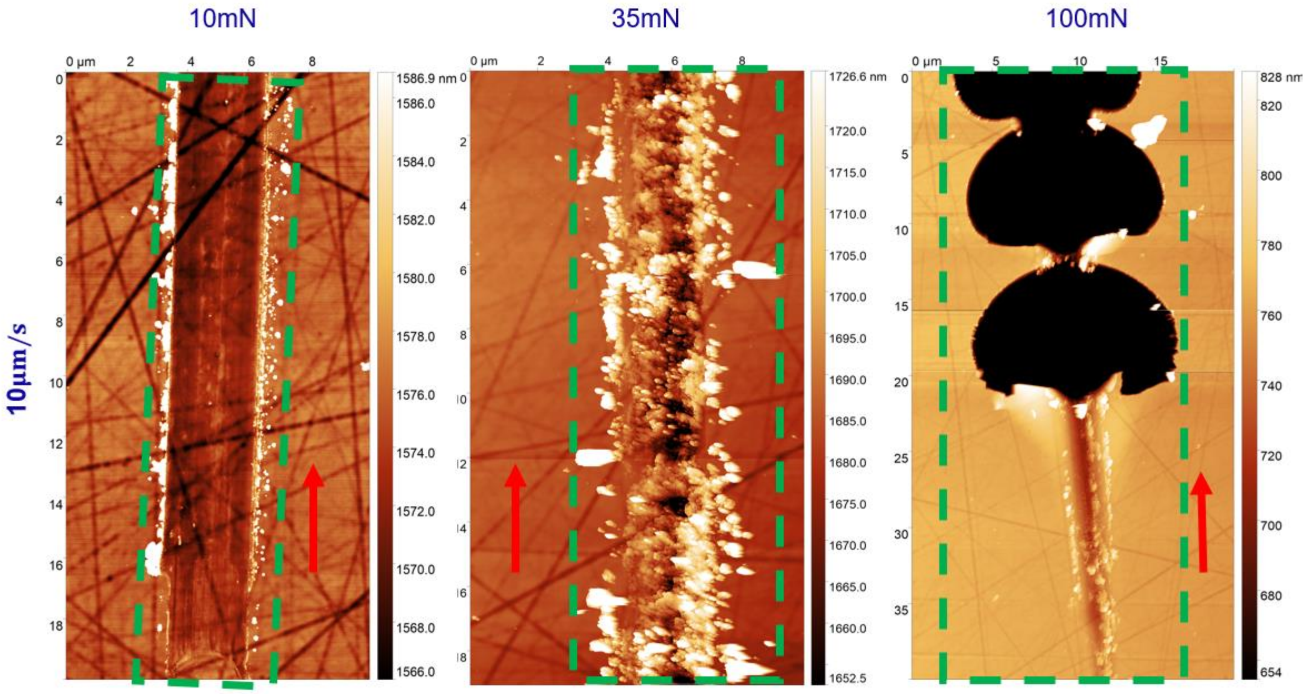

Figure 4.8: High-Resolution (HR) AFM images. Scratches lie within the green dashed rectangles. DLC failure observed in 10mN under 10 μm/s. Scale bar is adjusted to maximize contrast. Chips appear black due to being significantly deeper than plowed groove. Shown scratches at 10mN 0.5μm/s, 35mN 10 μm/s and 100mN,10 μm/s were observed with a fresh tip. Scratch direction is from bottom to the top annotated by the red arrow.

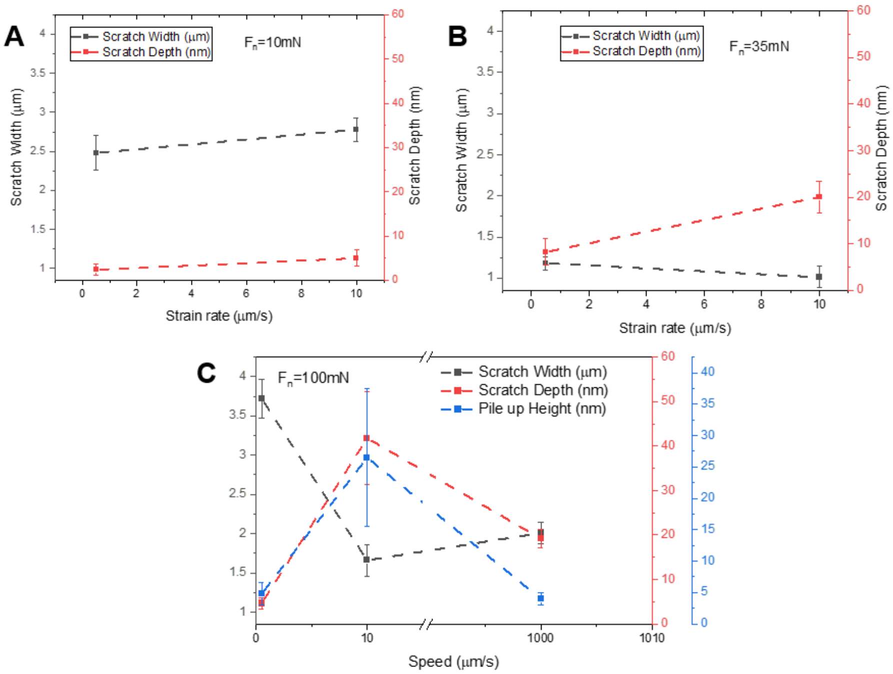

Figure 4.9: Double-Y diagrams showing scratch width (black) and scratch depth (red) for 10mN, 35mN and 100mN loads. In the case of 100mN small pile-ups are observed noted with blue. In case of 10mN and 35mN only debris are reported.

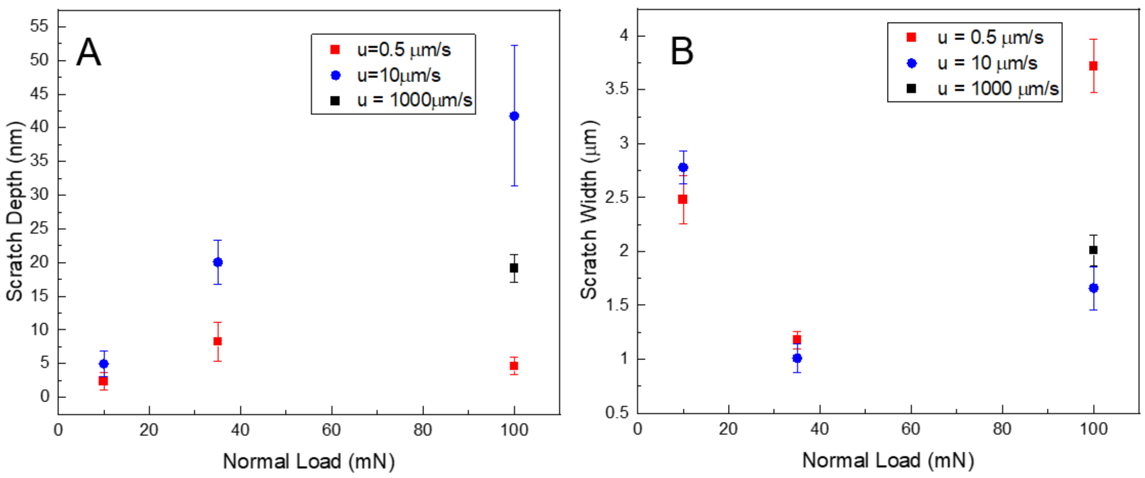

Figure 4.10: (A) Scratch depth and (B) Scratch width versus normal load. Scratch depth increases for all strain rates as the normal load increases, while scratch width shows a "v-shaped" behavior.

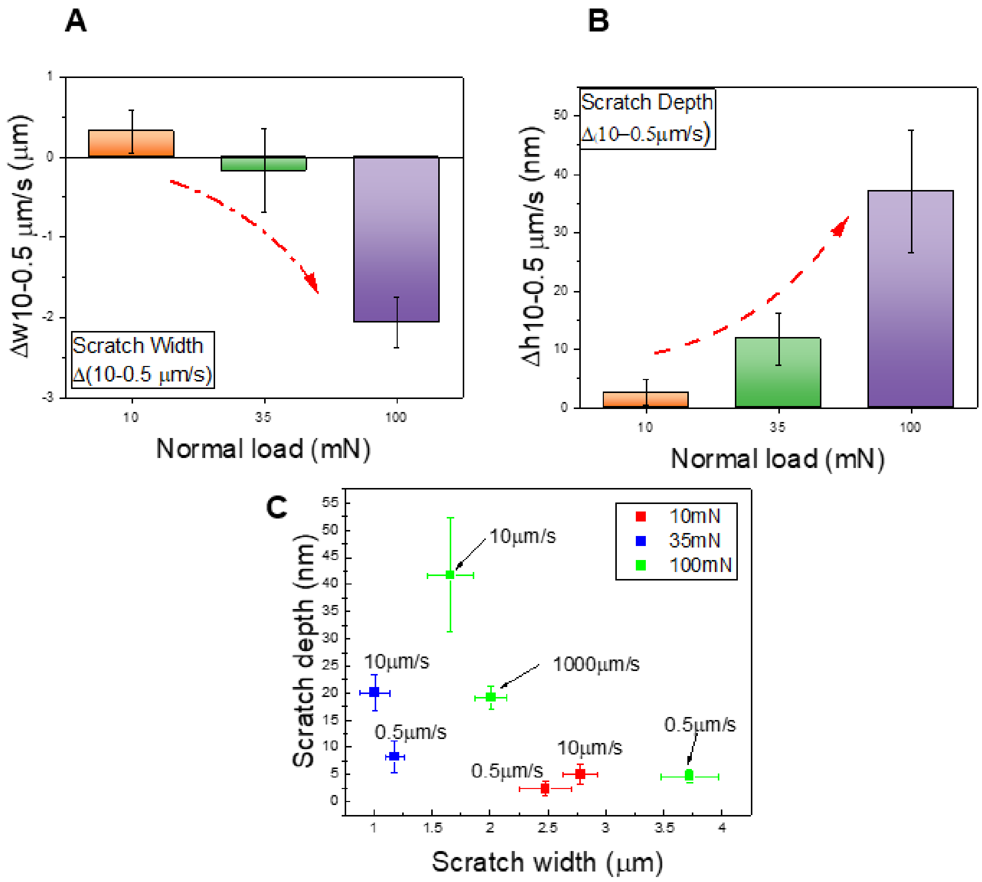

Figure 4.11: Difference between scratch characteristics at 10μm/s and 0.5μm/s in different normal loads. A: Difference in scratch width. Red arrow shows that upon increasing the load scratches at 10μm/s are narrower that those at 0.5μm/s. B: Difference in scratch depth, where red dashed arrow indicate that upon increasing the normal load scratches at 10μm/s are deeper that those at 0.5μm/s . C: Width versus depth diagram of scratches.

Table 4.2: Single-asperity scratching tests results. Reported 100mN, 10 μm/s data are average values before first spallation.

Sliding speed (µm/s)	**Scratch width (µm)**	**Scratch depth (nm)**	**Debris-pile-up height (nm)**
10mN			
0.5	2.48 ± 0.22	2.38 ± 1.24	2.71 ± 1.52
10	2.78 ± 0.15	4.97 ± 1.85	17.07 ± 6.44
35mN			
0.5	1.18 ± 0.08	8.24 ± 2.89	57.6 ± 23.90
10	1.01 ± 0.13	20.06 ± 3.33	27.5 ± 6.59
100mN			
0.5	3.72±0.25	4.64 ± 1.29	4.8 ± 1.81
10	1.66± 0.2	41.75 ± 10.43	26.47 ± 10.98
1000	2.01 ± 0.14	19.18 ± 2.04	3.98 ± 1.03

A closer analysis on 100mN, 10µm/s condition will be carried out. Topics to be discussed are:

I. Scratch development before failure.
II. DLC spallation and material lift-up features at the onset of spallation.

Figure 4.12 shows the first scratch were spallation occurred. From Figure 4.12a it is clear that the scratch progressivelly becomes wider and deeper indicating that the diamond tip was plowing deeper, increasing contact depth. Wear debris inside the groove are seen in Figure 4.12c-d, producing roughness inside the scratch groove. First spallation occurs roughly 20µm after start in all four scratches (see section A.1.1 for scratching test sequence). At spallations, the DLC is completetly removed (Figure 4.12e) and SiC is plowed (Figure 4.12d).

An interesting observation is that in order for the first spallation to occur, diamond tip has to plow DLC for about 20µm to possibly build up the required stresses for DLC delamination and spallation, while the rest of spallations occur almost instantaneously. In other words, when the first spallation occurs, stresses are reliesed evident from the through-thickness cracks oberved in Figure 4.12d). So, in order for the second spallation to occur it would be expected that certain scratching distance between the first and second spallation would be needed in order for the ncessary stresses for DLC spallation to be built up. However, it is obsrved that as soon as the first spallation occurs, the rest of them are being created succesively at a distance ~ 5µm. A computational work on the creation of DLC spallation would shed more light.A starting point could be the work of Mishra [59] , where the plowing of an elliptical asperity against Zn-coated steel is modelled. Adjustments on the loading conditions and materials included (diamond asperity sliding against DLC coating) can provide

In the work of [60], DLC spallation pattern was similar to this of the current thesis, and it was observed that upon decreasing the load the distance between succesive spallations increased up until a point where spallations stopped occuring. However, in [60] ramped load until 100mN was used while in the current work constant load of 100mN is used, thus the stress state during scratching between this work and [60] is different .

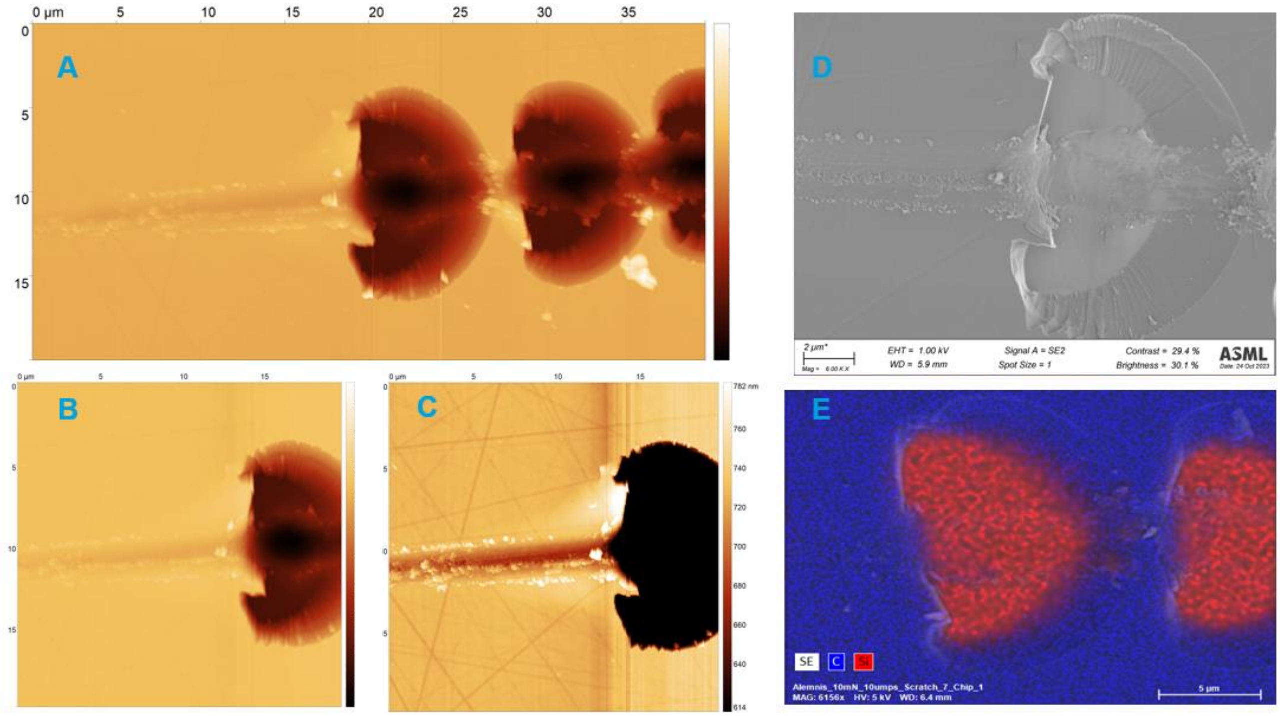

Figure 4.12: AFM and SEM/EDS images of plowing and spallations. (A) AFM image taken with 20nm/pixel resolution showing DLC ploughing, and first two spallations, (B) 10nm/pixel AFM image of plowing and first chip, (C) Image showed in B, with scale bar adjustment to increase contrast in the plowed region better revealing the groove morphology, (D) SEM image of area showed in B, (E) EDS image showing that at spallations DLC coating is completely removed exposing SiC.

All in all, qualitative and quantitative results on scratch development are shown in Figure 4.13 and Table 4.3, respectively. In Table 4.3 the average values of scratch depth, width and pile-up of for the four scratches are listed.

Initially the scratch is shallow (~35 nm) and narrow (~1.3 μm) and it becomes deeper and wider as scratching distance increasing. After roughly 20μm scratch width was ~2.3 μm and scratch depth almost tripled (100nm). In Figure 4.13a a pile-up is observed of around 20nm height, while at the onset of spallation the presence of adhered particles is observed.

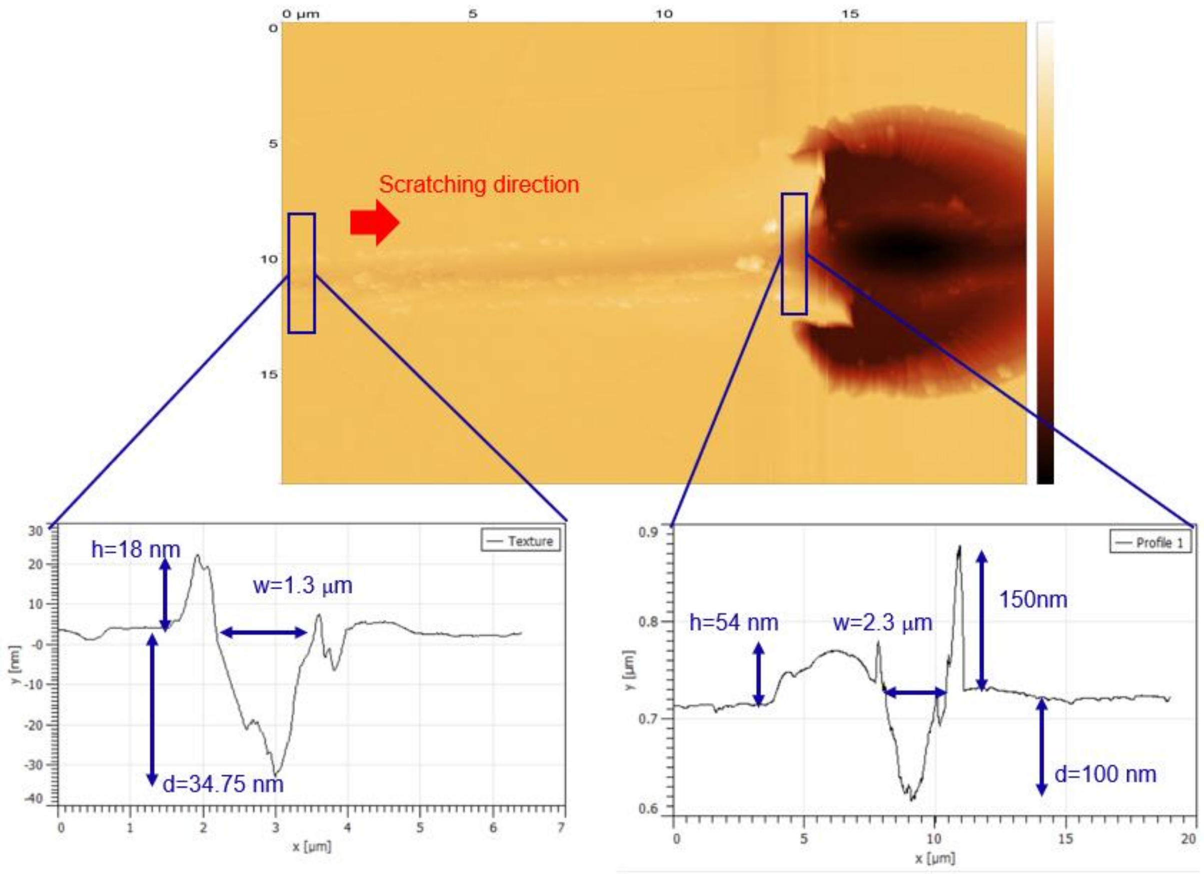

Figure 4.13: Scratch development during ploughing and at the onset of chipping. Scratch becomes deeper and wider with increasing sliding distance. Pile-up height also increases.

Table 4.3: Quantitative results of average scratch width, depth, pile-up height and pile-up width.

Avg. groove width (µm)	Avg. groove depth (nm)	Pile-up height (nm)	Pile-up width (µm)
Before failure			
1.66±0.12	21.34 ± 5.89 – 41.75 ± 10.43	11.78 ± 6.40	2.23 ±0.62
At the onset of failure			
1.98±0.27	86.12 ± 14.09	29.62 ± 9.0 (also >100nm features)	2.23 ±0.62
At failure			
12.03 ± 0.519	630-1000	111± 7.78	2.07 ±0.05

Finally, an investigation has been carried out to deduce whether the produced wear debris are adhered to DLC surface. In order to check that, sample was cleaned by a soaked tip with isopropanol. Pre and post SEM images capturing the three stages of 1) plowing, 2) failure onset and 3) failure are illustrated in Figure 4.14 . Results shows that high lift-up features at the onset of spallation are removed indicating poor adhesion of the particles with DLC surface. Particles inside the wear scar were not removed. Nevertheless, debris inside the wear scar do not contribute to DLC surface roughness, because they lie inside the groove. Further, during cleaning, particles were transferred by the cleaning tip which makes the spallation volume looking more contaminated after cleaning.

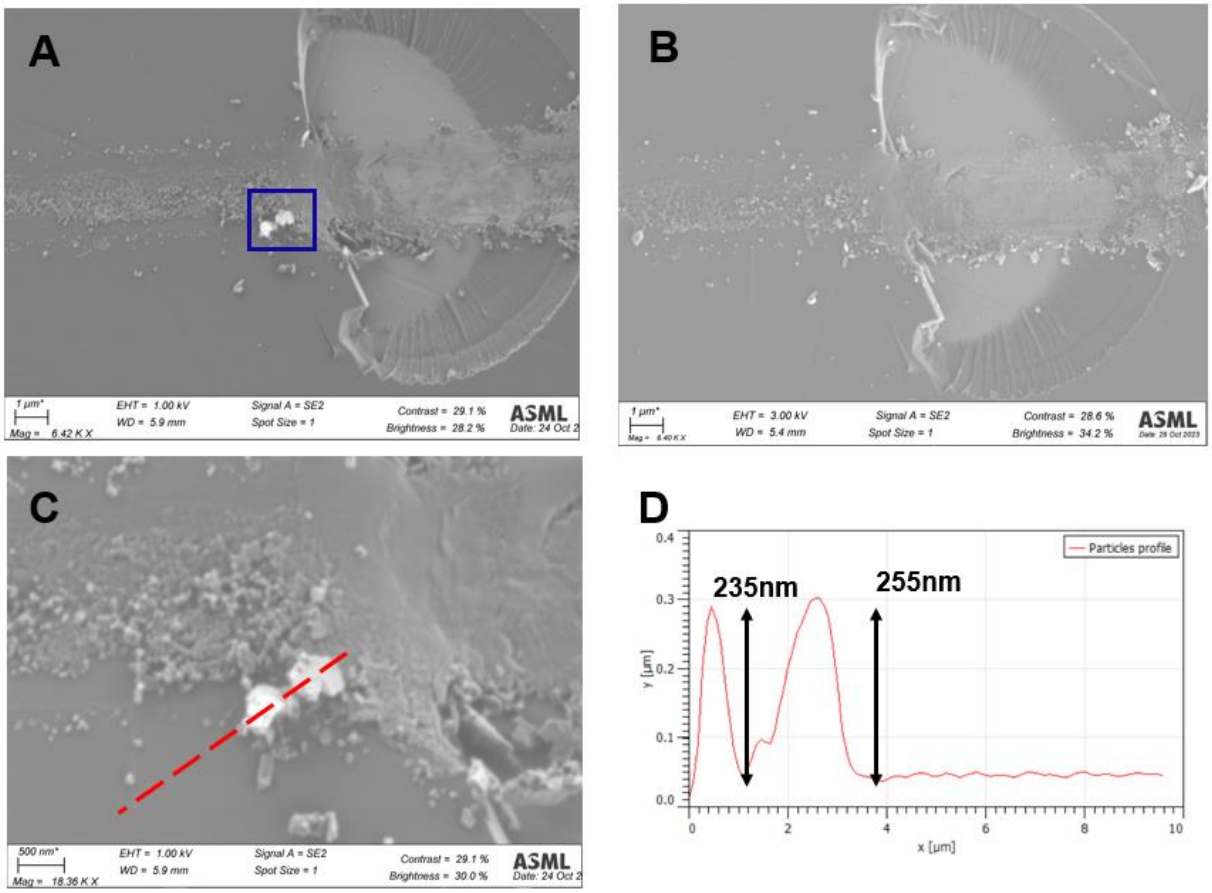

Figure 4.14: SEM images (A) before cleaning with isopropanol, (B) After cleaning, (C) Enlarged image of particles in A which were removed upon cleaning, (D) Particles profiles as obtained by Confocal OM.

4.2 Multi-asperity scratching tests

In this section the results from multi-asperity scratching tests are discussed. Four topics regarding DLC wear behavior are studied:

- Strain rate dependency,
- Interlayer influence,
- Influence of increasing load in scratch severity and density,
- Diamond asperity interference with DLC surface edge.

First, analysis with Confocal OM is performed in the area of the wafer with the highest variety of scratches, or in other words in the area that both deep and shallow scratches are observed. This area includes the 9 to 6 o’ clock positions. This is partially attributed to grit paper compliance caused by the mounting way as described in the section 3.2.2.2.

Tests performed on wafers of same architecture under different strain rate were performed. Wafers used were 1,2,5 and 6. The characteristics of the observed scratches are illustrated in Figure 4.15a, where each data point corresponds to a scratch. Higher strain rate results in scratches with broader distribution of depths and widths. However, the majority of scratches are less than 10nm deep and have a width ranging from 1 to 1.75μm. DLC wear behavior was shallow plowing with small pile-ups (<10nm high).

Further, the presence of asperities with different heights, radii and orientation make conclusions more difficult to be drawn from Figure 4.15a [59]. The normalized radius (radius over maximum radius) of diamond asperities at the 6 to 9 o' clock region of the grit paper is presented in Figure 4.15b. The radius of the asperities was measured as described in section 3.2.3. The majority of scratches have a normalized radius of curvature (RoC) around 0.3. The majority of scratches should be caused by the most frequently encountered asperities. Looking at Figure 4.15a, the majority of scratches have approximately 1.2μm width and 1-10nm depth. Therefore, these scratches are expected to be caused by asperities with normalized RoC of around 0.3.

Substituting the data of Figure 4.15a to Eq. 2.10 yields the normalized radius of asperities causing scratches of various widths and depths, as shown in Figure 4.15c. Scratches of width of about 1.2μm and depth less than 10nm are caused by asperities with normalized radius from 0.24 to more than 1. On the contrary scratches with $w \cong 1.5\ \mu m$ and $d > 15nm$, are caused by sharper asperities with RoC from ~0.10 to ~0.20, while scratches with width $>1.5\ \mu m$ and depth less than 10nm are caused by blunt asperities with normalized RoC>1. So, the different scratches in Figure 4.15a are not caused by the difference in strain rates, but rather from asperities of different radii scratching the DLC.

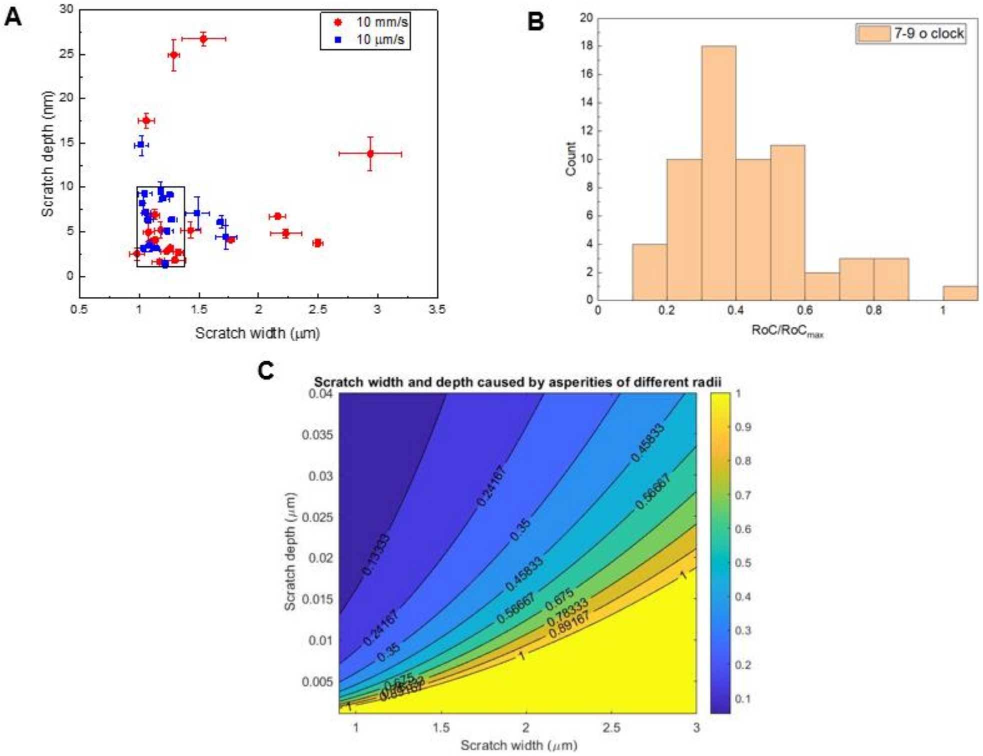

Figure 4.15: A: Scratch width versus scratch depth for DLC coatings of same interlayer thickness under 10mm/s and 0.010 mm/s strain rate. B: Normalized diamond asperity radius of curvature (RoC) at 7-9 o' clock position. C: Calculated asperities RoC causing scratches of different width and depth as calculated by Eq. 2.10.

The influence of interlayer thickness on DLC wear is presented in Figure 4.16. Scratch depth does not exceed 10nm, and differences in width are observed. DLC abrasive wear behavior remains plowing.

The effect of increasing the normal load on produced scratches is illustrated in Figure 4.17. Increasing load shows small difference in scratch depth and width. Under higher loading scratch density increases. This implies that under higher loading more asperities are brought into contact carrying the applied load. Therefore the load per asperity does not increase significantly.

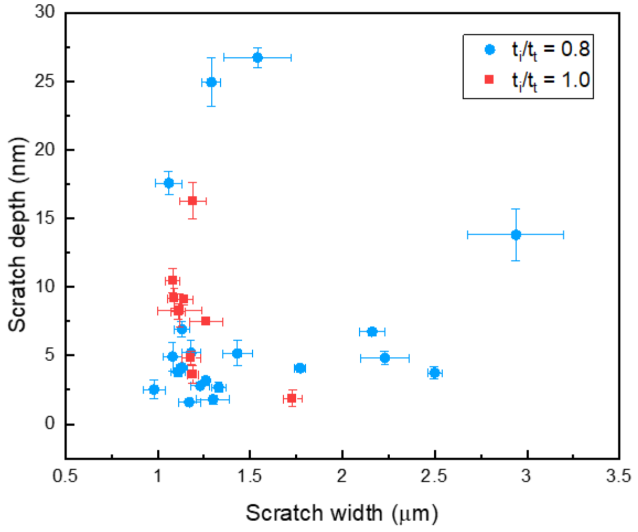

Figure 4.16: Investigation of DLC interlayer influence on abrasive wear.

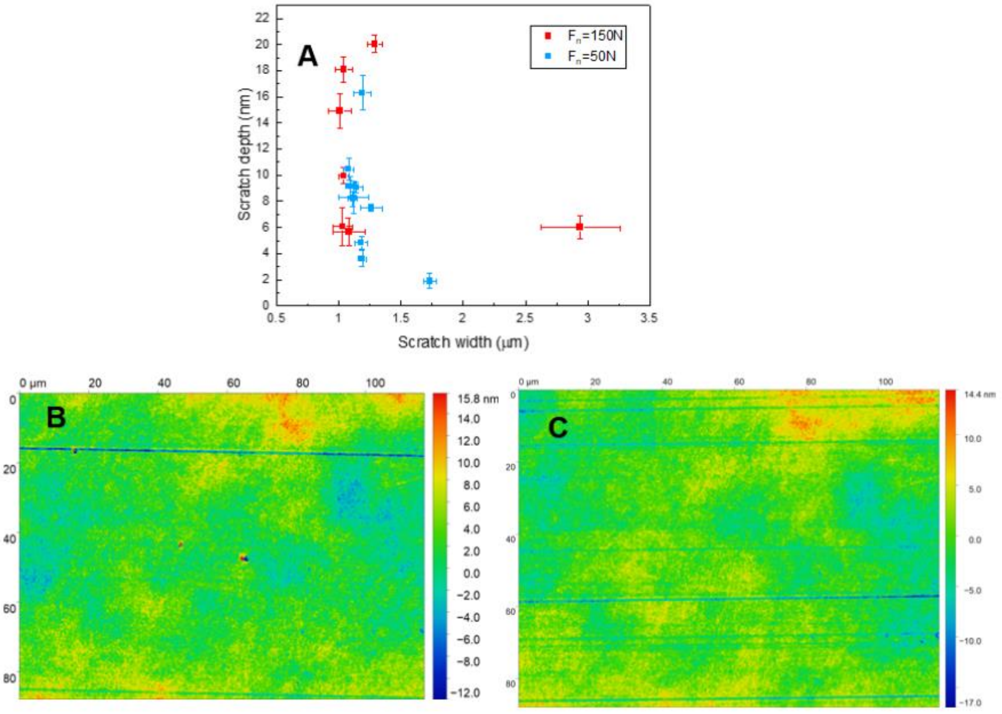

Figure 4.17: Difference in DLC wear behavior upon increasing load. (B): Low scratch density under 50N normal load, (C) Higher scratching density under 150N normal load.

4.2.1 Investigation of asperity interference at edge collision

The effect of grit paper collision with DLC wafers' edge was studied by placing the grit paper at a certain distance from the wafer's edge as described in Section 3.2.2.2 in Figure 3.9C-D. Results on DLC failure under different loading conditions and different initial distance (cases) from the edge are summarized in Table 4.4. Spallations occurred only in the 9 o' clock position and only for the cases when the distance from the edge was equal to the radius of the grit paper. In all cases, wafers were more damaged at 9 o' clock position and damage was decreasing from 9 to 6 o' clock position.

In the following paragraphs the observations will be explained. In order to follow the contents of this section the reader is referred to section 2.2, where the contact interference (ω) is discussed.

For case 1 and 3 the grit paper's global plane at 9 o' clock becomes horizontal just before collision happens. This is supported by calculations described in section A.4 of the Appendix. In other words, the asperities at 9 o' clock position are free-hanging. In case 2, approximately half of the grit paper's 9 o' clock region is already in touch with the wafer. This state of affairs is illustrated in Figure 4.18. Attention should be paid in the fact that Figure 4.18a illustrates the moment at which the 9 o' clock region of the grit paper is about to collide with the wafer's edge in cases 1 and 3, while Figure 4.18b shows the initial position of the grit paper as it is in case 2.

In the following, the rate of change of interference ω at asperities A and B of Figure 4.18 in cases 3 and 2 will be studied. At asperity A, the interference just before collision happens is maximum and decreases as it is "climbing" over the surface edge. The same applies for asperity B. When the asperity A is brought into contact with the wafer's edge its interference suddenly increases (due to the collision with the surface edge) and after it passes the wafer's edge it reaches a certain value. On the other hand, when asperity B comes into contact with the wafer's edge asperities in front of it have already been into contact(Figure 4.18d). This, coupled with the significant compliance of the grit paper/steel holder system makes the rate of change of ω of asperity B during impact to be lower than that of the asperity A. This difference in the rate of change of interference explains why DLC spallation happed in cases 1 and 3 and not in case 2.

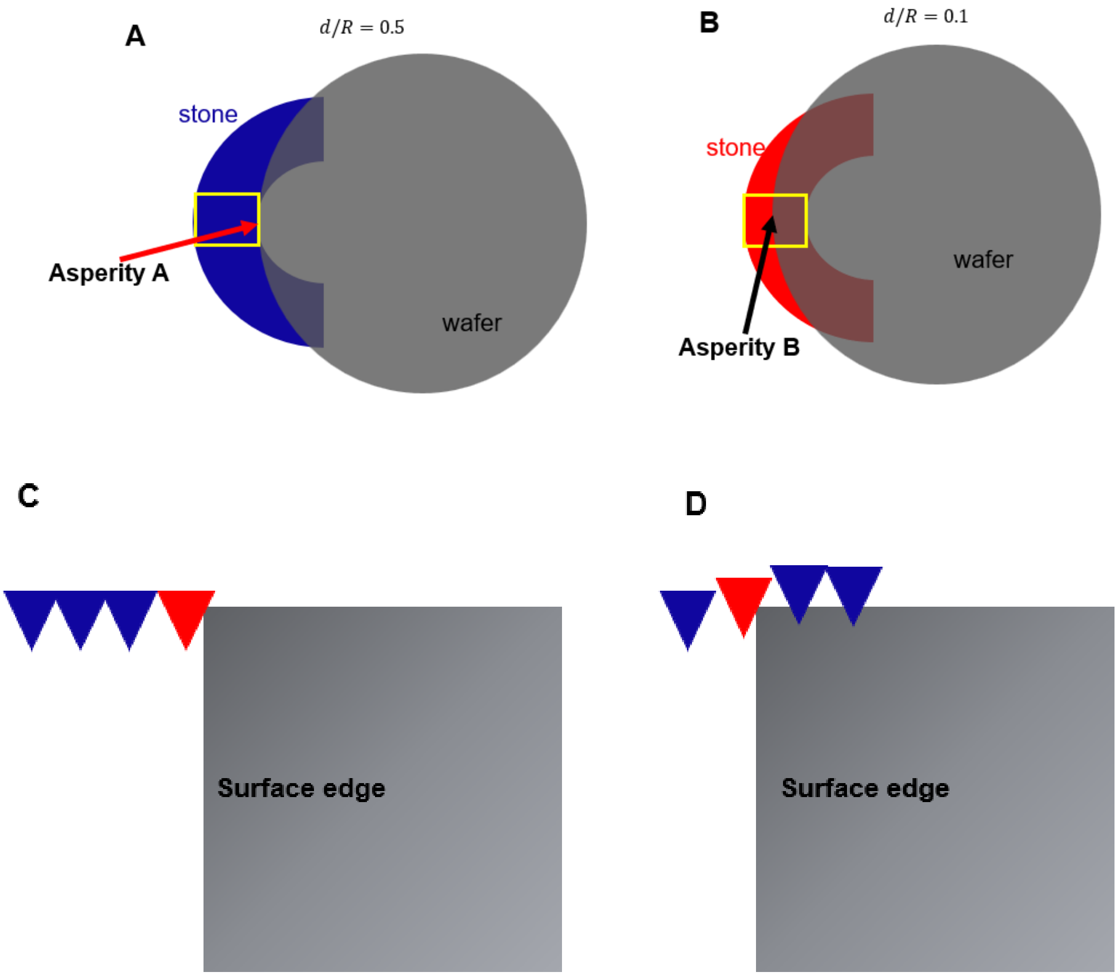

Figure 4.18: A-B: Rear part of diamond grit paper when colliding with wafer edge: Left: 9 o' clock region of the grit paper is free hanging when first interferes with wafer edge. Right: For case 2 the grit paper is initially partially supported at 9 o' clock position. Yellow rectangles show approximately the 9 o' clock region. Figures are in scale. C: Side view of the asperity A, marked as red, colliding with a surface edge. Initially the asperity has interference ω_M, which is the maximum value and it rapidly decreases as the asperity "climbs" through the edge. D: The rate of change of the asperity B is slower than that of A.

Table 4.4: Results of impact testing. Spallations occurred when distance from wafer edge was high enough so as grit paper's global plane at 9 o' clock becomes horizontal when colliding with the wafer edge .

Case	Wafer number	Distance from the edge/ grit paper diameter	Normal load (N)	Spallations at 9 o' clock position.
1	2,8	0.5	50	**Yes**
2	5,6	0.1	150	**No**
3	2	0.5	150	**Yes**

For all cases at 6 o' clock DLC wear was plowing in the edge and it increased towards the 9 o' clock area (where DLC spallation occurred) as illustrated in Figure 4.19. From Figure 4.18a, the rate of change of interference along the 6 to 9 o' clock position increases, so the impact from collision increases.

Notably, the pressure in 6 o' clock is higher than that at 9 clock, because the grit paper is less supported from the wafer. However, experimental evidence show that the wear at the wafer edge follows the reverse behavior, suggesting that the root cause of DLC spallation during edge collision cannot be the contact load during the impact. It is the rate of change of interference which drives the DLC spallation at the surface edge.

Moreover, from Figure 4.20 CoF increases as the grit paper becomes horizontal, and oscillates around the 0.5 value.

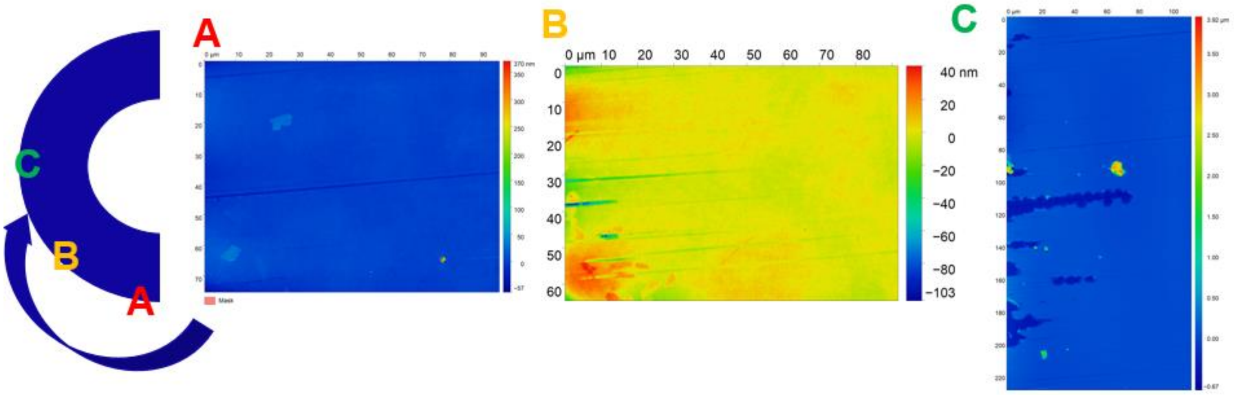

Figure 4.19: COM images showing that spallations occur in 9 o' clock position (noted with C), while towards 6 o' clock area scratch density and depth decrease resembling the case of sliding without edge collision.

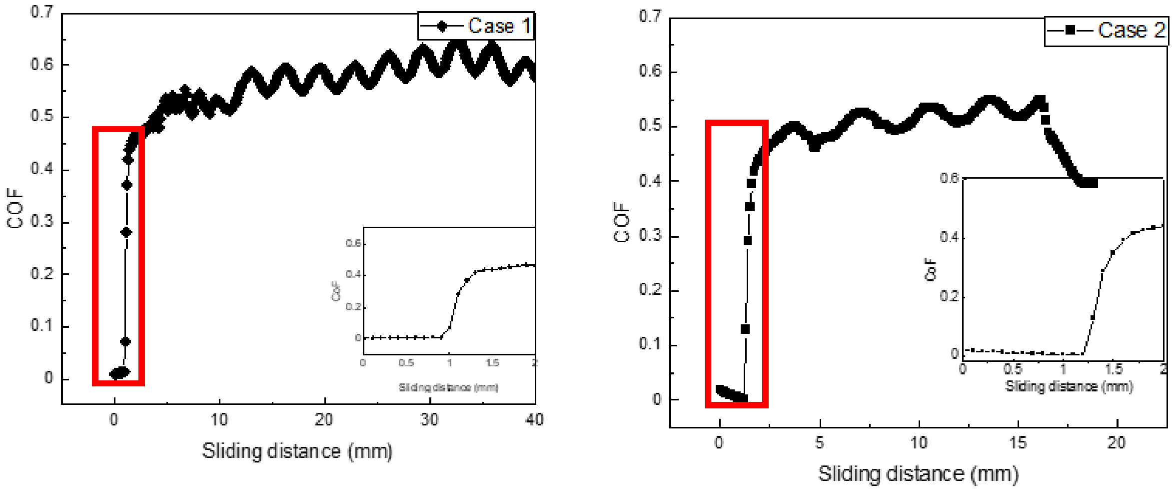

Figure 4.20: Left: CoF versus sliding distance in case 1. Similar behavior is seen for case 3. CoF increases rapidly in the first 2mm of sliding as the rear part f the grit paper climbs through the edge of the wafer reaching values of approximately 0.6. Right: CoF Vs sliding distance in case 2, where similar behavior in the first 2mm of sliding is observed. However, CoF takes a maximum value of 0.5. No differences in friction between the two cases are reported.

4.3 Discussion

4.3.1 Load dependent strain rate wear

Figure 4.9 and Figure 4.11 include the main take outs of single-asperity scratching tests. From Figure 4.9 a non-linear strain rate behavior is seen under 100mN. Figure 4.11 shows that strain rate influence on DLC abrasive wear behavior increases as load increases. The last observation can be explained in terms of subsurface shear stress magnitude and DLC/SiC interface adhesion strength.

First, the contact load regime was checked using Eq 2.7 and Eq. 2.8 (for ω_1 and ω_2). Substituting material's properties yield the following results:

$$\omega_1 = 92.4\,nm \tag{4.1}$$

$$\omega_2 \geq 5\,\mu m \tag{4.2}$$

In the current work, where the contact is elastoplastic (Figure 4.5),interference for the different loads used in single-asperity scratching tests can obtained by Eq. 2.2. In order to have an estimate of the shear subsurface stress (τ_{rz}) at the DLC/SiC interface Eq.2.4 and Eq.2.5 need to be calculated and substituted in Eq.2.6 These equations are valid for elastic contact mechanics and can provide just an estimate of the magnitude of subsurface stresses. By doing so, the results listed in Table 4.5 are obtained. The high values of the maximum contact pressure pin point that significant plasticity occurs. This is also evident by the fact that in all cases the applied normal load is sufficient to cause subsurface yield (indicated by the P_Y parameter). Further, the mean pressure (P_A) lies into a more reasonable values, since it is based on an elastoplastic contact. The depth of maximum subsurface stresses (4th row of Table 4.5) increases with load and it seems that in loads >10mN SiC substrate is significantly loaded. Last, subsurface stresses as obtained by Eq. 2.4-2.5 are expected to be in the order of GPa and increasing as normal load increases. Taking into account plasticity phenomena it is expected to further lower these values.

Table 4.5: Maximum contact pressure as obtained from elastic theory, Mean contact pressure as gained by elastoplastic theory, τ_{rz} at the DLC/SiC interface and normal load needed to initiate subsurface yield.

Parameter	F_n=10mN	F_n=35mN	F_n=100mN
Maximum contact pressure in elastic contact p_0 (GPa)	14.86	22.56	32.02
Mean contact pressure in elastoplastic contact P_a (GPa)	9.65	12.43	14.85
Subsurface shear stress (τ_{rz}) at the DLC/SiC interface (GPa)	3.55	6.45	9.46
Depth of maximum subsurface stresses/coating thickness	0.88	1.34	1.92
Normal load required for subsurface yield P_Y (mN)	10	35	100

Therefore, the observation that DLC abrasive wear is strain rate sensitive in high loads is explained as follows: Under mild(~10mN) loading, subsurface stresses even if they reach the DLC/SiC interface their magnitude is small compared with the adhesion strength of the DLC/SiC interface. As load increases, shear subsurface stress also increases, as shown in Table 4.5 . Therefore, increasing the normal load also increases the shear stresses at the DLC/SiC interface which start approaching the interfacial adhesion strength, which for the studied samples is unknown. As a result, the wear behavior at high loads exhibit strain rate sensitivity. The discussion on the observed non-linear strain rate DLC wear dependence at 100mN will take place in the next section.

Finally, an important conclusion is the following: For DLC/SiC applications where the normal load per asperity is close to 10mN single-asperity scratching tests are representative of engineering applications where strain rates are orders of magnitude higher because DLC/SiC wear behavior was identified as strain rate independent. However, as application's load per asperity increases the difference between single-asperity strain rates and the application's strain rate, making single-asperity tests results non representative.

4.3.2 Nonlinear strain rate dependent wear

Further, the non-linear strain rate behavior observed in 100mN (Figure 4.9) needs to be explained. DLC plastic deformation is strain rate independent as shown by nanoindentation tests. The answer to understand the non-linear strain rate wear behavior was searched in a number of areas without particular success. Areas studied include:

- Failure mechanics.
- sp2 to sp3 (rehybridization) conversion caused by increased stresses at the interface.
- Strain rate dependent subsurface stresses.
- Dynamic loading and the effect on subsurface stresses.

A detailed description of the motives to investigate these areas is given as follow.

DLC fracture investigation

First, strain rate influence on the energy balance between energy release rate (G) and crack resistance (R) was investigated. The reason why the energy balance was studied to explain the non-linear strain rate wear behavior of DLC is because spallation is accompanied by through-thickness cracks. Therefore, if the potential energy that triggers crack propagation (G) is strain rate sensitive, then DLC failure will also be influenced. Also, if crack resistance energy is strain rate sensitive similar picture is expected.

Because elastoplastic loading is studied, energy release rate (G) is substituted by the energy definition of J integral. J is the negative derivative of potential energy over crack increment and R depends on surface energy as discussed in Chapter 4 of [61].

Second, strain rate sensitivity of stresses and strains at crack tip were studied. Elastic-Plastic Fracture Mechanics (EPFM) was used because of the elastoplastic loading regime of DLC during scratching. According to Hutchinson, Rice & Rosengren (HRR) model stresses and strains for a certain J value are described by Equations 4.3 and 4.4, respectively [61].

$$\sigma_{ij} = \sigma_0 \left(\frac{E}{a\sigma_0^2 I_n} \frac{J}{r} \right)^{\frac{1}{n+1}} \overline{\sigma_{\imath\jmath}}(\theta, n)$$

4.3

$$\epsilon_{ij} = a\,\sigma_0 \left(\frac{E}{a\sigma_0^2 I_n}\frac{J}{r}\right)^{\frac{n}{n+1}} \overline{\epsilon_{ij}}(\theta, n)$$

4.4

, where σ_0 is the yield strength, E Young's modulus, α a constant, J is the value of the J-integral, r is the radial distance from the crack tip, n is strain hardening factor with n=1 denoting purely elastic behavior and $\overline{\sigma_{ij}}(\theta, n)$, $\overline{\epsilon_{ij}}(\theta, n)$ being functions of the angle θ from the axis of crack propagation and n. From HRR model stresses and strains are not influenced by the imposed strain rate. Other models taking into account the strain rate sensitivity of crack tip propagation velocity and thus on stresses and strains may shed more light into the non-linear strain rate dependent DLC wear behavior.

The drawback of such analysis are that in our case the system investigated is a ceramic coating. Therefore, theories describing fracture mechanics on polymers or steels need to be taken with caution. Further investigation on fracture mechanics of DLC coating is beyond the scope of this thesis.

Dynamic loading and impact

Under high speed sliding, the sliding velocity can reach the speeds of the elastic wave propagation and therefore contact (and thus subsurface) stresses are affected by the material's inertia. Under dynamic loading, stress waves are transmitted through the impacted material [62]. Dilatational (or pressure or longitudinal), distortional (shear or transverse) and Rayleigh waves are propagated with speeds c_1, c_2 and c_3, respectively.

$$c_1 = \left(\frac{2(1-v)G}{(1-2v)\rho}\right)^{\frac{1}{2}}$$

$$c_2 = \left(\frac{G}{\rho}\right)^{\frac{1}{2}}$$

$$c_3 = \alpha c_2$$

, where α is the root of the following equation:

$$(2-a^2)^4 = 16(1-a^2)(1-\frac{a^2 c_2^2}{c_1^2})$$

c_1, c_2 and c_3 are close to the speed of sound. Therefore, 10$\mu\mathrm{m/s}$ sliding speed (or equivalently strain rates) is 8 orders of magnitude lower. However, such resonance can take place in rapid crack propagation, where the crack tip propagates near the Rayleigh speed. Therefore, it may be that crack tip propagation speed increases with imposed strain rate. When crack tip velocity approaches c_3 stress waves are transmitted through DLC reaching the DLC/SiC surface, increasing DLC receptance and stress at the interface causing DLC spallation. Under higher strain rates, crack tip velocity also increases, moving away from the resonance value of c_3.

Further, presence of metal adhesion layer could explain strain rate dependence. For example Cr plastic deformation exhibit significant strain rate influence [63]. In the case of adhesion layer absence, carbon-carbon and carbon-silicon bonds occur in the DLC/SiC interface. In the work of Bai and Yu [64], it is deduced that interfacial failure of DLC films is induced by sp3 to sp2 transition during cyclic tensile tests. However, hybridization is associated with breaking and creating atomic bonds. Bond creation is thermodynamically driven and not driven from kinetics. Therefore rehybridization is not expected to contribute to strain rate dependent behaviors.

Following the explanation followed in section 4.3.1, strain rate dependent wear behavior can be analyzed in terms of subsurface stresses. Under high loads, subsurface (shear) stresses reach and exceed the DLC/SiC interface. Therefore, the following parameters influence DLC/SiC abrasive wear behavior:

- DLC bulk properties
- DLC/SiC interface mechanical, and physicochemical phenomena.
- SiC mechanical properties.

SiC load carrying capacity is not expected to be strain rate dependent. Therefore, the complex interplay between nanomechanical and physicochemical phenomena taking place in the DLC/SiC interface may exhibit a strain rate dependency. Nanomechanical phenomena include crack formation, and the stress state of the interface, while physicochemical phenomena include those governing the adhesion between DLC and SiC such as surface energy.

Further study needs to be done on the phenomena taking place in DLC/substrate interface in order to understand the non-linear strain rate dependency. First, it is recommended that scratching tests with same materials and parameters as those used in the current thesis should be taken under: 100mN 100μm/s and 500μm/s conditions. Such measurements combined with the ones described here will better analyze the non-linear strain rate wear behavior.

4.3.3 DLC qualitative wear behavior

DLC/SiC abrasive wear behavior, has been identified to be strain rate dependent in high normal loads per asperity (~100mN). The wear behavior of DLC on SiC versus diamond under constant normal load has been found to be predominantly plowing with wear debris inside and at the edge of the wear track. Literature shows particle-free wear scars [60] [65]. In the work of Bird et.al. [60] scratching under ramped load with 1μm and 5 μm diamond conical tips versus DLC on Si substrate with sliding speed of 0.5 μm/s were carried out. In the single-asperity scratching tests performed in the current thesis, the normal load was held constant during the whole scratching distance. Also, in our case the substrate was SiC instead of the much softer Si, which is expected to affect scratching at high loads (~100mN).

High material lift-up occurred at the case of 100mN, 10μm/s at the onset of DLC spallation (Figure 4.13). An explanation could be that at the onset of failure DLC is delaminated and buckled in the DLC/SiC interface therefore producing material lift-up features. FIB cross sections can investigate this hypothesis. Presence of wear debris-particles indicate material loss. Also, these particles may play the role of abrasives, increasing locally the stresses and consequently subsurface stresses. The higher density of wear debris at 35mN, 10μm/s compared to 35mN, 0.5μm/s may explain why DLC failure takes place at 10μm/s condition. However, the lack of evidence for low loads at 1mm/s prevent us from better understanding the non-linear wear behavior at 100mN.

4.3.4 Multi-asperity tests

Multi-asperity scratching tests where grit paper started on top of DLC surface as shown in Figure 3.9a-b performed under 50N normal load are in agreement with the 10mN results of single asperity tests. In both cases shallow plowing is observed with no strain-rate dependence. 10mN normal load at single-asperity scratching tests are equivalent with applying 180N normal load during multi-asperity scratching between the grit paper and DLC wafer as described in Section 3.2.2.2. Therefore, in multi-asperity scratching, 50N normal load produce similar DLC wear compared to the 150N normal load.

This outcome may be of use in engineering applications where a given load per asperity is needed. However, knowing the load per asperity in an engineering application is rather difficult since multi-asperity contacts take place with asperities of different geometries and heights. It is easier to think about the macroscopic applied normal load, which is a controlled variable rather than the normal load per asperity. From our work it is suggested that lower macroscopic normal loads cause similar wear at single-asperity level than the macroscopic normal load calculated by scaling calculations. Reversely, lower macroscopic normal loads can produce higher abrasive wear than expected on single-asperity scale. The range of macroscopic normal loads that yield similar single-asperity scale tribological behavior can be studied. A recommendation for future study could be to investigate the influence of asperity height distribution to the aforementioned load range.

The explanation of the effect of surface roughness during a ramped load scratching test is based upon the theory proposed by Greenwood &Williamson [66]. Similar is the work of Tabor [67], where the contact of rough surfaces was modelled . More precisely, as normal load increases more asperities are brought into contact carrying the applied stress. Therefore, normal load at asperities that are already in contact increases either at decreased rate or remains constant as other asperities start carrying the applied load. Upon further loading depending on the asperity distribution the following can happen:

- In the extreme case of two distinct distributions (only short and tall asperities) the taller asperities will carry the load and penetrate the surface deeper. This will stop when the shorter asperities come into contact with the scratches surface. Until this happen, tall asperities will already have penetrated deeper, making deeper and wider grooves. Higher penetration depth result in higher subsurface stresses in coating-substrate interface. Thus, coating may be delaminated before the short asperities come into contact.
- If asperity height distribution is homogeneous, then small increments in normal load would result in new asperities start being in contact. Therefore, taller asperities will not penetrate further into the surface because load is accommodated by fresh asperities that are brought into contact. When all the asperities are in contact further loading will result in asperities plowing deeper making deep and wide scars.

The difference between the two scenarios is that in the former case scratches become deep and wide at lower loads. Therefore in the first case the range of macroscopic loads giving similar single-asperity wear is smaller than that of the second, where asperities are having a homogeneous height distribution. For our case it is deduced that grit paper has homogenous asperity height distribution since single-asperity wear behavior remains similar in the range of 50-150N. Experimentally it is confirmed that scratch density change between scratching under 50N and 150N normal load (Figure 4.17), which supports the beforementioned phenomenological approach.

4.3.5 Wear during grit paper-wafer edge collision

Last, understanding the effect of grit paper's rate of change of interference during edge collision is of importance. Collisions of free hanging-asperities at the rear part of the grit paper at 9 o' clock caused DLC spallation while from 9 to 6 o' clock position less wear is observed. Mild wear takes place when the colliding asperities exhibit compliance and their rate of change of interference during collision increases smoothly.

Furthermore, the following link between grit paper's asperity interference and asperity height can be made: "Higher interference is equivalent to as if the asperities of the grit paper are taller. Lower interference yields an equivalent state of shorter asperities."

From our work it is suggested that DLC spallation was caused by the high rate of change of asperity interference at 9 o' clock position, rather than the applied normal load. This is evident from the results regarding the wear evolution from 6 to 9 o' clock presented in 4.2.1.

In the following part of this section the equation of motion of a spherical asperity (with radius R) of a grit paper like the one used in section 4.2 colliding and "climbing" an edge will be derived. A similar work, where the collision of two spherical asperities belonging to two surfaces in relative lateral motion was studied in chapter 4 of the work of Boucly [68] . The differences between Boucly's consideration and the current model is that this model is analytical and in this work the counter surface is a surface edge, modeled as a step function at x=0.

Figure 4.21 illustrates a spherical asperity colliding with a surface edge at the time moment $t=t_0$. A force F is acting along the direction of the impact spot and the center of mass of the asperity. This force is analyzed in two perpendicular forces, one at x-axis and one at z-axis, which are noted as f_x and f_z, respectively. Since in a single-asperity scratching tests sliding velocity is constant this means the sum of forces at the x-axis is zero. In other words, scratching test is displacement controlled which means that the scratching test setup "senses" the opposing lateral (friction) force f_x and compensates it in order to keep the sliding velocity constant.

At z-axis, 3 forces are acting:

- f_z: due to the asperity-edge collision
- $f_{spring} = -kz$: due to the fact the compliance caused by the presence of the adhesive between the steel holder and the grit paper. Mathematically the asperity stiffness is introduced by the spring stiffness k.
- F_n: The applied normal load

$$\Sigma F_z = -|f_{spring}| - |F_n| + |f_z| \ , f_z \uparrow\downarrow \ f_{spring}$$

Equation 4.5

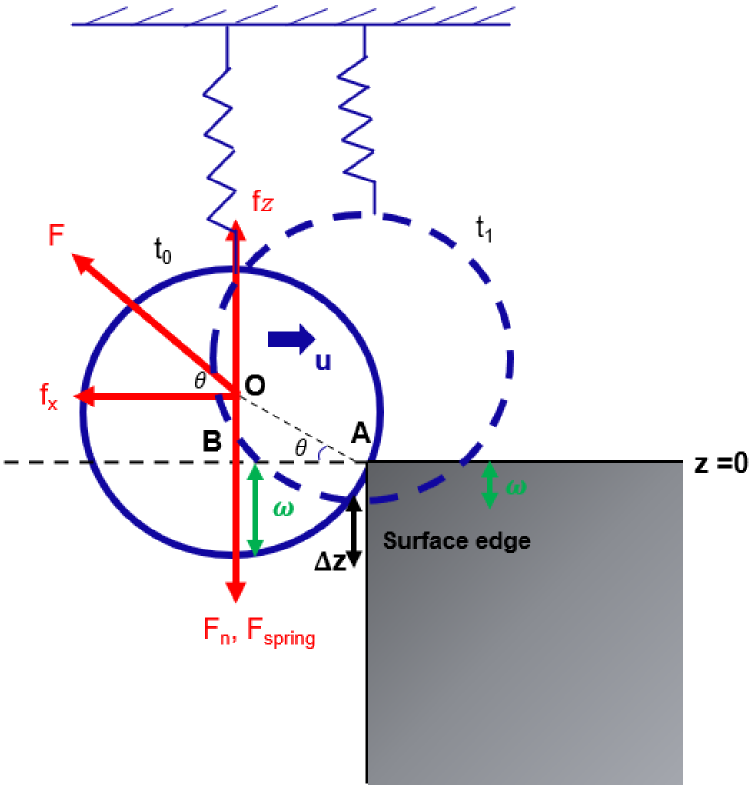

Figure 4.21: Schematic representation of a spherical asperity colliding with a surface edge at the time moment t_0. For $t_1>t_0$, the asperity has climbed the edge by resolving its contact interference ω.

By looking the change of interference between t_1 and t_0, it is seen that the change in interference equals to the change of z-displacement Δz. Therefore the following equation holds:

$$d\omega = dz$$

Equation 4.6

From the Pythagorean theorem in the triangle OAB, the side AB can be obtained:

$$R^2 = (R-\omega)^2 + AB^2 \rightarrow AB = \sqrt{\omega(2R-\omega)}$$

Equation 4.7

Angle θ is the angle between the z=0 plane of the surface and the direction of the acting force F. So, $tan\theta$ is:

$$tan\theta = \frac{R-\omega}{AB} \rightarrow tan\theta = \frac{R-\omega}{\sqrt{\omega(2R-\omega)}}$$

Equation 4.8

However, the magnitude of f_z and f_x are linked with $\tan\theta$ as following:

$$tan\theta = \frac{f_z}{f_x} \rightarrow f_z = f_x tan\theta = f_x \frac{R-\omega}{\sqrt{\omega(2R-\omega)}}$$

Equation 4.9

Substituting Equation 4.9 to Equation 4.5 yields:

$$\Sigma F_z = -|f_{spring}| - |F_n| + f_z \rightarrow \Sigma F_z = -|f_{spring}| - F_n + f_x \frac{R-\omega}{\sqrt{\omega(2R-\omega)}}$$

Equation 4.10

Using Newton's 2nd law and Hooke's law for $|f_{spring}| = kz$ we have:

$$m\ddot{z} = -kz - F_n + f_x \frac{R-\omega}{\sqrt{\omega(2R-\omega)}}$$

, which according to Equation 4.6 ($dz = d\omega$) gives:

$$m\ddot{\omega} = -k\omega - F_n + f_x \frac{R-\omega}{\sqrt{\omega(2R-\omega)}} \rightarrow m\ddot{\omega} - f_x \frac{R-\omega}{\sqrt{\omega(2R-\omega)}} + k\omega + F_n = 0$$

Equation 4.11

As boundary conditions ω is taken so that $\omega(t=0)$ takes its maximum (negative) value ω_M, while at $t \rightarrow \infty$ the asperity is sliding on the top of the surface having the minimum interference ω_m. Mathematically:

$$\omega(0) = \omega_M$$

Equation 4.12

$$\omega(\infty) = \omega_m$$

Equation 4.13

Although Equation 4.11 gives the equation of motion on z-axis of the asperity no symbolic solution can be reached with the boundary conditions of Equation 4.12-13. Therefore the assumption that contact interference is considerably less than the asperity radius was used ($R \gg \omega$). However, even with this approximation no symbolic solution could be reached with the boundary conditions of Equation 4.11-15. Therefore the variables δ and r were used to simplify the ODE:

$$Eq.7\ (R \gg \omega) \rightarrow m\ddot{\omega} + \frac{f_x\sqrt{\frac{R}{2}}}{\sqrt{\omega}} - k\omega - F_n = 0$$

Equation 4.14

$$R = \alpha(1 + \frac{r}{\alpha})$$

Equation 4.15

$$\omega = \beta(1 + \frac{\delta}{\beta})$$

Equation 4.16

, where α and β are positive constants with units of distance, so both parts of the equations are expressed in meters. Taking the 1st order Taylor approximation of Eq4.15.16 results in the linearization of Equation 4.14.

$$\frac{1}{\sqrt{\omega}} = \beta^{-\frac{1}{2}}\left(1 + \left(\frac{\delta}{\beta}\right)\right)^{-\frac{1}{2}} \xrightarrow{1^{st} order\ Taylor\ approx.} \frac{1}{\sqrt{\omega}} = \beta^{-\frac{1}{2}}\left(1 - \frac{1}{2}\frac{\delta}{\beta}\right)$$

Equation 4.17

$$\sqrt{R} = \sqrt{\alpha}\sqrt{1 + \frac{r}{2\alpha}}$$

Equation 4.18

$$\ddot{\omega} = \ddot{\delta}$$

Equation 4.19

Substituting Equation 4.16-18 to Equation 4.14 yields:

$$m\ddot{\delta} + k\beta + k\delta - f_x\sqrt{\frac{\alpha}{2\beta}}\left(1 + \frac{1}{2\alpha}r\right) + \frac{f_x}{2\beta}\sqrt{\frac{\alpha}{2\beta}}\left(1 + \frac{1}{2\alpha}r\right)\delta + F_n \rightarrow$$

$$m\ddot{\delta} + k\delta + \frac{f_x}{2\beta}\sqrt{\frac{\alpha}{2\beta}}\left(1 + \frac{1}{2\alpha}r\right)\delta + F_n + k\beta - -f_x\sqrt{\frac{\alpha}{2\beta}}\left(1 + \frac{1}{2\alpha}r\right) = 0$$

$$\ddot{\delta} + \frac{k + \frac{f_x}{2\beta}\sqrt{\frac{\alpha}{2\beta}}(1 + \frac{r}{2\alpha})}{m}\delta + \frac{F_n + k\beta - f_x\sqrt{\frac{\alpha}{2\beta}}(1 + \frac{r}{2\alpha})}{m} = 0$$

$$\boxed{\ddot{\boldsymbol{\delta}} + \boldsymbol{\xi_1\delta} + \boldsymbol{\xi_2} = \mathbf{0}}$$

Equation 4.20

$$\xi_1 = \xi_1(k, R, m, F_n, \mu) = \frac{k + \frac{\mu F_n}{2\beta}\sqrt{\frac{\alpha}{2\beta}}\left(1 + \frac{r}{2\alpha}\right)}{m} = \frac{k + \frac{\mu F_n}{2\beta}\sqrt{\frac{\alpha}{2\beta}}\left(\frac{2R}{2\alpha}\right)}{m} \quad [\frac{1}{s^2}]$$

Equation 4.21

$$\xi_2 = \xi_2(k, R, m, F_n, \mu) = \frac{F_n + k\beta - \mu F_n \sqrt{\frac{\alpha}{2\beta}} \left(\frac{2R}{2\alpha}\right)}{m} \quad \left[\frac{N}{kg}\right] = \left[\frac{m}{s^2}\right]$$

Equation 4.22

$$\xi = \frac{\xi_2}{\xi_1} = \frac{1 + \frac{k\beta}{F_n} - \mu \sqrt{\frac{\alpha}{2\beta} \frac{2R}{2\alpha}}}{\frac{k}{F_n} + \frac{\mu \sqrt{\frac{\alpha}{2\beta} \frac{2R}{2\alpha}}}{2\beta}} \quad [m]$$

Equation 4.23

ODE of Equation 4.20 is solved analytically and the solution is given in Equation 4.24:

$$\delta = (\omega_M + \xi - \beta)\, e^{-\sqrt{|\xi_1|}\, t} + \beta - \xi \xrightarrow{Eq.4.16} \omega = (\omega_M + \xi - \beta)\, e^{-\sqrt{|\xi_1|}\, t} + 2\beta - \xi =$$
$$\xrightarrow{\beta = |\omega_M|} \boxed{\omega = \xi e^{-\sqrt{|\xi_1|}\, t} + 2|\omega_M| - \xi}$$

Equation 4.24

, where $\omega_M < 0$ is the initial asperity interference. Taking the second time derivative of Equation 4.24 and equating with zero, gives the condition of $\dot{\omega}$ minimization:

$$\frac{d\omega}{dt} = \xi\left(-\sqrt{\xi_1}\right) e^{-\sqrt{|\xi_1|}\, t} \rightarrow \frac{d^2\omega}{dt^2} = \xi * \xi_1\, e^{-\sqrt{|\xi_1|}\, t} = 0 \rightarrow \xi = 0\ (1) or\ \xi_1 \rightarrow 0\ (2)$$

Equation 4.25

All quantities in ξ_1 are positive, therefore (2) is rejected. Solving (1) yields Equation 4.26, which is the condition which should be met in order for minimum edge wear to occur. Equation 4.26 is the final result of the model and the quantity I is a function of Coefficient of Friction (μ) asperity, asperity initial interference (ω_M), asperity radius (R), stiffness (k) and the applied normal load (F_n). The parameter R_{max} is a positive constant with units of distance and it represents the maximum radius of curvature of a distribution of asperities. Equivalently, it represents the maximum value of x-axis of Figure 4.15b.

Contour plots for I under different stiffness and CoF values are illustrated in Figure 4.22. The x-axis of Figure 4.22 is the "normalized" radius of curvature, defined as $R/\sqrt{R_{max}}$ and the y-axis is the initial asperity interference (ω_M) over the coating thickness ($\omega_{\max}$). The "normalized" radius of curvature was chosen as $R/\sqrt{R_{max}}$ instead of R/R_{max} due to the presence of the former into Equation 4.26.

$$-\frac{1+\frac{k\beta}{F_n}-\mu\sqrt{\frac{\alpha}{2\beta}\frac{2R}{2\alpha}}}{\frac{k}{F_n}+\frac{\mu\sqrt{\frac{\alpha}{2\beta}\frac{2R}{2\alpha}}}{2\beta}}=0\rightarrow 1=\mu\sqrt{\frac{\alpha}{2|\omega_M|}\frac{2R}{2\alpha}}-\frac{k|\omega_M|}{F_n}\xrightarrow{\alpha=R_{max}}\mu\frac{1}{\sqrt{|2\omega_M|}}\frac{R}{\sqrt{R_{max}}}-\frac{k|\omega_M|}{F_n}=1\rightarrow$$

$$I=\boxed{\mu\frac{1}{\sqrt{2|\omega_M|}}\frac{R}{\sqrt{R_{max}}}-\frac{k|\omega_M|}{F_n}=\ 1}$$

Equation 4.26

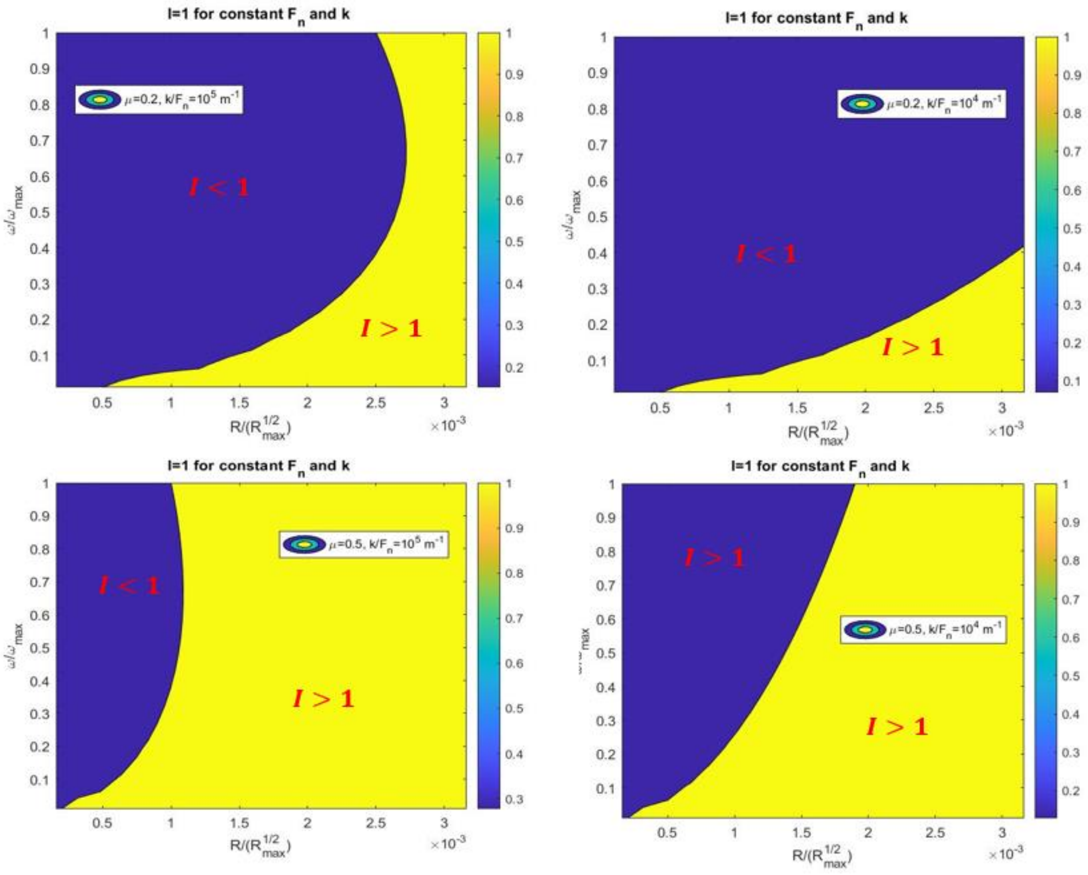

Figure 4.22: Contour plots of I versus the absolute value of initial interference over coating thickness and normalized asperity radius. $I<1$ holds in the blue area and $I>0$ holds in the yellow area. $I=1$ is the condition for minimization of the rate of change asperity interference and thus edge wear during an asperity colliding with an edge. A: I for μ=0.2, $\frac{k}{F_n}=10^5$, B: I for μ=0.2, $\frac{k}{F_n}=10^4$ (more compliant asperity), C: I for μ=0.5, $\frac{k}{F_n}=10^5$, D: I for μ=0.5, $\frac{k}{F_n}=10^4$.

Minimizing wear during collision can also be derived by minimizing the force during impact. Using Newtons 2nd law ($f=\frac{dp}{dt}=m\,d^2\omega/dt^2$) and substituting m as proportional to R^3 (based on the fact that the volume of a sphere is proportional to R^3) and $d^2\omega/dt^2$ from Equation 4.25, the impact force f is found to be proportional to ξ_2 which is equal to $(-I+1)/m$. Therefore, minimization of f is reached when Equation 4.26 is reached, indicating the validity of the proposed model.

Key messages from Figure 4.22 are:

- CoF during the “climbing” of an asperity over an edge plays a crucial role on the locus of points for which $I = 1$. This is shown by comparing Figure 4.22a-c and Figure 4.22b-d. From Figure 4.20 it was shown that grit paper’s CoF increased as it was “climbing” the wafer edge. An analogous behavior for a single asperity is expected.
- For $\frac{k}{F_n} = 10^4, \mu = 0.5$, (Figure 4.22d) sharp asperities ($\frac{R}{\sqrt{R_{max}}} \sim 1.6\ 10^{-3}$) with maximum normalized initial interference less than 30% of the coating thickness will result in lower edge wear. For blunter asperities, ω_M increases, in order to keep $I = 1$. However, as initial interference increases, it will reach the depth of coating/substrate interface causing coating delamination.
- Increasing asperity stiffness (the stiffness of the adhesive between the grit paper and the steel holder) shifts the locus of $I = 1$ points towards sharper asperities (comparing Figure 4.22c-d). Therefore, low edge wear is accomplished by the use of stiffer adhesive and blunter asperities.
- Asperity radius should not exceed $\frac{R}{\sqrt{R_{max}}} \sim 1.6\ 10^{-3}$. For higher radii, initial interference which gives $I = 1$, is close to coating thickness, therefore increasing the risk of coating delamination. So, initial interference is suggested to be kept less than 30% of coating thickness.

4.3.6 Designing strategy for enhanced wear performance

Therefore, designing routes for reducing wear under high ramped loading for multi-asperity diamond-DLC contacts are the following:

- Diamond asperity height distribution should be continuous in order for successive asperities to carry any load increments. In other words, height distribution should look like the one illustrated in Figure 4.23a, where there are “short”, “tall” and intermediate asperities rather than this of Figure 4.23b, where there are only “short” and “tall” asperities. In the former case, the taller ones will first carry the applied load and as the normal load increases the shorter asperities will start carrying the load without letting the taller ones penetrate deep enough to promote subsurface yielding and adhesive failure. The effect of asperity height distribution on wear behavior has been first studied by the work of Greenwood and Williamson [66] in the mid-60s, but also later with more novel numerical calculations [69] [70]. In the former, the contact deformation of rough surfaces is studied when two surfaces are elastically and plastically loading. The latter two, computationally investigate elastoplastic loading between two rough surfaces.
- DLC/SiC adhesion strength needs to be as high as possible. However, optimizing DLC/substrate adhesion is rather complex [26] as explained in section 2.4. An equivalent state is reached if subsurface (shear) stresses are minimized. This can be achieved by reducing contact pressure per asperity. This is met by the first step described in this list, since the load per asperity does not change considerably because of the successive asperities that are brought into contact and start carrying the applied normal load (Figure 4.23a). In addition, if softer DLC interlayer thickness increases, the compliance of harder-top layer would increase, reducing contact stresses. However, attention should be paid on the fact that increasing contact area may result in friction increase and potentially higher wear. In our tests, CoF during single-asperity scratching tests are very low (<0.1). Therefore, an increase in friction is not expected to cause severe wear. If however, CoF during

sample-level testing is high, then increasing the soft-interlayer thickness may degrade system's abrasive wear performance.

- When asperity collisions with edges take place, the rate of change of interference should not increase suddenly, because of increased edge wear and possible coating delamination. An analytical model was developed which dictates that minimization of edge wear is accomplished when Equation 4.26 is satisfied or, in other words, when asperity's initial interference just before collision and asperity radius are decreased. Increasing asperity radius-without turning other parameters involved in Equation 4.26 will aggravate edge wear by probably causing DLC spallation. For the current work it is suggested that asperity initial interference should not exceed 30% of the coating thickness and the ratio of $\frac{R}{\sqrt{R_{max}}}$ should be kept around 0.0016.

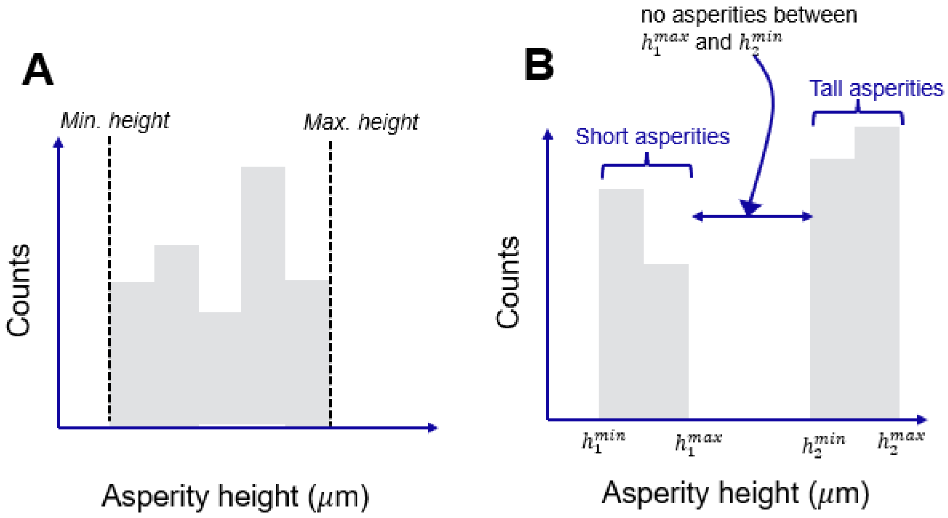

Figure 4.23: (A) A continues asperity height distribution between a minimum height value and a maximum height value. (B) Non continuous asperity height distribution. Two "groups" of asperities are observed named "short" asperities and "tall" asperities. The former are having heights from h_1^{min} to h_1^{max} and the latter from h_2^{min} to h_2^{max}. No asperities are having a height inside the h_1^{max}-h_2^{min} range. This results in taller asperities carrying the applied load and penetrating deeper into the material while the shorter ones are still not in contact thus they don't carry any part of the applied load.

5 Conclusions and recommendations

5.1 Conclusions

The answers to the research questions formulated in section 2.5 are illustrated in this chapter:

1) What is the DLC abrasive wear behavior when scratched by diamond particle(s)?

DLC abrasive wear behavior when scratched by diamond particles is predominantly plowing with wear debris inside and outside of wear scar. Under higher loading (≥35mN), debris density increases and upon further loading (100mN) DLC fails by spallation (adhesive failure between DLC/SiC substrate).

2) Is DLC wear behavior strain rate dependent?

DLC deformation is not strain rate dependent. This is supported by nanoindentation tests under different strain rates. DLC/SiC system wear performance is strain rate sensitive for high normal loads ($F_n \geq 100$mN). In other words, when normal load at the single-asperity scale is high enough so as subsurface stresses at DLC/SiC interface are comparable to the interfacial adhesion strength, the wear behavior is influenced by DLC/SiC interface and SiC mechanical properties, where the former seems to have a strain rate sensitivity. Therefore, the overall coating (DLC)-substrate (SiC) system wear behavior is strain rate dependent.

3) How the substrate-DLC interface affects the DLC tribological behavior?

DLC/SiC interface plays critical role under high loading. Therefore, high interfacial strength results in better abrasive wear performance. Also, strain rate seems to influence the adhesion strength by mechanisms still unknown.

4) What material lift-up features are created during single and multi-asperity scratching?

During single-asperity scratching tests highest material lift-up (in sometimes exceeding 200nm) are produced in the onset of spallation. During plowing loose wear debris are produced in both cases.

5) Does DLC interlayer thickness affect coating's wear behavior?

In this work interlayer thickness did not alter abrasive wear performance. Under low loading it is not expected to influence the wear behavior due subsurface stresses being carried by DLC bulk. For higher loading applications increasing interlayer thickness will result in higher compliance of the hard top-layer, increasing contact area and thus decreasing contact pressure and therefore the magnitude of subsurface stresses. Caution should be paid on the effect of true contact area increase when there is strong adhesion between the contacted surfaces because of increase in coefficient of friction (CoF).

6) What is the wear at the edge of a surface when an asperity collides with it?

As shown in section 4.2.1 and 4.3.5, the wear at the edge of the DLC surface was maximum (DLC spallated), when the rate of change of interference was maximum. As $\dot{\omega}$ decreased, DLC plowing at the edge occurred.

7) How the interference of an asperity colliding with a surface edge change during the collision?

When an asperity of the grit paper of section 4.2 collides with the edge of a surface its initial interference (ω_M) takes its maximum value. After the impact, the interference decreases exponentially as shown by

Equation 4.24. The condition for minimized edge wear is given in Equation 4.26, where in order for this condition to be met fine-tuning of the following parameters should be performed:

- Asperity initial interference (ω_M) .
- Asperity radius (R).
- Coefficient of friction (CoF).
- Adhesive material's stiffness. The adhesive glues the steel holder with the diamond grit paper.

The guideline derived is that "normalized" asperity radius($R/\sqrt{R_{max}}$) and initial interference should be decreased. The former should not exceed 0.0016 and the latter should be lower than 30% of coating thickness.

8) What design guidelines should be followed to optimize DLC wear behavior?

Since wear is system property, improving the tribosystem components will result in lowering system's (DLC-diamond) abrasive wear. The following qualitative guidelines are suggested:

- It is beneficial when the scratching surface comprises asperities with continuous height distribution. This results in a wider macroscopic normal load range that gives similar wear behavior in single-asperity scale since successive asperities will start carrying the applied load.
- In applications where asperities collide with a surface edge it is instructed that asperities rate of interference should be as low as possible during the impact. In section 4.3.5 it was shown that $\dot{\omega}$ depends on asperity stiffness, asperity radius, asperity mass and normal load. More precisely, Equation 4.26 illustrates the condition for edge wear minimization and Figure 4.22 shows the contour plots under different asperity radius and initial interference. The suggested guideline to minimize wear is that initial asperity interference and asperity radius should be lowered.

Key messages of this thesis are:

- DLC bulk deformation is not strain rate dependent. Results supporting this statement are illustrated in section 4.1.1 Figure 4.1.
- DLC/SiC wear behavior is strain rate sensitive in higher loads. It is suggested that DLC/SiC interface shows strain rate sensitivity. Results supporting this statement are illustrated in Figure 4.11 of section 4.1.2. Discussion supporting this statement can be found in 4.3.1.
- For DLC applications with normal load per asperity higher than 100mN and with strain rates that are considerably higher than those reached in single-asperity tests (e.g. scratching), single asperity tests are not representative of the applications, because of the considerable strain rate influence on DLC abrasive wear behavior. Supporting evidence can be found in 4.3.1.
- There is a macroscopic normal load range that produces similar single-asperity wear behavior. It is suggested that this range depends on the asperity height distribution. Results showing this can be found in section 4.2 and relative discussion was held in section 4.3.4.
- For the case when an asperity collides with DLC surface edge, minimization of edge wear is accomplished when the asperity initial interference and radius are reduced while keeping the asperity stiffness and applied normal load constant. The higher the rate of change of asperity interference the higher the edge wear. Equation 4.26 gives the condition for minimum edge wear, which is an expression involving CoF, asperity initial interference (just before it collides with the

surface), asperity radius, asperity stiffness and applied normal load. Increasing asperity radius is not recommended for optimized edge wear. From this work it is suggested that in order for minimum edge wear to occur, normalized asperity radius ($R/\sqrt{R_{max}}$) should be lower than 0.0016 and initial interference should be less than 30% of the coating thickness.

5.2 Recommendations

1. Investigation of strain rate influence on DLC/SiC adhesion strength. Deconvoluting the interplay between nanomechanical and physicochemical processes taking place in coating-substrate interface.
2. From the literature it is known that etching time enhances DLC/substrate adhesion by removing surface oxides prior DLC deposition. Also, depositing a thin film (adhesion film) between DLC and the substrate has been proven advantageous. Examples of such films are Si, Ti/TiN and Cr [71] [72]. Scratching tests with and without adhesion films under 100mN and 5μm spherical tip are suggested, in order to investigate the quantitative differences in scratch characteristics and DLC spallation.
3. Perform single-asperity scratching tests at 100mN 100$\mu m/s$ and 500 $\mu m/s$ in order to investigate the DLC non-linear strain rate wear dependency.
4. Perform single-asperity scratching tests at given loads with tips of different radius and under ramped and constant load. This is proposed in order to deduce the reason why wear debris were produced inside the wear scar in our case while in others work no debris inside wear scars were formed [60] [65].
    a. Proposed tips radius are 0.5,1,5 μm .
    b. Ramped and constant load scratching is proposed. Ramped load is proposed to be from 0 to 100mN and constant load to be 100mN.
    c. FIB cross sections of the produced scratches should be obtained.

    Coupled with the 1st recommendation a better understanding of DLC abrasive wear and the effect of DLC/coating interface can be obtained.

5. Perform numerical analysis to explain why DLC spallations occur successively (with around 5μm distance from the previous spallation) after the first spallation occurs.
6. Based on experimental results of A.1.3.1 and Figure 4.7 for diamond tip wear , a wear model for a 5μm diamond tip sliding against DLC can be proposed. More specifically, the data points of Figure 4.7 can be fitted and based on this fitting, the tip wear during the single-asperity scratching tests can be estimated.

A Appendix

A.1 Single-asperity scratching tests

A.1.1 Single-asperity scratching tip overview

Measurement number	Normal load (mN)	Strain rate (µm/s)	# Tip
1	10	0.5	1
2	10	0.5	1
3	10	0.5	1
4	10	0.5	1
5	10	0.5	1
6	10	0.5	1
7	10	0.5	1
8	10	0.5	1
9	10	0.5	1
10	10	10	1
11	10	10	1
12	10	10	1
13	10	10	1
14	10	10	1
15	10	10	1
16	10	10	1
17	10	10	1
18	10	10	1
19	10	1000	1
20	10	1000	1
21	10	1000	1
22	10	1000	1
23	10	1000	1
24	10	1000	1
25	10	1000	1
26	10	1000	1
27	10	1000	1
28	35	0.5	1
29	35	0.5	1
30	35	0.5	1
31	35	0.5	1
32	35	0.5	1
33	35	0.5	1
34	35	0.5	1
35	35	0.5	1
36	35	0.5	1
37	35	10	1
38	35	10	1
39	35	10	1
40	35	10	1
41	35	10	1
42	35	10	2
43	35	10	2
44	35	10	2
45	35	10	2
46	35	1000	2
47	35	1000	2
48	35	1000	2
49	35	1000	2
50	35	1000	2
51	35	1000	2
52	35	1000	2

53	35	1000	2
54	35	1000	2
55	100	0.5	2
56	100	0.5	2
57	100	0.5	2
58	100	0.5	2
59	100	0.5	2
60	100	0.5	2
61	100	0.5	2
62	100	0.5	2
63	100	0.5	2
64	100	10	2
65	100	10	2
66	100	10	2
67	100	10	2
68	100	10	2
69	100	10	3
70	100	10	3
71	100	10	3
72	100	10	3
73	100	1000	3
74	100	1000	3
75	100	1000	3
76	100	1000	3
77	100	1000	3
78	100	1000	3
79	100	1000	3
80	100	1000	3
81	100	1000	3

A.1.2 Single-asperity Confocal Optical Microscopy

Conditions	Set number
10mN 0.5µm/s	1
10mN 10µm/s	2
10mN 1000µm/s	3
35mN 0.5µm/s	4
35mN 10µm/s	5
35mN 1000µm/s	6
100mN 0.5µm/s	7
100mN 10µm/s	8
100mN 1000µm/s	9

COM images of Set 3 and Set 6 are not included because normal load was not controlled from the machine test setup. Analysis of Set 1-Set 5 was performed with the SensoView software from Sensofar and analysis of Set 6-Set 9 was done in Gwyddion.

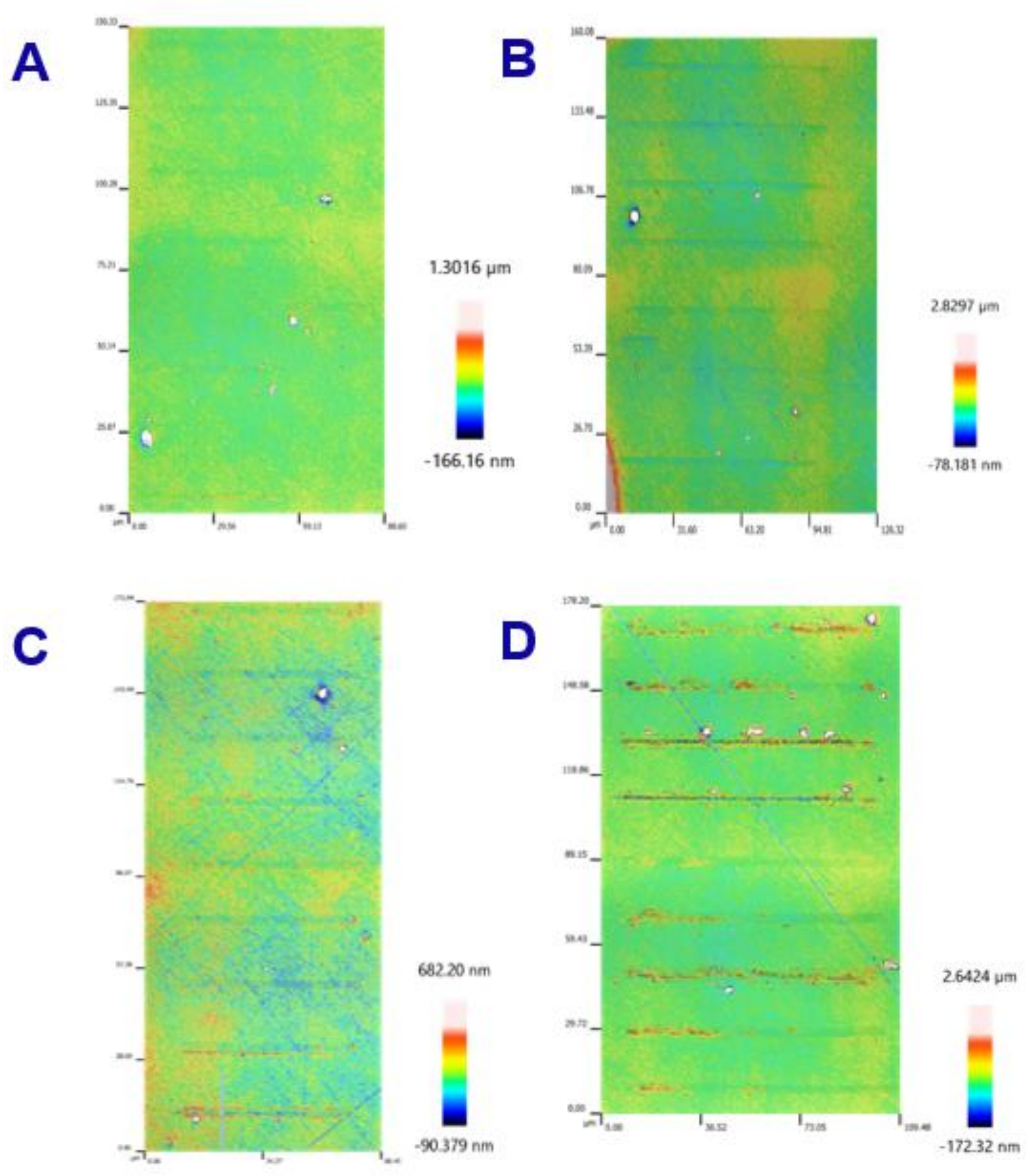

Figure A.1: A: Set 1. Scratches are barely visible due to the low applied normal load, B: Set 2: Scratches are more visible than those of Set 1, C: Set 4, D:Set 5: Wear scars full of debris, indicating perhaps worn tip.

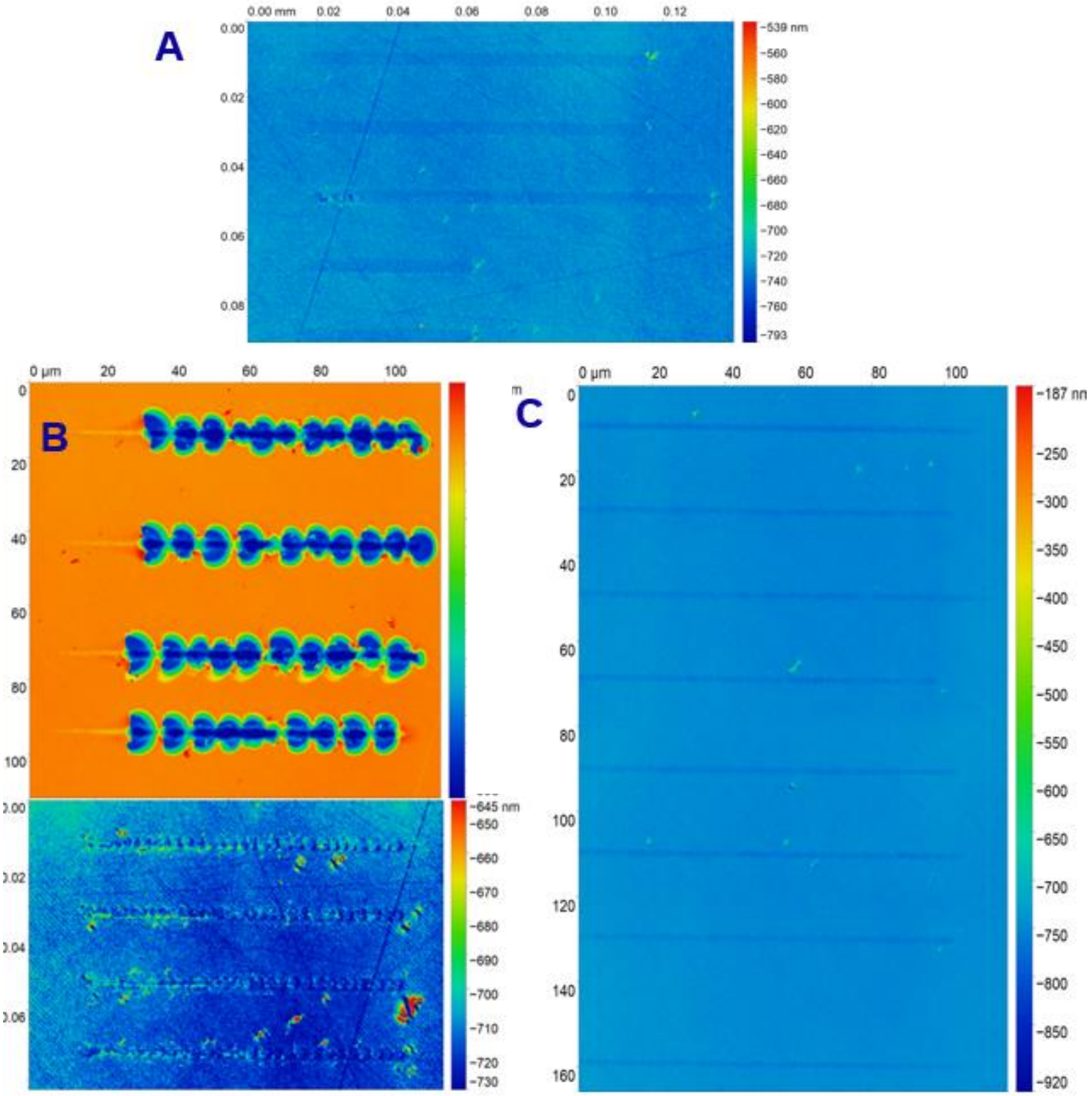

Figure A.2: A:Set7. 1-5 scratches, B: Set 8. 6 first scratches (bottom image) are full of debris (here scratches 2-5 are captured). After tip replacement scratches dramatically change indicating the effect of worn tip. Scale bars are adjusted to enhance contrast, C: Set 9.

A.1.3 SEM/EDS images of tips and scratches in single-asperity scratching tests

A.1.3.1 Diamond tips

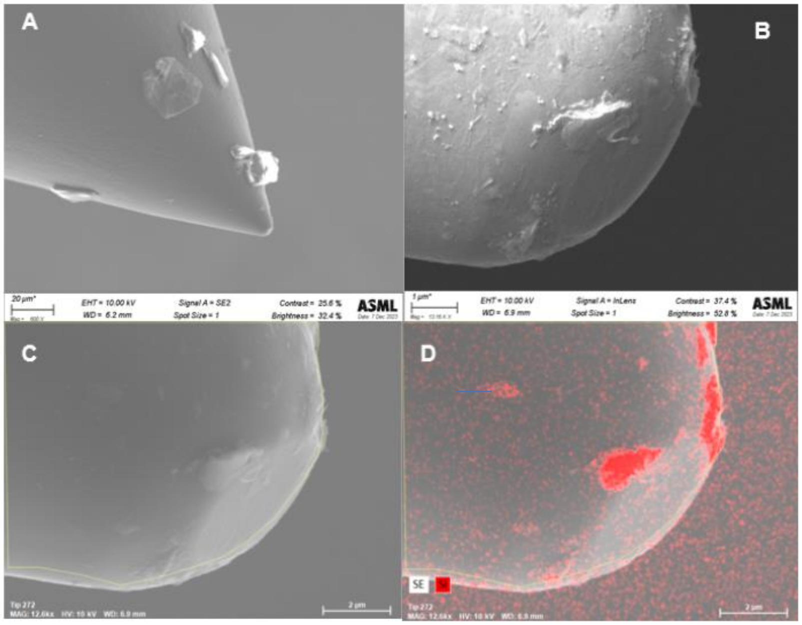

Figure A.3: Tip 1: (A) Low magnification SEM image of tip 1. (B) Enlardged image of A at the tip edge, C-D: SEM/EDS image showing adhered Si particles at the edge of the tip.

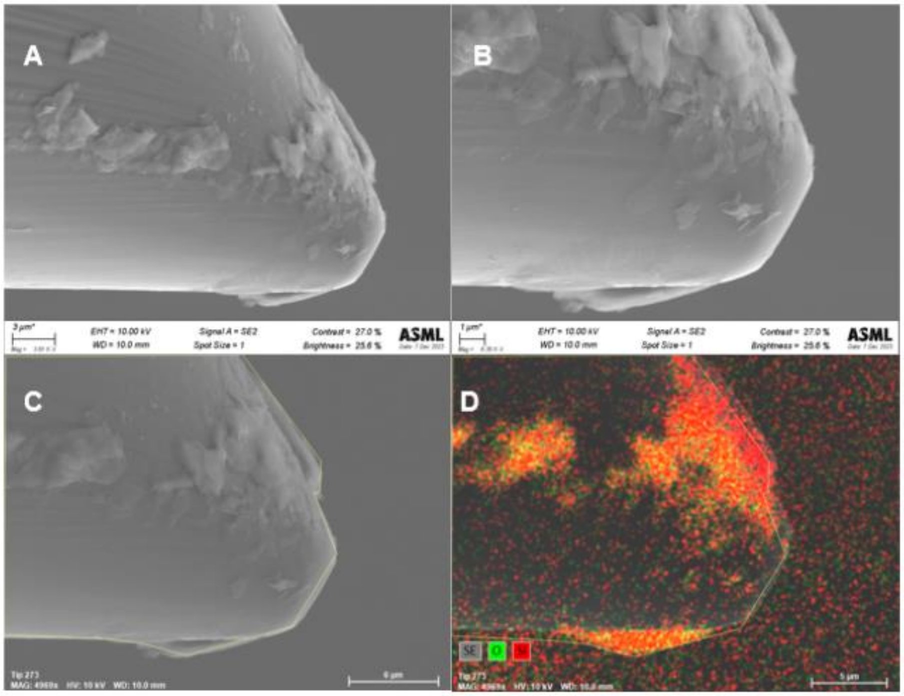

Figure A.4: Tip 2: (A) Low magnification SEM image of tip 2. (B) Enlarged image of A at the tip edge, C-D: SEM/EDS image showing adhered Si particles at the edge of the tip. Images show that tip profile is almost flat meaning that significant tip wear took place.

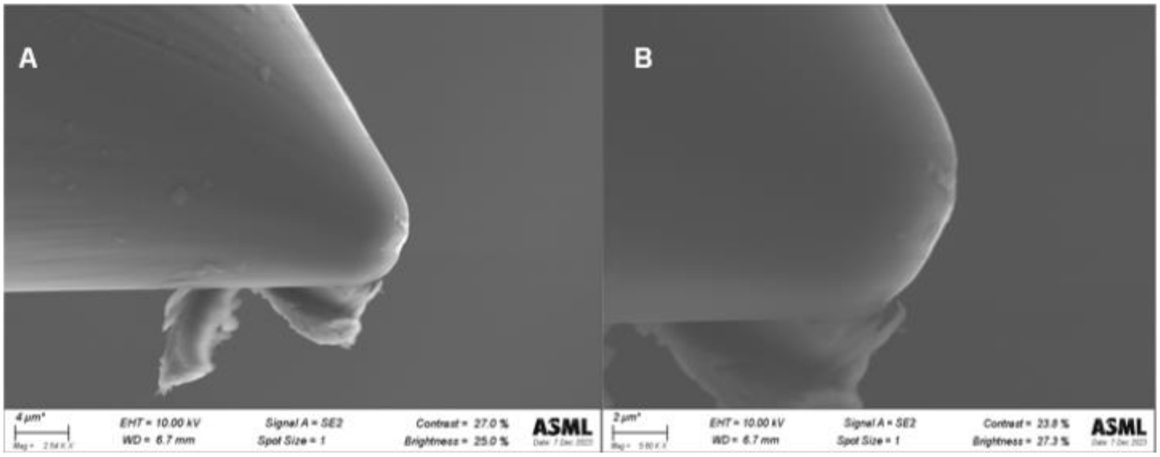

Figure A.5: Tip 3: (A) Low magnification SEM image of tip 3 showing an adhered particle (B) Enlarged image of A at the tip edge. Due to charge accumulation, acquisition of EDS images was not possible, which makes the chemical identification of the adhered particle impossible. Judging by the particle morphology it may be delaminated DLC coating.

A.1.3.2 Scratches on DLC surface

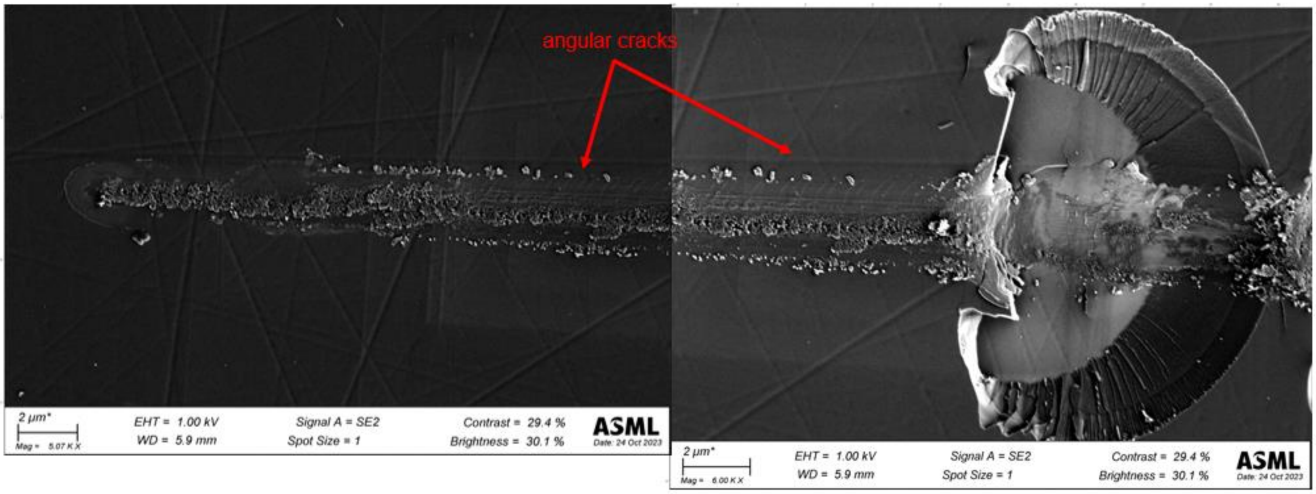

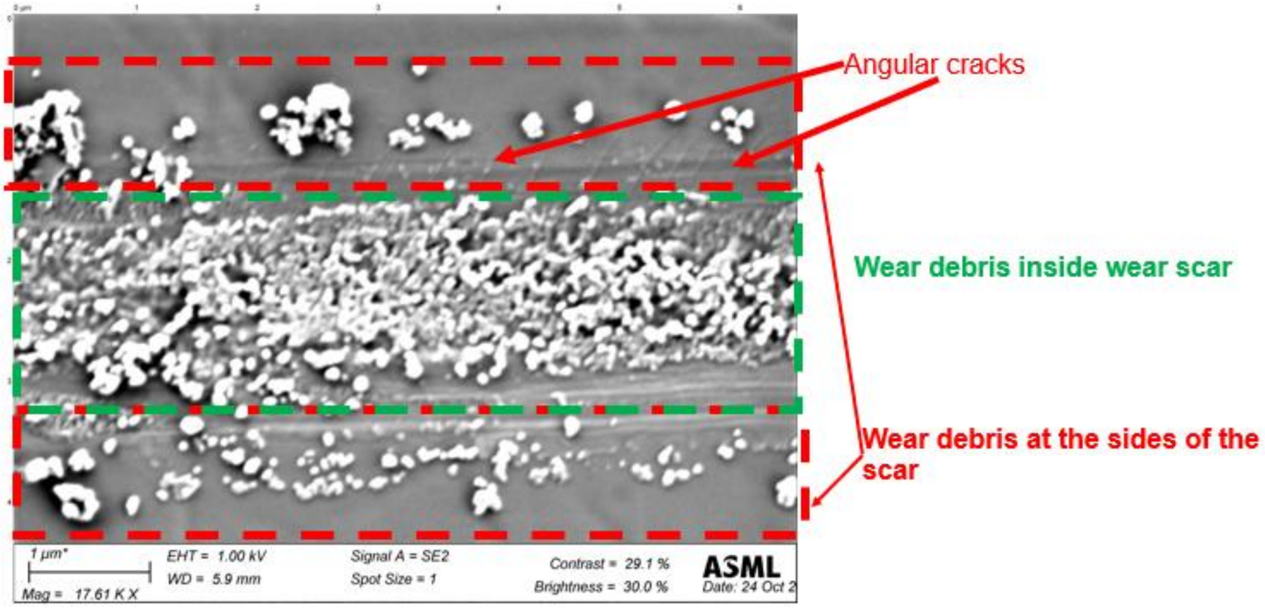

Figure A.6: SEM image showing debris inside the wear scar, at the edge of the wear track and angular cracks on the top side of the scar.

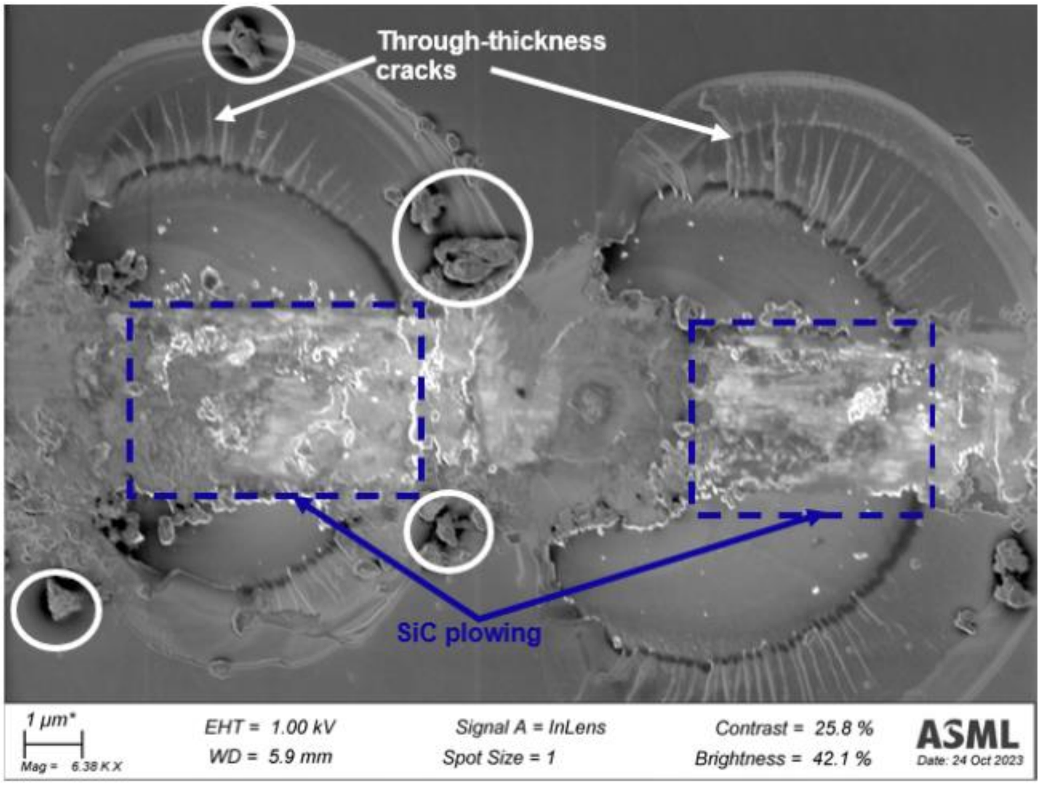

Figure A.7: SEM image of spallations. SiC plowing is observed. Through-thickness cracks are observed in the edges of spallations. Large particles are also visible and are enclosed by the white circles.

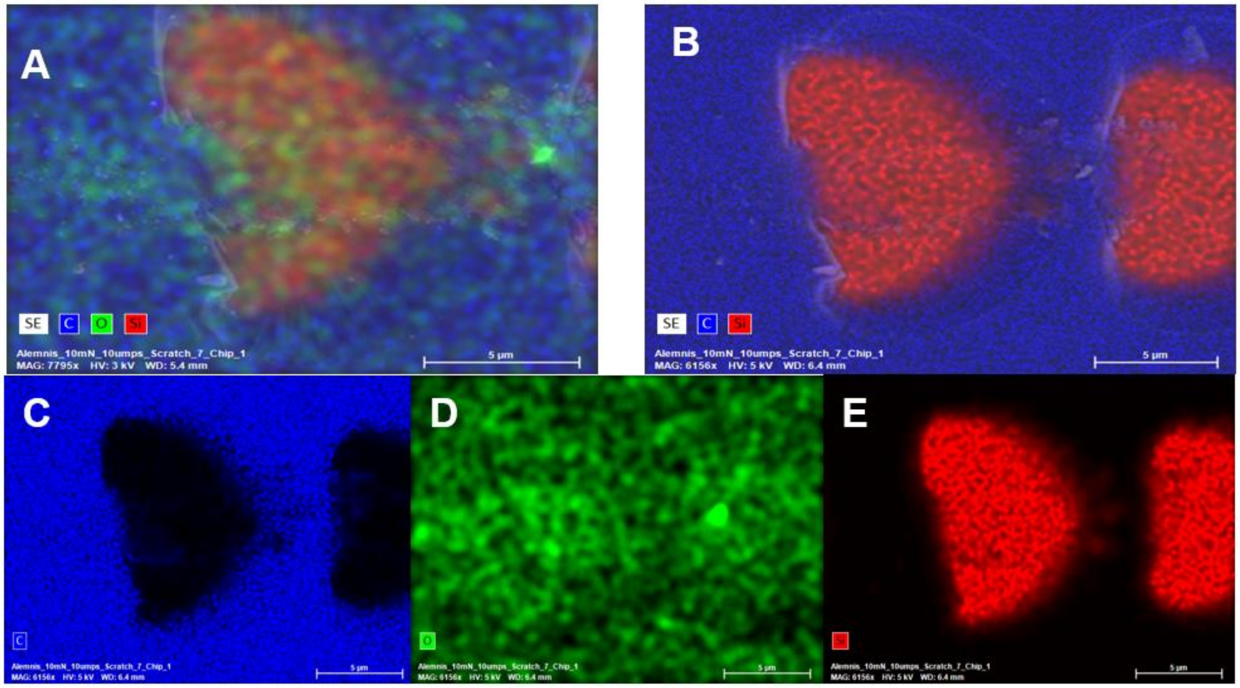

Figure A.8: SEM/EDS image of DLC spallations. DLC is completely removed inside spallations (red shows carbon). There is an organic particle at the onset of the second spallation.

A.1.4 AFM images

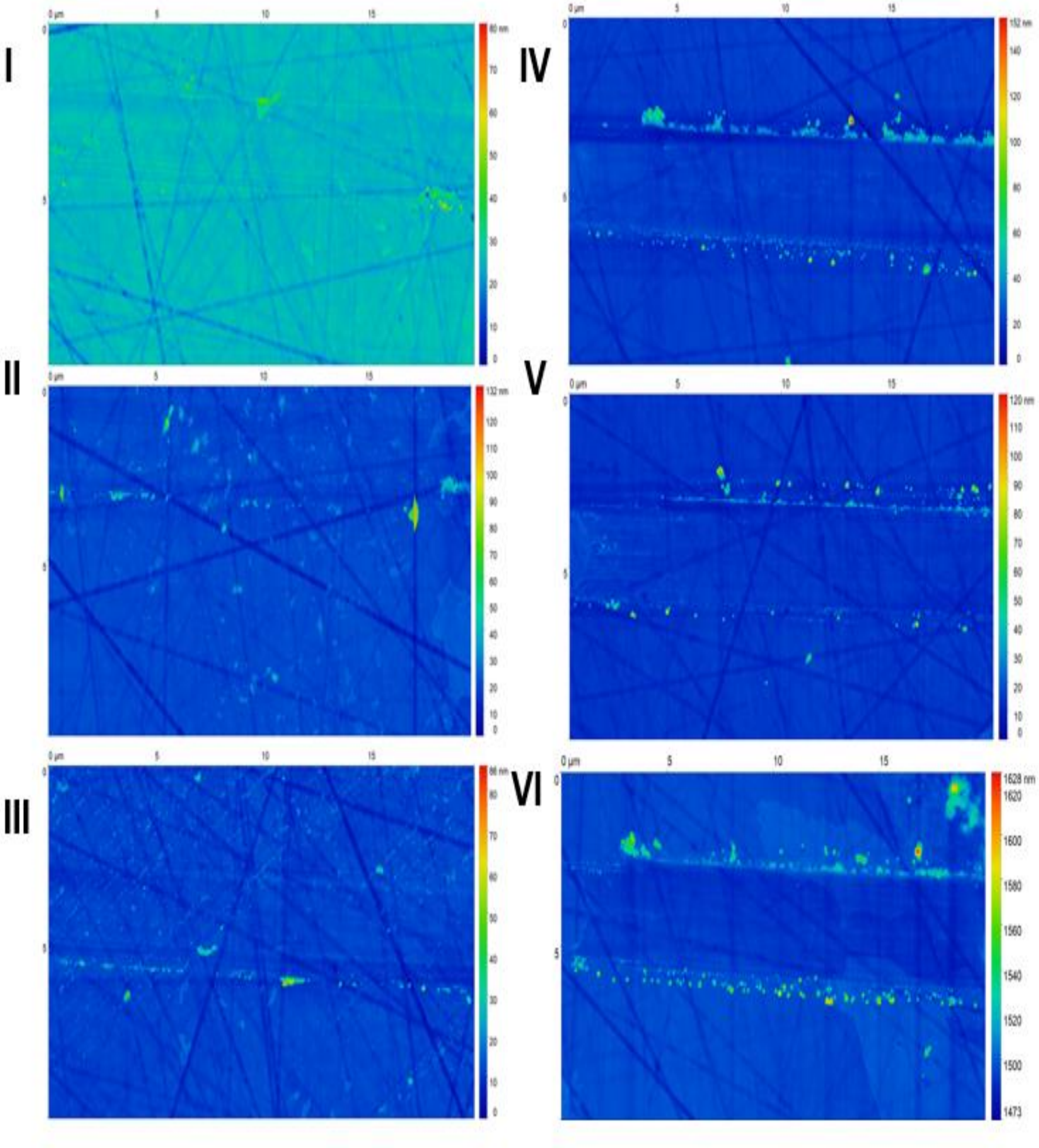

Figure A.9: I-III: Set 1 : 10mN, 0.5 μm/s.IV-V: :Set 2, 10mN, 10μm/s.VI: Set 4, 35mN, 10 μm/s.

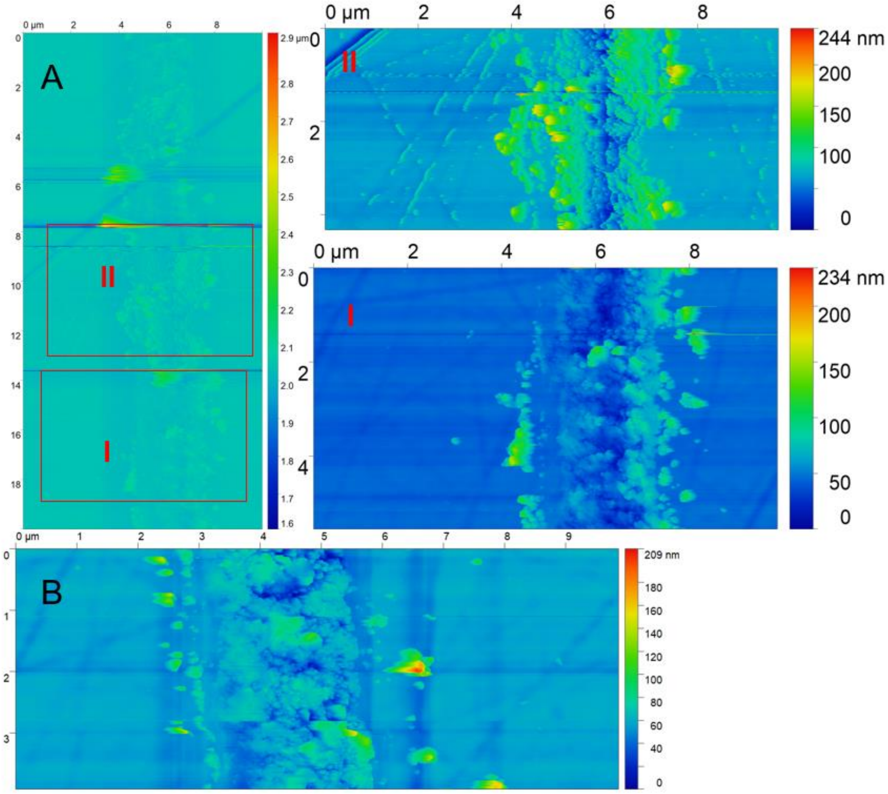

Figure A.10: Set 5: 35mN 10 um/s, with tip just before replacement. Groove is contaminated with debris.

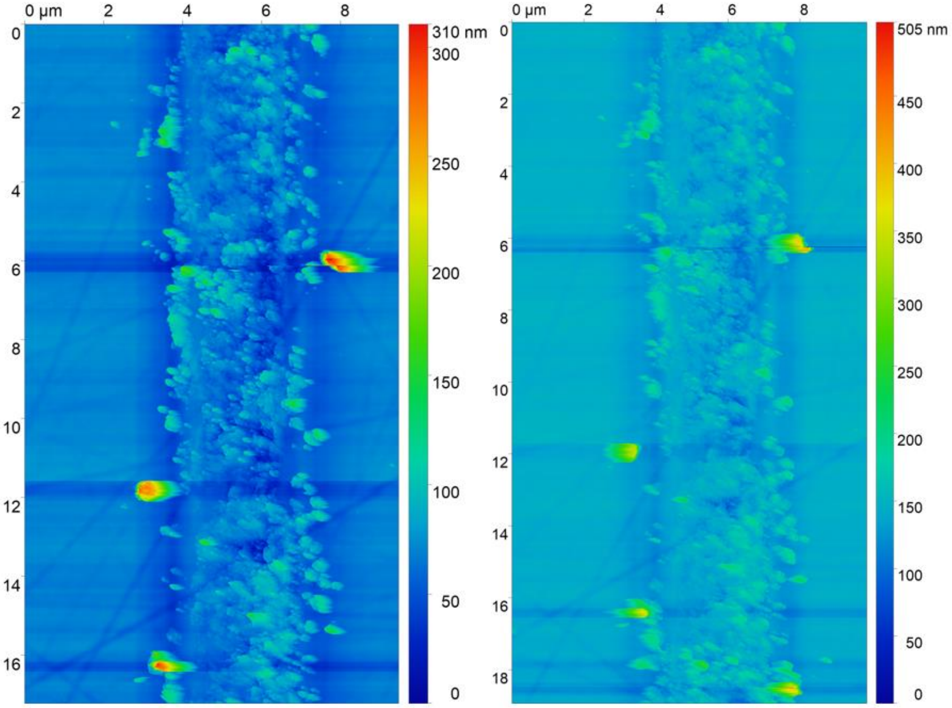

Figure A.11: Set 5 scratches with fresh tip. Forward and backward scanning.

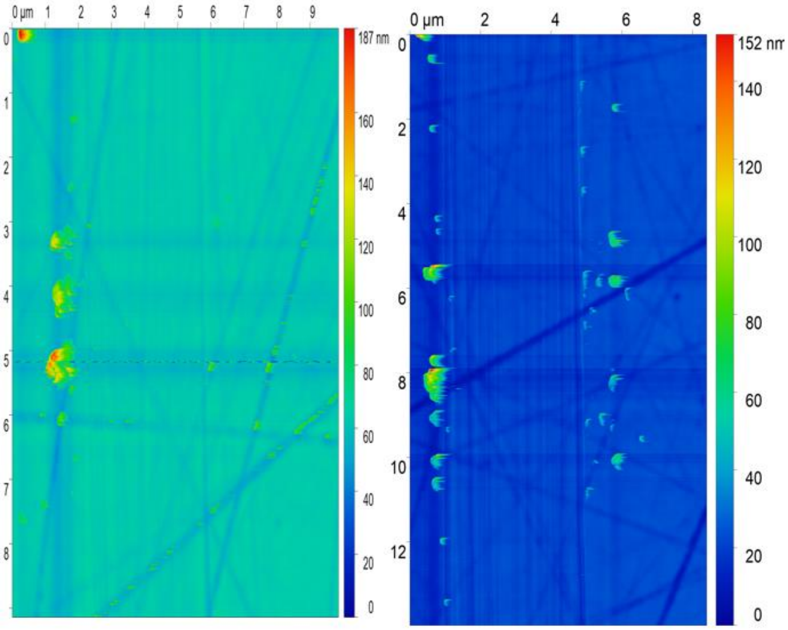

Figure A.12: Set 7, 100mN, 0.5 μm/s.

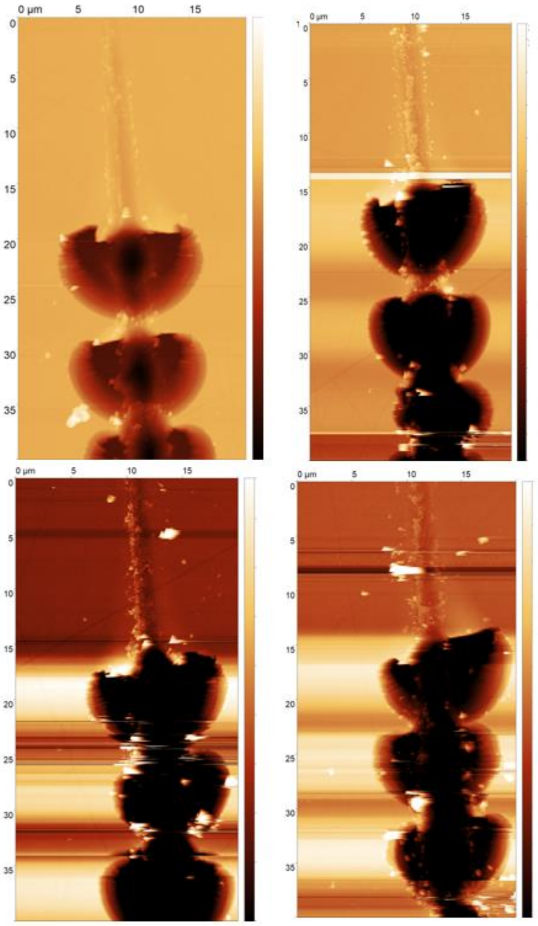

Figure A.13: Set 8, 100mN 10 μm/s. DLC plowing and spallation.

A.2 Multi-asperity tests

A.2.1 Optical micrograph of scratches

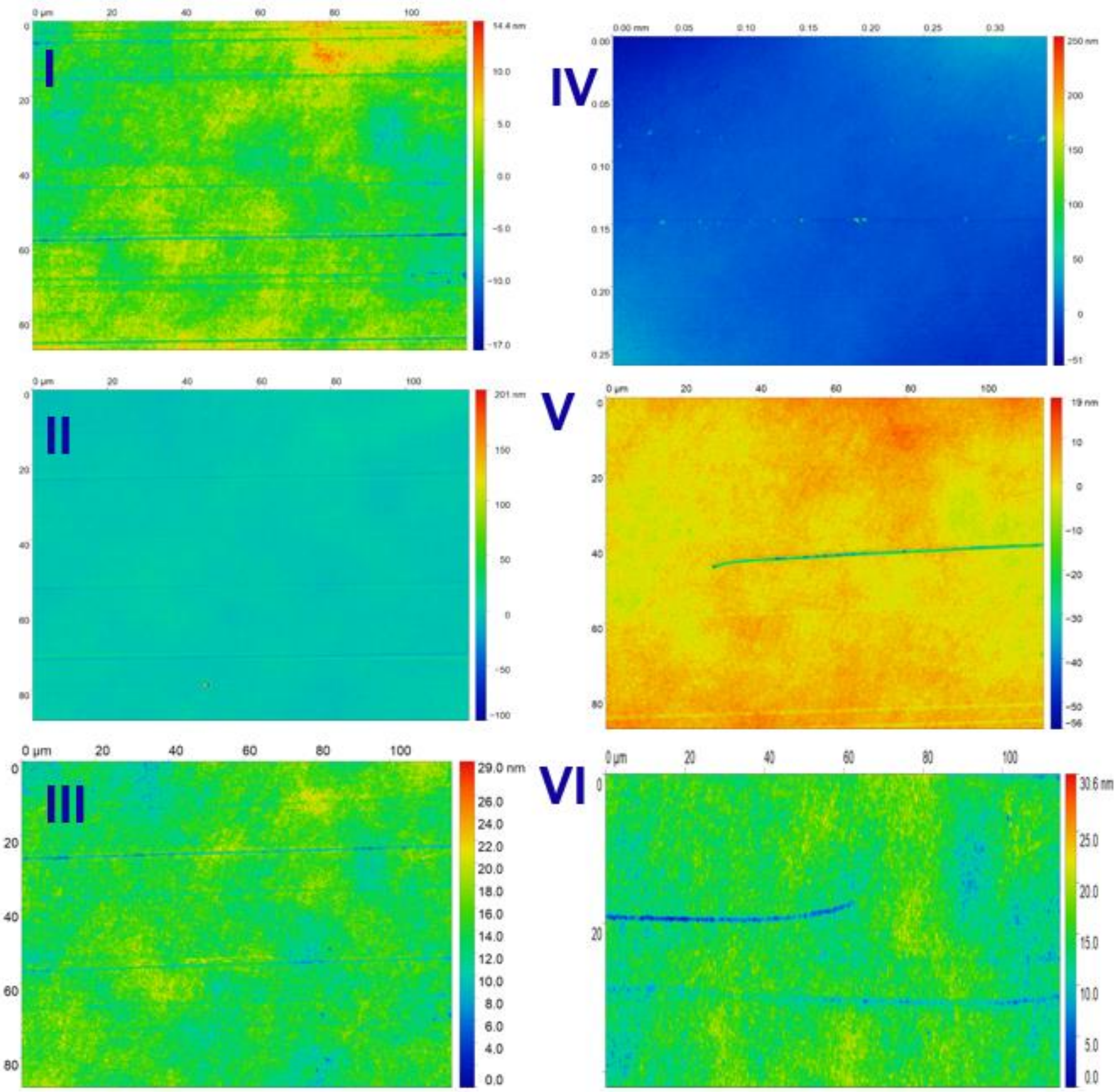

Figure A.14:I: Scratches at 9 o' clock under 150N normal load. From wafer 7. II: Scratches under 150N 2mm after start at 9 o' clock. Scratching direction is from left to right. III: Deep and shallow scratches on the DLC surface of wafer 1.VI: Two scratch (in horizontal direction) in 9 o' clock area. Bottom scratch presents wear debris inside the groove. Load used 150N. (Wafer 7). Scratching direction is from left to right. V: Deep and wide scratch under 50N, 100mm/s conditions at 7 o' clock position of wafer 1. Scratching direction is from left to right. VI: Scratches observed in wafer 2 (50N, 0.01mm/s).

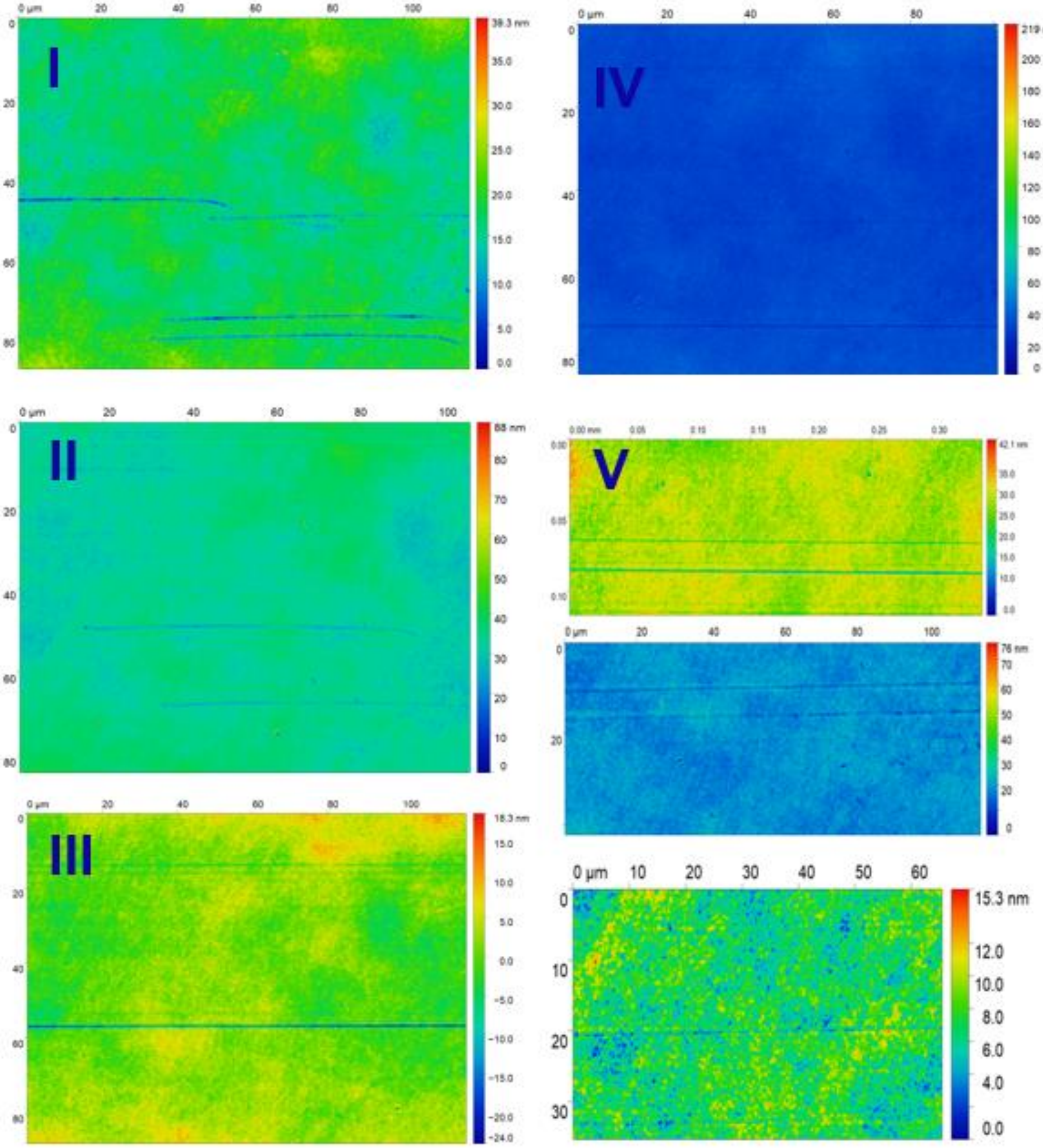

Figure A.15: I: Wafer 5 (50N, 0.01 mm/s) scratches. II: Wafer 5 (50N, 0.01mm/s) shallow scratches. III: Wafer 6 (50N, 10mm/s) shallow and deep scratches. IV: Wafer 6 shallow scratches. V: Wafer 6 scratches. No lift-up features observed.

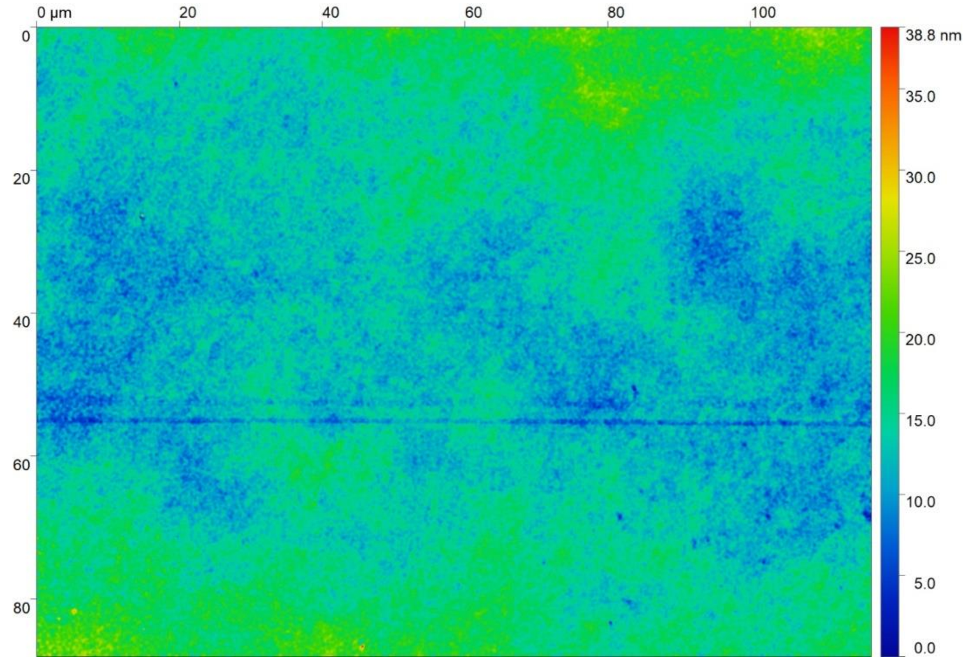

Figure A.16: Wafer 8 (50N, 10mm/s, $t_i/t_t = 1.0$) scratches.

A.2.2 Confocal micrographs from multi-asperity collision with DLC surface edge

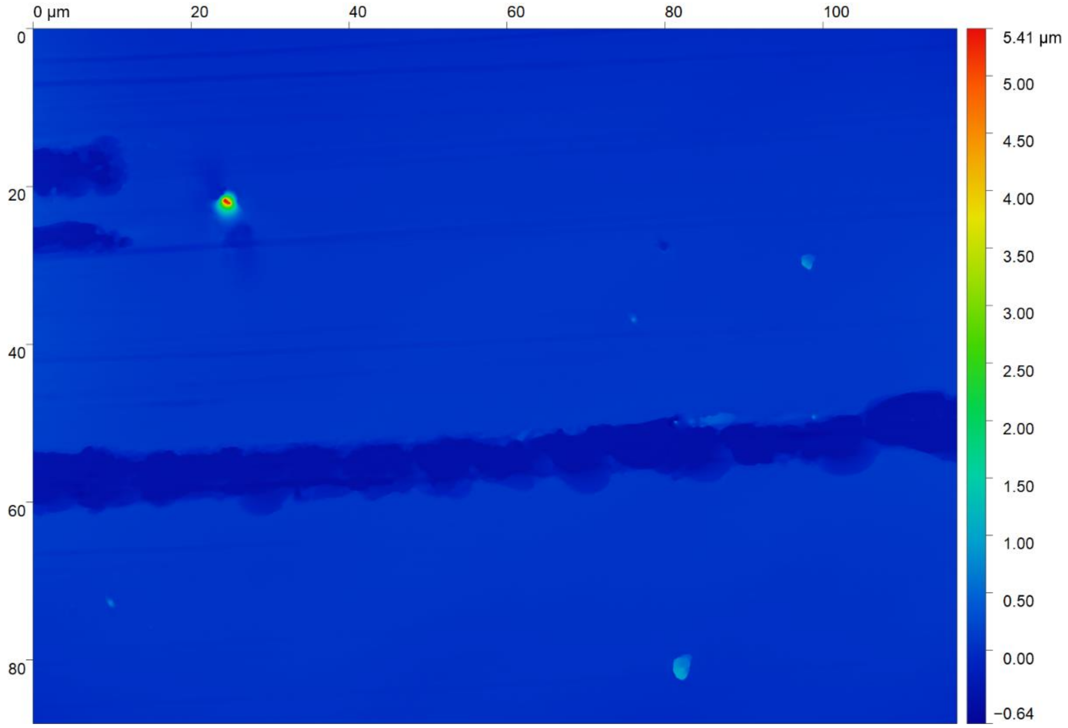

Figure A.17: Wafer 2, 50N, d/R = 0.5, F_n=50N, 9 o' clock. Edge is located in the left of the image.

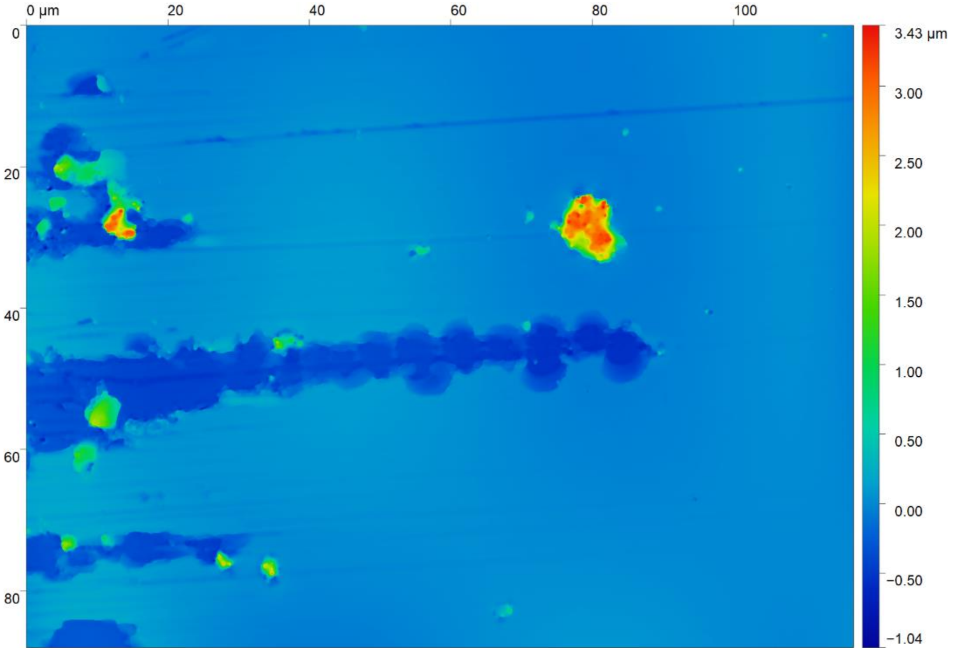

Figure A.18: Wafer 2, 50N, d/R = 0.5, F_n=50N, 9 o' clock, spallations and scratches. Wafer edge is in the left of the image.

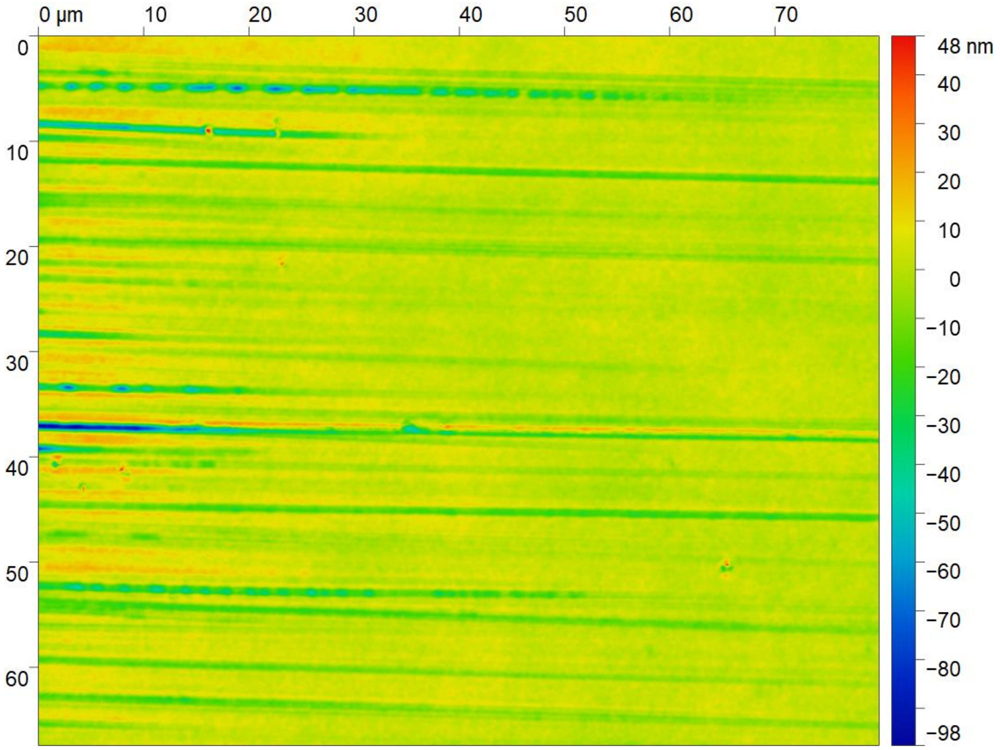

Figure A.19: Wafer 2, d/R = 0.5, F_n=50N, 9 o' clock, away from the edge. Scratching is from left to right.

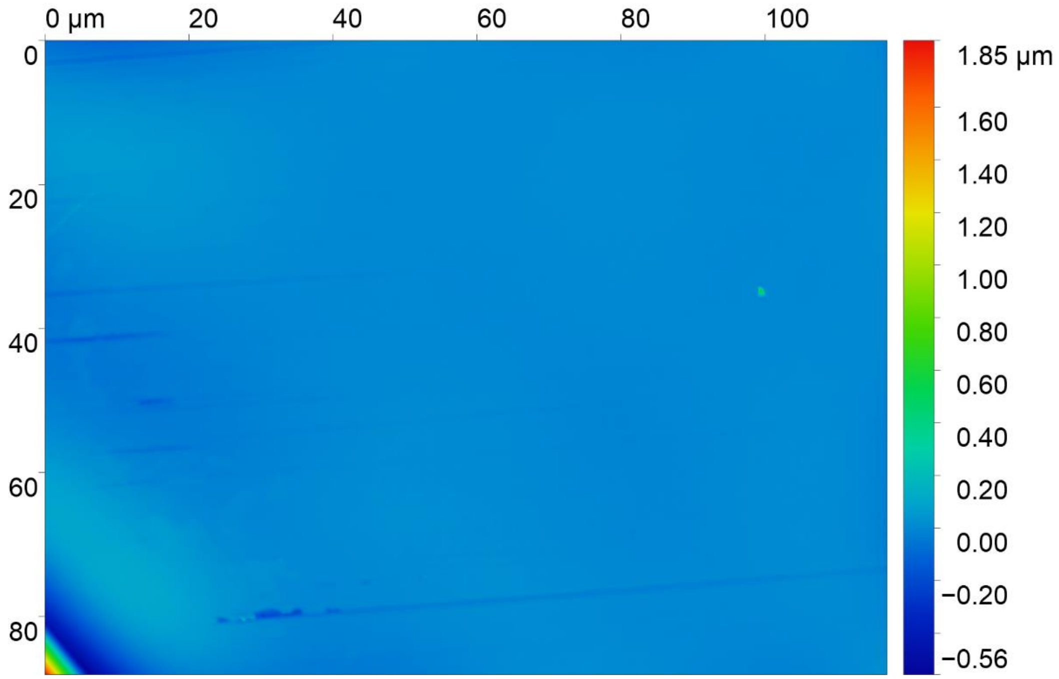

Figure A.20: Wafer 2, d/R = 0.5, F_n=150N, 9 o' clock.

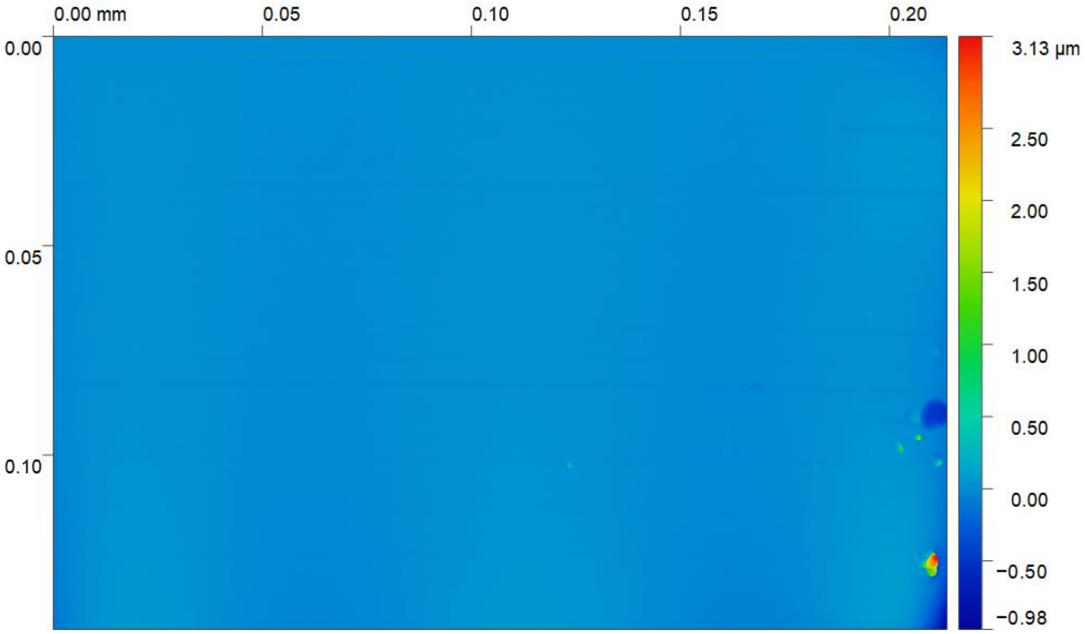

Figure A.21: Wafer 5, d/R = 0.1, F_n=150N, 9 o' clock. Scratching is from right to left. Scratches visible.

A.3 Wafer vacuum chuck

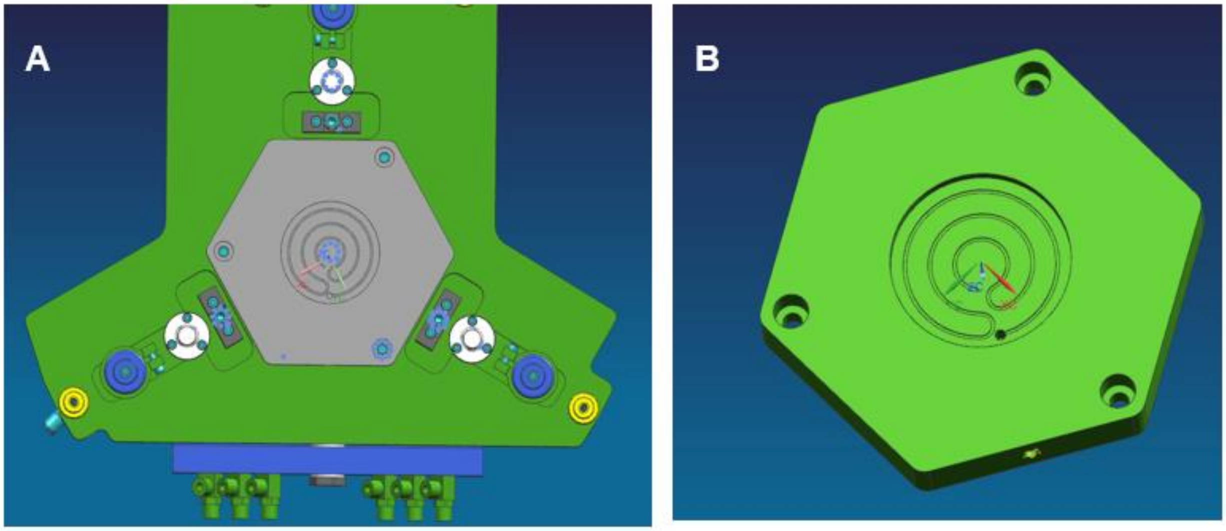

Figure A.22:A: Wafer chuck (grey) mounted on the bottom part of the Bruker UMT (green), B: Wafer vacuum chuck with a 2-inch hole where the DLC/SiC wafers were mounted.

A.4 CoF in multi-asperity scratching tests

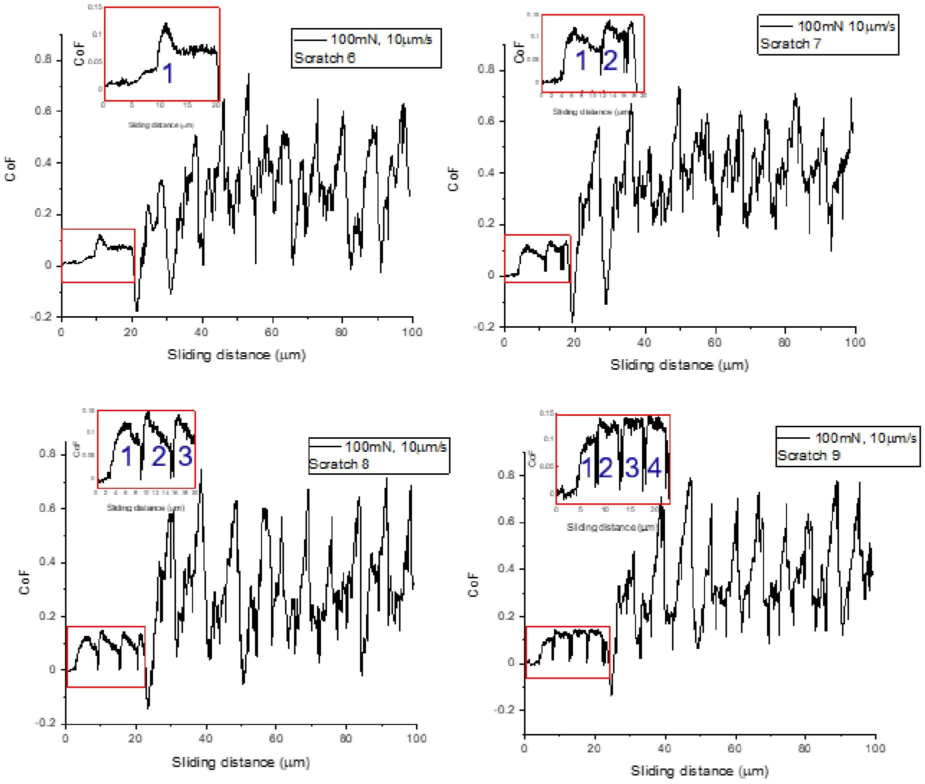

Figure A.23: CoF at the scratches where DLC spallation occurred. Before DLC spallation (roughly after 20µm of sliding) CoF

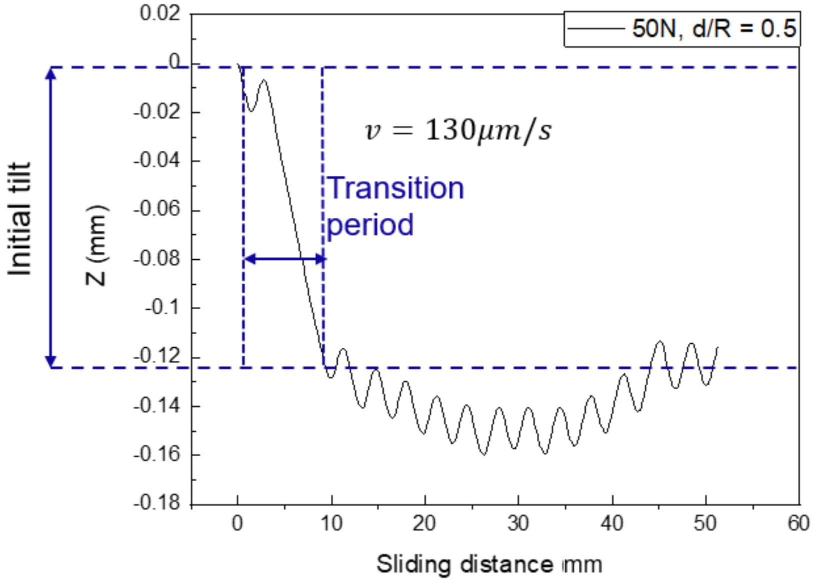

Figure A.24: z-displacement of the grit paper when it starts scratching at a distance d = R/2 from the edge of the wafer.

B Bibliography

[1] K. Holmberg and A. Erdemir, "Influence of tribology on global energy consumption, costs and emissions," *Friction,* vol. 5, no. 3, pp. 263-284, 2017.

[2] R. Singh, E. Yoon and R. Jackson, "Biomimetics: The science of imitating nature.," *Tribol. Lubr. Technol,* no. 65, p. 40, 2009.

[3] A. Singh and K. Suh, "Biomimetic patterned surfaces for controllable friction in micro-and nanoscale devices.," *Micro Nano Syst. Lett.,* vol. 1, no. 6, 2013.

[4] P. Pusplata, P. Tadge and S. Ray, "A Review On The Synthesis Strategies For The Fabrication Of Superhydrophobic Coating.," *ECS Trans.,* no. 107, p. 19835, 2022.

[5] P. Xu and e. al., "Adhesion behaviors of water droplets on bioinspired superhydrophobic surfaces," *Bioinspir. Biomim,* no. 17, p. 041003, 2022.

[6] C. Rutland, P.Cigler and V. Kubale, "Reptilian skin and its special histological structures.," in *Veterinary Anatomy and Physiology,* London, UK, IntechOpen:, 2019, pp. 1-21.

[7] E. Stratakis, "Laser engineering of biomimetic surfaces.," *Mater. Sci. Eng. R Rep.,* vol. 141, p. 100562., 2020.

[8] F. Ilie and A.-C. Cristescu, "A Study on the Tribological Behavior of Molybdenum Disulfide Particles as Additives," *Coatings* , vol. 12, no. 9, p. 1244, 2022.

[9] T. Gradt and T. Schneider, "ribological Performance of MoS2 Coatings in Various Environments," *Lubricants* , vol. 4, no. 3, p. 32, 2016.

[10] W. Liu, X. Qiao, S. Liu and P. Chen, "A Review of Nanomaterials with Different Dimensions as Lubricant Additives," *Nanomaterials,* vol. 12, no. 21, p. 3780, 2022.

[11] C. Donnet and A. E. e. al, Tribology of DLC films: Fundamentals and Applications, New York: Springer Science, 2008.

[12] N. Ohtake, M. Hiratsuka, K. Kanda, H. Akasaka, M. Tsujioka, K. Hirakuri, A. Hirata, T. Ohana, H. Inaba, M. Kano and e. al, "Properties and Classification of Diamond-Like Carbon Films," *Materials* , vol. 13, no. 315, 2021.

[13] M. Masen, ABRASIVE TOOL WEAR IN METAL FORMING PROCESSES, Enschede: PhD Thesis, 2004.

[14] K. Holmberg, H. Ronkainen and A. Matthews, "Tribology of thin coatings," *Ceramics International,* no. 26, pp. 787-795, 2000.

[15] M. VARENBERG, "Towards a unified classification of wear," *Friction,* vol. 1, no. 4, pp. 333-340, 2013.

[16] Tribology of Diamond-Like Carbon Films Fundamentals and Applications, Springer, 2008.

[17] X. Li and B. Bhushan, "Micro/nanomechanical and tribological characterization of ultrathin amorphous carbon coatings," *J. Mater. Res*, vol. 14, no. 6, 1999.

[18] Y. Zhao, D. M. Maietta and L. Chang, "An Asperity Microcontact Model Incorporating the Transition From Elastic Deformation to Fully Plastic Flow," *J. Tribol,* vol. 122, no. 86, pp. 86-93, 200.

[19] C. M. Mate and R. W. Carpick, Tribology on the Small Scale A Modern Textbook on Friction, Lubrication, and Wear, New York: Oxford University Press, 2019.

[20] J. Jamari, Running-in of Rolling Contacts, Enschede: Wöhrmann Printing Service, 2006.

[21] K. Johnson, "Normal contact of inelastic solids," in *Contact mechanics*, New York , Cambridge University Press, 1985.

[22] B. D. Beake, T. W. Liskiewicz, A. Bird and X. Shi, "Micro-scale impact testing - A new approach to studying fatigue resistance in," *Tribology International,* vol. 149, 2020.

[23] A. Perry, "The adhesion of chemically vapour-deposited hard coatings to steel—the scratch test," *Thin Solid Films,* no. 78, pp. 77-93, 1981.

[24] A. Perry, "Scratch adhesion testing of hard coatings," *Thin Solid Films,* no. 107, pp. 167-180, 1983.

[25] P. Steinmann and H. Hintermann, "Adhesion of TiC and Ti(C, N) coatings on steel," *J. Vac. Sci. Technol.* , vol. A3, pp. 2394-2400, 1985.

[26] J. Valli, "TiN coating adhesion studies using the scratch test method," *J. Vac. Sci. Technol A3,* no. 6, pp. 2411-2411, 1985.

[27] B. D. Beake, A. J. Harris and T. W. Liskiewicz, "Review of recent progress in nanoscratch testing," *Tribology - Materials, Surfaces & Interfaces,* no. 7:2, pp. 87-96, 2013.

[28] S. Bull, "Failure modes in scratch adhesion testing," *Surf. Coating Technology,* no. 50, pp. 25-32, 1991.

[29] J. v. Stebut, R. Rezakhanlou, K. Anoun, H. Michel and M. Gantois, "Major damage mechanisms during scratch and wear testing of hard.," *Thin Solid Films,* no. 181, pp. 555-564, 1989.

[30] E. Standard, "Advanced technical ceramics—methods of tests for ceramic coatings. Part 3. Determination of adhesion and other mechanical failure modes by scratch test," prEN1071-3, 42, 1999.

[31] P. Hedenquist, M. Olsson, S. Jacobson and S. Hogmark, "Failure mode analysis of TiN-coated high speed steel: in situ scratch test adhesion test in scanning electron microscope.," *Surf. Coat. Technol,* no. 41, pp. 31-49, 1990.

[32] M. Larsson, M. Olsson, P. Hedenquist and S. Hogmark, "On the mechanism of coating failure as demonstrated by scratch and indentation testing of TiN and HSS.," *Surf. Eng.,*, no. 191, 1996.

[33] Y. Wang, S. Hsu and P. Jones, "Evaluation of thermally-sprayed ceramic coatings using a novel ball-on-inclined plane scratch method.," *Wear,* no. 218, pp. 96-102, 1998.

[34] K. Holmberg, A. Laukkanen, H. Ronkainen, K. Wallin and S. Varjus, "A model for stresses, crack generation and fracture toughness calculation in scratched TiN-coated steel surfaces," *Wear,* no. 254, pp. 278-291, 2003.

[35] W. Oliver and G. Pharr, "An improved technique for determining hardness and elastic modulus using load and displacement sensing indentation experiments," *Journal od Materials Research,* vol. 6, no. 7, pp. 1564-1583, 1992.

[36] G. Pharr, W. Oliver and F. Brotzen, "On the generality of the relationship among contact stiffness, contact area, and elastic modulus during indentation," *Journal of Materials Research,* no. 7, pp. 613-617, 1992.

[37] B. S.I, "Relation between the reduced and unreduced hardness in nanomicroindentation tests," *Technical Physics,* no. 44, pp. 775-781, 1999.

[38] I. N. Sneddon, "THE RELATION BETWEEN LOAD AND PENETRATION IN THE AXISYMMETRIC BOUSSINESQ PROBLEM FOR A PUNCH OF ARBITRARY PROFILE," *Int. J. Engng Sci.,* vol. 3, pp. 47-57, 1965.

[39] A. Selvadurai, "On Boussinesq's problem," *International Journal of Engineering Science,* no. 39, pp. 317-322, 2001.

[40] G. PASCUAL, "CISION," Park Systems, 19 July 2023. [Online]. Available: https://www.prweb.com/releases/2014/11/prweb12299193.htm.

[41] "How does AFM work?," Nanosurf, [Online]. Available: https://www.nanosurf.com/en/support/afm-operating-principle.

[42] D. Fukuda, K. Niwa, K. Hattori, S. Inoue, R. Kobayashi and T.Numata, "Confocal Microscopy Imaging with an Optical Transition Edge Sensor," *Journal of Low Temperature Physics* , no. 193, pp. 1228-1235, 2018.

[43] J. Killgore and C. Higgins, "Scanning Probe Microscopy for Advanced Materials and Processes," 31 August 2020. [Online]. Available: https://www.nist.gov/programs-projects/scanning-probe-microscopy-advanced-materials-and-processes.

[44] M. Joshi, A. Bhattacharyya and W. Ali, "Characterization techniques for nanotechnology applications in textiles," *India Journal of Fibre & Textile Research* , vol. 33, pp. 304-317, 2008.

[45] J. Robertson, "Amorphous carbon," *Advances in Physics* , vol. 35, no. 4, pp. 317-374, 1986.

[46] J. Robertson, "Deposition and Characterization of Multilayer DLC/BN Films," *Materials Sciences and Applications,* vol. 37, no. 4-6, pp. 129-281, 2002.

[47] J. Robertson, "Mechanical properties and coordinations of amorphous carbons," *Phys. Rev. Lett,* vol. 68, no. 2-13, p. 220, 1992.

[48] A. C. Ferrari, J. Robertson, M. G. Beghi, C. E. Bottani, R. Ferulano and R. Pastorelli, "Elastic constants of tetrahedral amorphous carbon films by surface Brillouin scattering," *Appl. Phys. Lett. 75,* vol. 75, p. 1893–1895, 1999.

[49] J. Robertson, "The deposition mechanism of diamond-like a-C and a-C: H," *Diamond and Related Materials,* vol. 3, no. 4-6, pp. 361-368, 1994.

[50] N. Ohtake, M. Hiratsuka, K. Kanda, H. Akasaka and M. Tsujioka, "Properties and Classification of Diamond-Like Carbon Films," *Materials,* vol. 14, no. 2, p. 315, 2014.

[51] K. KALITA, R. K. GHADAI and S. CHAKRABORTY, "Parametric optimization of CVD process for DLC Thin film coatings: a comparative analysis," *Sådhanå,* vol. 47, no. 57, pp. 47-57, 2022.

[52] H. Lan and T. Kato, "Effect of Deposition Parameters on Nano-Mechanical Properties of DLC Films by PECVD," in *International Tribology Symposium,* China, 2010.

[53] Z. Wang, X. Zhong, L. Jiang, F. Qi, X. Ouyang, J. Wang and B. Liao, "Effect of interfacial delamination on coating crack in thick diamond-like carbon coatings under indentation," *Acta Mechanica Sinica,* vol. 36, p. 524–535, 2020.

[54] X. Zeng, S. Zhang, X. Ding and D. Teer, "Comparison of three types of carbon composite coatings with exceptional load-bearing capacity and high wear resistance," *Thin Solid Films,* Vols. 420-421, pp. 366-370, 2001.

[55] J. Robertson, "Properties of diamond-like carbon," *Surface and Coatings Technology,* vol. 50, no. 3, pp. 185-203, 1990.

[56] M. A. Tamor, W. C. Vassell and K. R. Carduner, "Atomic constraint in hydrogenated ‘‘diamond-like’’ carbon," *Appl. Phys. Lett,* vol. 58, pp. 592-594, 1991.

[57] "Alemnis Scratching Testing," [Online]. Available: https://alemnis.com/.

[58] E. Kral, K. Komvopoulos and D. Bogy, "Hardness of Thin-Film Media: Scratch Experiments and Finite Element Simulations," *Journal of Tribology,* vol. 18, no. 1, 1996.

[59] T. Mishra, MODELLING PLOUGHING BY AN ELLIPTICAL ASPERITY THROUGH A ZINC COATED STEEL SHEET With application to modelling friction in deep-drawing, Enschede, 2019.

[60] A. Bird, L. Yang, G. Wu and B. Inkson, "Failure mechanisms of diamond-like carbon coatings characterised by in sit SEM scratch testing," *Wear,* pp. 530-531, 2023.

[61] J. M. and Z. J. W. R.J.H., Fracture Mechanics: 2nd Edition, Delft: Delft Academic Press, 2002.

[62] K. Johnson, "Dynamic effects and impact," in *Contact Mechanics*, New York, Cambridge University Press, 1985.

[63] V. Maier, A. Hohenwarter, R. Pippan and D. Kiener, "Thermally activated deformation processes in body-centered cubic Cr – How microstructure influences strain-rate sensitivity," *Scripta Materialia,* vol. 106, pp. 42-45, 2015.

[64] L. Bai and Y. Yu, "Fatigue behaviors of diamond-like carbon films," *Diamond & Related Materials,* vol. 124, no. 108892, 2022.

[65] M. S. Kabir, Z. Zhou, Z. Xie and P. Munroe, "Scratch adhesion evaluation of diamond like carbon coatings with alternate hard and soft multilayers," *Wear,* 518-519.

[66] J. Greenwood and J. Williamson, "Contact of Nominally Flat Surfaces," *Proceedings of the Royal Society of London. Series A, Mathematical and physical sciences,* vol. 295, no. 1442, pp. 300-319, 1966.

[67] D. Tabor, "The hardness and strength of metals," *J. Inst. Metals,* vol. 79, pp. 1-18, 1951.

[68] V. Boucly, Semi-Analytical Modeling of the Transient Thermal-Elastic-Plastic Contact and its Application to Asperity Collision, Wear and Running-in of Surfaces, Lyon, 2008.

[69] J. Horng, "An Elliptic Elastic-Plastic Asperity Microcontact Model for Rough Surfaces," *Journal of Tribology,* vol. 120, no. 1, pp. 82-88, 1998.

[70] D. Cerlinca and S. Spinu, "A NUMERICAL APPROACH TO THE CONTACT OF NOMINALLY FLAT SURFACES," *International Journal of Modern Manufacturing Technologies,* vol. XIII, no. 3, pp. 2067-3604, 2021.

[71] C. Lung and D. Wang, "Microstructure and adhesion characteristics of diamond-like carbon films deposited on steel substrates," *Diamond and Related Materials,* vol. 10, pp. 1528-1534, 2001.

[72] A. Tyagi, R. Walia, Q. Murtaza, S. M. Pandey, P. K. Tyagi and B. Bajaj, "A critical review of diamond like carbon coating for wear resistance applications," *International Journal of Refractory Metals & Hard Materials,* vol. 78, pp. 107-122, 2019.

[73] N. Tayebi, T. F. Conrya and A. A. Polycarpou, "Determination of hardness from nanoscratch experiments: Corrections for interfacial shear stress and elastic recovery," *J. Mater. Res.,* vol. 18, no. 9, pp. 2150-2162, 2003.